PROCESS CONTROL OF ELECTRON BEAM SYSTEMS FOR THIN FILM COATING

By

NAMITA MAITI

(**ENGG01200704027**)

Bhabha Atomic Research Centre, Mumbai – 400 085, INDIA

A thesis submitted to the

Board of Studies in Engineering Sciences

In partial fulfillment of requirements

For the Degree of

DOCTOR OF PHILOSOPHY

of

HOMI BHABHA NATIONAL INSTITUTE, MUMBAI

July, 2013

Homi Bhabha National Institute

Recommendations of the Viva Voce Board

As members of the Viva Voce Board, we recommend that the dissertation prepared by **Namita Maiti** entitled "**Process Control of Electron Beam Systems for Thin Film Coating**" may be accepted as fulfilling the dissertation requirement for the Degree of Doctor of Philosophy.

____Date:
Chairman: Prof. A. P. Tiwari

____Date:
Guide / Convenor: Prof. M. S. Bhatia

____Date:
Member 1: Prof. S. V. G. Ravindranath

____Date:
Member 2: Prof. A. Bhattacharjee

____Date:
External Examiner: Prof. D. K. Pandya, IIT-Delhi

____Date:
Internal Examiner: Prof. (Smt.) A. Sharma

Final approval and acceptance of this dissertation is contingent upon the candidate's submission of the final copies of the dissertation to HBNI.

I hereby certify that I have read this dissertation prepared under my direction and recommend that it may be accepted as fulfilling the dissertation requirement.

Date:

Place: Mumbai **Guide: Prof. M. S. Bhatia**

STATEMENT BY AUTHOR

This dissertation has been submitted in partial fulfillment of requirements for an advanced degree at Homi Bhabha National Institute (HBNI) and is deposited in the Library to be made available to borrowers under rules of the HBNI.

Brief quotations from this dissertation are allowable without special permission, provided that accurate acknowledgement of source is made. Requests for permission for extended quotation from or reproduction of this manuscript in whole or in part may be granted by the Competent Authority of HBNI when in his or her judgment the proposed use of the material is in the interests of scholarship. In all other instances, however, permission must be obtained from the author.

Namita Maiti

DECLARATION

I hereby declare that the investigation presented in the thesis has been carried out by me. The work is original and has not been submitted earlier as a whole or in part for a degree/diploma at this or any other Institution / University.

Namita Maiti

DEDICATIONS

I dedicate this thesis to my Parents

Smt. Charushila Maiti

and

Shri Jamini Kanta Maiti

ACKNOWLEDGEMENTS

I would like to express my deep sense of gratitude towards my guide Dr M S Bhatia for his valuable guidance, keen interest and encouragement during the course of this work. I am extremely grateful to Dr. B. K. Dutta, Dr A P Tiwari, Dr S V G Ravindranath and Dr K V Nagesh, Dr. A. Bhattacharjee and Dr. (Smt) A. Sharma for their constant encouragement and fruitful discussions during this work. I am indebted to Dr. K. B. Thakur, Dr A K Das and Dr L M Gantayet for their support.

My sincere thanks to my colleagues Mr U. D. Barve, Mr. S. Mukherjee, Dr. B. Dixit, and Dr. D. Bhattacharyya for their valuable suggestions and cooperation during the experiments and subsequent analysis.

I am grateful to my father Shri Jamini Kanta Maiti, mother Smt. Charushila Maiti, brothers (Shri Santosh Kumar Maiti and Shri Sourindra Kumar Maiti), sisters (Ms. Usha Maiti, Smt. Gita Maiti and Smt. Kabita Giri), father-in-law and mother-in-law for their moral support and numerous blessings.

I thank my husband, Dr. Sunil Kumar Kopparapu for many technical suggestions, helping in manuscript preparations, proof reading of the manuscripts and supporting me all throughout. Finally it is my loving son, Mast. Sumit wanted me to complete my PhD study at the earliest – I am indeed thankful to him.

Namita Maiti

List of Abbreviations

AFM Atomic Force Microscopy

ALD Atomic Layer Deposition

CFD Computational Fluid Dynamics

EBPVD Electron Beam Physical Vapor Deposition

EHT Extra High Tension

EMA Effective Medium Approximation

ESCA Electron Spectroscopy for Chemical Analysis

FCVA Filtered Cathodic Vacuum Arc

FFT Fast Fourier Transform

GIXR Grazing Incidence X-ray Reflectivity

PLD Pulsed Laser Deposition

RCRHF Rectangular Cathode with Rectangular Holdings with Fins

RCRHWF Rectangular Cathode with Rectangular Holdings without Fins

SE Spectroscopic Ellipsometry

TCRHF Trapezoidal Cathode with Rectangular Holdings with Fins

TCTHF Trapezoidal Cathode with Trapezoidal Holdings with Fins

TCTHWF Trapezoidal Cathode with Trapezoidal Holdings without Fins

XPS X-ray Photoelectron Spectroscopy

Contents

List of Figures

List of Tables

List of Publications

INTERNATIONAL JOURNALS

1. Namita Maiti, S. Mukherjee, Bhunesh Kumar, U. D. Barve, V. B. Suryawanshi, and A. K. Das, “Design and development of indirectly heated solid cathode for strip type electron gun”, Review of Scientific Instruments , vol.81, no.1, pp.013302-013302-10, Jan 2010 doi: 10.1063/1.3271539
2. Namita Maiti, A. Biswas, R. B. Tokas, D. Bhattacharyya, S. N. Jha, U. P. Deshpande, U. D. Barve, M. S. Bhatia and A. K. Das , “Effects of Oxygen flow rate on microstructure and optical properties of Aluminum oxide films deposited by electron beam evaporation technique”, Vacuum, Volume 85, Issue 2, 20 August 2010, Pages 214-220, ISSN 0042-207X, 10.1016/j.vacuum.2010.05.017.
3. Santalal Mukherjee, Namita Maiti, U. D. Barve, A. K. Das, “An indirectly heated solid cathode for linear electron beam emitter assembly”, Vacuum, Volume 84, Issue 7, 4 March 2010, Pages 920-923, ISSN 0042-207X, 10.1016/j.vacuum.2010.01.002.
4. Namita Maiti, U. D. Barve, M. S. Bhatia, and A. K. Das, “Design of transverse electron gun for electron beam based reactive evaporation system”, Review of Scientific Instruments, Review of Scientific Instruments, vol.82, no.5, pp.056106-056106-3, May (2011) doi: 10.1063/1.3597576
5. Namita Maiti, U. D. Barve, Shakti Kumar Mishra, M. S. Bhatia, and A. K. Das “Attenuation of electron gun generated surges in an electron beam evaporation system using ferrite beads”, Vacuum, 86 (2012), pp 1810 - 1814 , Available online 27 April 2012, ISSN 0042-207X, 10.1016/j.vacuum.2012.04.028.

SYMPOSIUM

1. Namita Maiti, Atul Tak, Yashodhan Khabade, V. B. Suryawanshi and A. K. Das, “Modeling of vapor transport of electron beam evaporation based coating system”, AIP Conf. Proc. 1451, (2012) pp 304-306.
2. Namita Maiti, P. Karmakar, U. D. Barve, A V Bapat, "An Evaporation System for Film Deposition Using Electron Beam Sources", International Symposium on “Vacuum Science and Technology”, Journal of Physics: Conference Series 114 (2008) 012049.
3. Pallab Karmakar, Namita Maiti, A V Bapat, "Design and Performance of Differential Pumping System of Coating Unit", International Symposium on “Vacuum Science and Technology”, Journal of Physics: Conference Series 114 (2008) 012069.

4. Namita Maiti, P. Karmakar, U. D. Barve, A V Bapat, "An Evaporation System for Film Deposition Using Electron Beam Sources", International Symposium on “Vacuum Science and Technology”, Bulletin of Indian Vacuum Society, Vol. 12(2), 2009, pp 3-7.
5. Namita Maiti, U.D. Barve, Jagannath, S.Mukherjee, M.S. Bhatia, A.K. Das, “Deposition of boron thin film by using electron beam evaporation technique’’, presented at National Conference on Recent Advances in Surface Engineering (RASE 09), NationalAerospace Laboratories, Bangalore, 26-27 Feb’2009.

ABSTRACT

The on-going work in electron beam physical vapor deposition (EBPVD) technology has infused a lot of confidence in developing many new coatings. The unique features and flexibility of EBPVD arise due to its controllability in variation of structure and composition of processed materials, low contamination and high packing density in deposits. EBPVD technique offers freedom from impurity, many unique features, like independence in control of microstructure and composition of the coating via manipulation of controlling process parameters such as pressure level, substrate temperature, gas content (in case of reactive evaporation), power (voltage, current) and evaporant composition.

To achieve desired coating, process control plays an important part. Also the required stoichiometry of the coating can be obtained only when all the process parameters are suitably controlled. The electron gun, which is the heart of the evaporation system, is energized through a high voltage power source and auxiliary power supplies, needs to operate without interruption. However, the gun suffers from breakdown problem. So the gun and power sources have to be designed to mitigate breakdown effects. The focus of the research reported in this thesis revolves around 1) emphasis on the design of electron beam gun and its optics through simulation and experimental validation, 2) damage control of electron gun generated surges by using ferrite beads thereby reducing process interruptions and 3) finding suitable range of process parameters to enable the desired coating of alumina (representative coating) via experimentation and characterization of coatings.

An electron gun has three electrodes, namely, cathode, anode and focusing electrode. Various authors have reported the work on gun design and they are mostly limited to directly heated cathode based gun design whether it is high beam power or low beam power gun. High power evaporation gun for strip coaters is generally strip type. Due to thermal expansion, directly heated filament has the inherent disadvantage of filament distortion,

change of shape and movement with respect to the focusing electrode. Moreover, directly heated filament generates strong self-induced magnetic field due to the filament heating current. The effects of cathode distortion and self-induced magnetic fields result in non-uniform distribution of heat flux on the work surface. On the other hand, indirectly heated type solid cathode guns are not besieged with these issues. The investigations presented in this thesis pertain to indirectly heated cathode based gun with major emphasis on strip type beam for high power gun. In particular, the design analysis of a high power indirectly heated solid cathode (for a 200 kW, 45 kV, and 270^{o} bent strip type electron gun) has been presented. The design approach consists of simulation followed by extensive experimentation with different cathode configurations. The designed cathode is of trapezoidal section (8 mm x 4 mm x 2 mm) with an emitting area of 110 mm x 4 mm made up of tantalum operating at about 2500 K. The solid cathode at an operating temperature of 2500 K generated a well defined electron beam. Electromagnetic and thermo-mechanical simulation is used to optimize the shape of the beam. Thermal modeling has also been used to analyze the temperature and stress distribution on the electrodes. The simulation results are validated by experimental measurement.

Directly heated type gun design for low power beam has been carried out with special emphasis on reactive evaporation, which is carried out generally in higher pressure environment. A bend of 270^{o} decouples the e-beam generation zone from generated vapor. For a metallic coating the high vacuum in the order of $5x\ 10^{-3}$ Pa is needed, so the vapor generation zone and the beam generation zone can be mounted on one chamber. For reactive coating, pressure in the range of 10^{-1} Pa to 10^{-2} Pa is needed but e-guns do not operate reliably in this pressure range due to frequent voltage flashover. In order to overcome this problem, substrate chamber is isolated from gun chamber using a bifurcation plate. On this bifurcation plate, an aperture is provided for e-beam to emerge from the gun chamber to the substrate chamber. Using the differential pumping arrangement the gun chamber pressure is maintained at better than $5x10^{-3}$ Pa, whereas substrate chamber pressure can be between 10^{-1} Pa and 10^{-2} Pa. The dimensions of this aperture are critical to maintain this pressure difference. Design of a 10 kV, 10 kW transverse electron gun, suitable for reactive evaporation is also presented in this work by simulation and modeling. Simulation of the electron beam trajectory helps in locating the emergence aperture after 90^o bend and in designing the crucible on which the beam is finally incident after 270^o bend. Experimental validation has been done for beam trajectory by piercing a stainless steel plate at 90^o position which is kept above the crucible.

Vapor transport studies of titanium and yttria have been carried out with the help of CFD modeling. The modeling provides the detailed insight of the coating process when the coating operation is carried out. CFD modeling has been used in this thesis for non-uniform temperature distribution on the evaporant surface. Also the reactive evaporation of yttria has been modeled using CFD. The coating thickness has been validated with experimental results.

Vacuum breakdown is a very common problem during the operation of any electron gun. This not only spoils the coating, it also causes lot of damage to the electronic components of the system. The approach adopted in this work is to attenuate the breakdown current near the gun so that it does not propagate to the power source to cause any detrimental effect. An investigation has been carried out to reduce the amplitude and the high frequency content of the signal. Ferrite beads have been used to suppress the high frequency content of the breakdown signal and also the amplitude of the breakdown signal reduces. High frequency content of the signal in the MHz range could be attenuated to lower range of KHz by use of ferrite beads.

Reactive evaporation technique has been used to deposit thin films of alumina (Al_2O_3) on crystalline Si substrates at ambient temperatures in an electron beam (e-beam) evaporation system using alumina granules as evaporant material. The loss of oxygen due to dissociation of alumina has been compensated by bleeding high purity oxygen gas into the system during evaporation. The density and optical properties of the films showed interesting variation with oxygen flow rates.

CHAPTER 1

Introduction

Over the past few years thin film coating has developed continuously. Thin film studies have provided impetus to many new areas of research in solid state physics, chemistry and surface physics, which are based on phenomena uniquely characteristic of the geometry, thickness and structure of thin films. PVD (Physical Vapor Deposition) has been used for production of semiconductor devices, optical components, wear resistant hard coated cutting tools, thermal and chemical barrier coatings. PVD can be resistive, electron beam based EBPVD (Electron Beam Physical Vapor Deposition) or plasma sputter deposition. Better controllability of evaporation rate and high purity of coating due to vacuum environment has made the evaporation by electron beam more attractive compared to other means of coating. Also vaporization of reactive and refractory materials using water-cooled crucible have been possible. As the evaporant material is placed in a water-cooled crucible and molten evaporating zone is contained within its own cooler skull, the chemical reactivity problem between evaporant material and the crucible is avoided.

The EBPVD system comprises of a chamber where the electron gun and the crucible are housed, the vacuum system for this chamber, high voltage power source to energize the electron gun, crucible manipulator, substrate holding system where the substrate to be coated is mounted and the work pressure control system. All these components are highly integrated, and therefore the performance of the coating system depends on the performance of each component. An electron beam generated by electron gun is directed to heat the evaporant material kept in the crucible and the evaporated vapor gets deposited on the substrate to give rise to the desired coating.

Electrons are emitted thermionically from heated tungsten/tantalum cathode obeying Richardson Equation:

$$J = AT^2 \exp\left(-\frac{e\phi}{kT}\right)$$

where, J = current density, A = Richardson constant, T = temperature in K, e = electron charge, ϕ = work function, k = Boltzman constant

As the current increases, field generated by the cathode anode spacing and the voltage applied, controls how much current can be obtained obeying the Child-Langmuir Equation:

$$J = 2.335 \times 10^{-6} \frac{V^{\frac{3}{2}}}{d^2}$$

where, V = voltage, d = cathode anode distance

Only if the voltage is increased, the current increases in the space charge limited region. For a Pierce [1] type gun operating in the space charge limited mode, power is increased by increasing the voltage. An electron in motion in a magnetic field experiences a force perpendicular to its direction and to the magnetic field. This effect causes electron beam to deflect in transverse and axial beam gun. Permanent magnet is used to provide the main deflection field for transverse beam gun of low power, but an electromagnet is used for high power gun. Transverse beam gun requires a fixed and stable voltage to maintain non - variable beam radius, so it operates in emission limited mode and the power is increased by increasing the cathode temperature. Fig. 1.1 shows the schematic of the axial and 180^{o} bent beam electron gun. However 270^{o} bent beam gun decouples the vapor generation region from the electron gun region resulting in improved performance. The 270^{o} bent beam gun has been the focus of this research work.

.

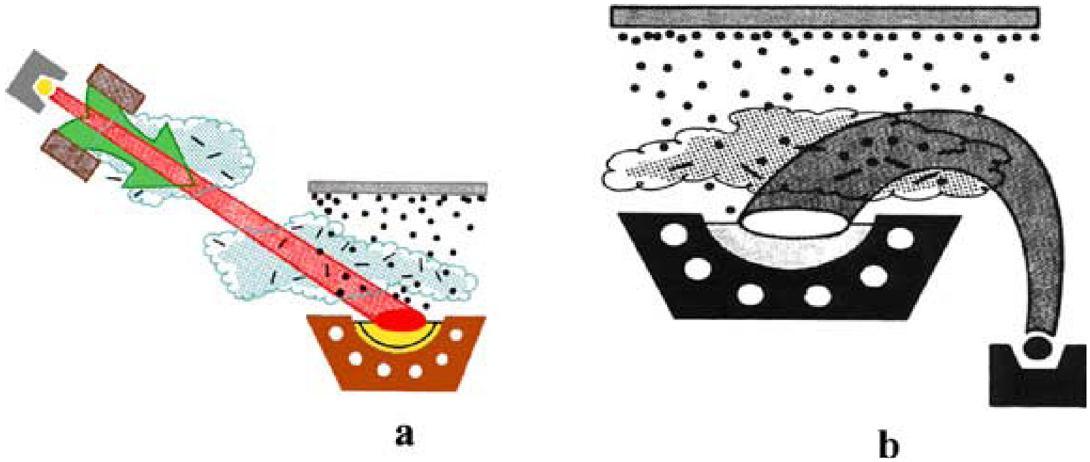

Fig 1.1 Schematic diagram showing: (a) axial and (b) bent beam electron gun [1].

The electron beam generated by thermionic emission is accelerated and bent by 270^o in an E x B field, which subsequently hits the evaporant material placed on a crucible. The beam power is translated into heat energy on the evaporant material thereby generating stream of vapor. The substrate to be coated is placed above the vapor stream to obtain desired coating with the help of suitable control on evaporation rate and surrounding medium depending on the type of coating. In order to achieve the desired coating, the process control plays an important part. The required stoichiometry of the coating can be obtained only when all the process parameters are suitably controlled. The low power electron gun is shown in the Fig. 1.2 and the gun-crucible assembly is shown in the Fig 1.3. The electron gun is energized through a high voltage power source and auxiliary power supplies. The electron gun has its breakdown problem, so the gun has to be designed to tackle the breakdown related issues. After these issues are resolved, each power supply is regulated through proportional-integral controller. Therefore, the focus of this research is mainly on the design of electron gun and interruption free process.

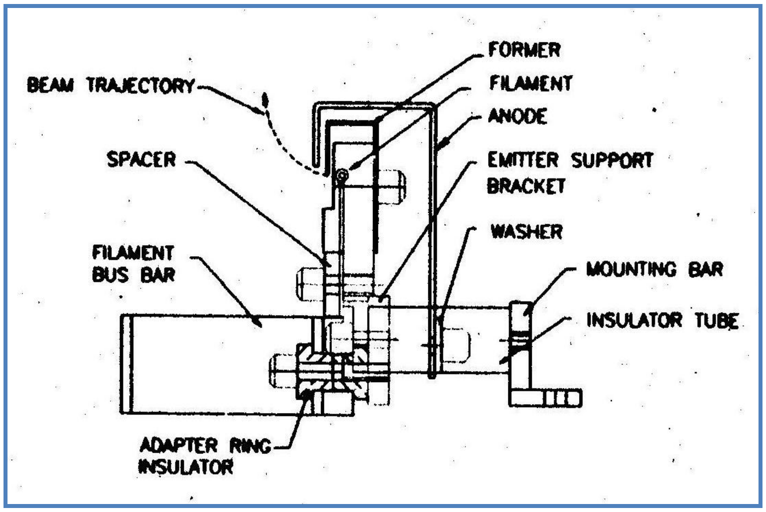

Fig 1.2. Electron gun

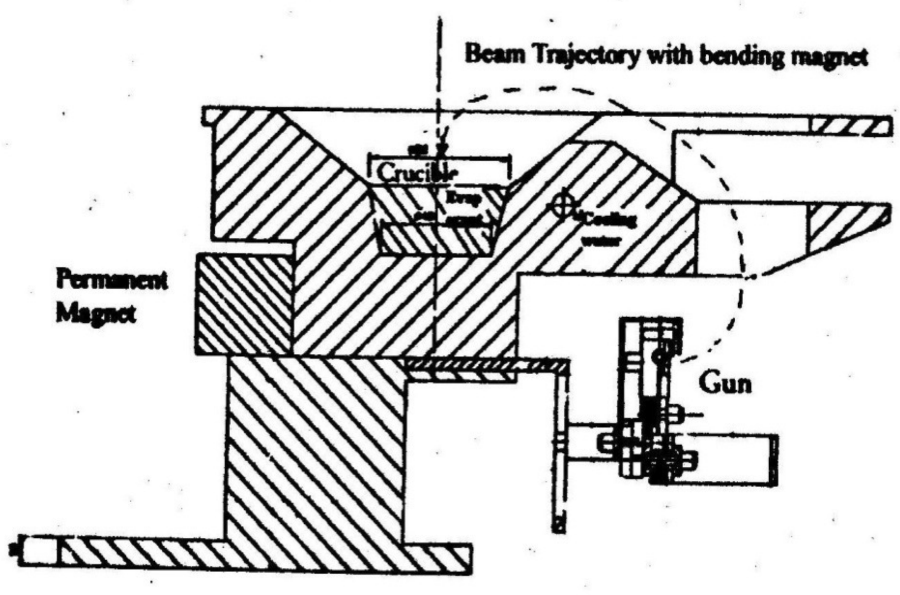

Fig 1.3. Electron gun and crucible assembly

CHAPTER 2

Literature survey

2.1 Literature update and directions of research

One of the central issues in development of electron beam evaporation based system is in the design of the electron gun and the ambient in which it is to operate. Needless to say, the design of electron gun is dependent on the applications, namely, evaporation, melting and welding. So the gun can be a bent beam (transverse) type or an axial type. It can be a high power gun or low power gun. In evaporation system bent beam type of electron gun is used in order to achieve vapor decoupling.

The methods of shape optimization to design the cathode of an electron gun has been discussed in [2] on axial gun. The dynamical equations modeling the electron particle path as well as the generalized shape optimization problem has been reported in this paper.

Computer optimization techniques has also been used in [3] with several different design parameters while considering multiple design criteria, including beam and gun properties on axial gun. In the high power regime of evaporation gun, design and performance of an 80 kW strip electron gun [4] with a focal strip of 80 x 5 mm^2 using directly heated cathode is reported. This is a transverse gun. Electrons from an electrically heated, multi-segmented tantalum filament are electrostatically focused to provide a sheet of electrons in the post-anode region, that when bent through 270° along a circle of radius 120 mm by a uniform magnetic field, focuses on the target. Magnetically focused line source electron gun on a strip of 80 x 2 mm^2, which could be scanned over a range of 100 mm in a direction perpendicular to the long dimension of the strip has been reported in [5].

A tungsten wire of length 140 mm with diameter 0.9 mm was used as a directly heated thermionic electron beam source in [6]. An emission current of 5000 mA was achieved at an input heating power of 600 W. Cathode to anode distance of 6 mm with acceleration voltage of 10 kV was used. A uniform external magnetic field of 50 G was employed to obtain a well-focused electron beam at a deflection of 180°, with cathode to work site distance of 130 mm. Dimensions of the beam is 1.25 x 120 mm^2 recorded at the work site.

Due to thermal expansion, directly heated filament has the inherent disadvantage of distortion (filament shape) and movement with respect to the focusing electrode. A spring assembly has been proposed in [7] to prevent sagging and distortion of the filament due to thermal expansion.

In order to maximize the practical working temperature of a large-surface cathode, electron bombardment from a secondary filament has been reported in [8]. This method has three important advantages. In order to overcome the problems of directly heated cathode, the concept of indirectly heated cathode has been proposed in [9] for cathode length less than 50 mm. Though the concept of indirectly heated cathode has been proposed, there has been no detailed report on design issues of high power cathode reported in literature, especially for cathode length greater than 50 mm.

The development of directly and indirectly heated cathode have been reviewed in [10]. We investigate (as shown in [11]) indirectly heated cathode based gun with major emphasis on strip type beam for high power gun. In particular, an indepth analysis and design of a high power (200 kW, 45 kV) indirectly heated solid cathode (110 mm length) has been carried out. The design of high power gun is based on simulation and analysis by extensive experimentation with several cathode configurations. An indirectly heated cathode model [12] has been utilized for this analysis. The tantalum filament gains power by resistance heating from a DC source. It emits electrons on reaching the emission temperature. The emitted electrons are attracted towards the solid cathode due to relative positive potential of solid cathode with respect to the filament. Solid cathode gains power by electron bombardment and to some extent by radiation heat from the filament. For beam trajectories in the filament - solid cathode space, simulation has been carried out using an electron optics software EGUN© by SLAC [13].

In the regime of low power evaporation, the gun is generally a directly heated type and a few designs of bent beam (180°) electron gun using non-uniform magnetic field has been reported [14]. Bending the beam by 270°, the evaporant vapors can be further prevented to enter the electron gun region thereby decoupling the vapor generation zone from beam generation zone. Commercial coaters that use this feature are available. For a metallic coating, the coating takes place in the high vacuum medium in the order of 5×10^{-3} Pa, so the vapor generation setup and the beam generation setup can be mounted on one chamber. However, for non-metallic coating the reactive coating is necessary. Hence the desirable properties can be achieved in the pressure range of 10^{-1} Pa to 10^{-2} Pa. At this high pressure the electron gun does not operate reliably due to high voltage flashover. In order to overcome this problem, in this thesis, an electron gun has been designed for a differentially pumped reactive evaporation system. The substrate chamber is isolated from gun chamber using a bifurcation plate. On this bifurcation plate, aperture is provided for beam emergence from the gun chamber to the substrate chamber. Using the differential pumping arrangement [15] the gun chamber pressure is maintained at better than 5×10^{-3} Pa, whereas substrate chamber pressure can be between 10^{-1} Pa and 10^{-2} Pa. The design of 270° bent beam electron gun of non- axi-symmetric configuration using non-uniform magnetic field to operate in an ambient of 10^{-1} Pa to 10^{-2} Pa has been presented in this research work [16].

Understanding the coating process is facilitated when it is modeled suitably for evaporation and deposition process. The theory of evaporation was established by Hertz, then

Langmuir and followed by Knudsen. The cosine model and its variants have been used in several evaporation applications for simple emitting shapes (eg. Circle, line etc.). Monte Carlo method is used to compute the vapor flux distribution in [17] and it provides the stochastic nature of evaporation process. However, Monte Carlo models are not available in closed form, so it is difficult to use them for system level analysis. Finite element models [18-19] are used to describe atom/molecules dynamics during EB–PVD process. Using finite element method, the computational model of EB-PVD has been extended [20] by the substrate manipulation model, which mathematically formulates substrate manipulation using coordinate transformation technique.

In [21-22], CFD (computational fluid dynamics) modeling is used to simulate the deposition process using the inlet boundary conditions with constant temperature, pressure and mass fractions of titanium vapors. Using non-uniform temperature distribution on the evaporant surface, the CFD modeling has been extended to the present study of work in this thesis. Following the vapor pressure contours as reported in [23], the Knudsen number is found to be less than 0.1 in the computational domain. Therefore, CFD modeling could be applied to obtain vapor flux distribution.

For metallic coating the vapor transport mechanism is not influenced by any external inlet. Whereas, for any reactive coating, the vapor transport is influenced by external inlet. As a representative case we have considered the coating of yttrium oxide.

Yttrium-oxide (Y_2O_3) is a compound of yttrium and oxygen, so at a high temperature chemical reactions take place. As Y_2O_3 is heated above 2680 K, it transforms in vapor phase. The products will be YO, O and yttrium. Yttrium metal in gas form reacts readily to form Y_2O_3 in the presence of oxygen. Therefore external oxygen is bled into the system. The possible reactions as reported in [24] have been considered for the analysis and subsequent experimentation.

One of the central issues in development of an electron beam evaporation based system is the interruption free process. The interruption arises due to breakdown in the gun. Besides process degradation, this phenomena poses threat to the feeding power source and associated control electronics. More specifically, as the material in the crucible evaporates, positive metal vapor ions may be generated, which may go back to the emitter along the same path taken by the electron beam causing erosion in the emitter [25]. All these factors sometimes make it difficult to ascertain the reliable high voltage performance of the electron gun. To overcome the breakdown problem, one tries to maintain the electric field as uniform as possible. Safe limit is followed while choosing the inter-electrode gap and also the creepage path of the insulator. Electrode profiles are modified to maintain the electric field at acceptable level. After following all the necessary high voltage related guidelines, the breakdown reduces considerably. Work along these lines have been reported from time to time. The investigation reported in [26] prevents arcing in the gun by providing an improved electrostatic field, an improved magnetic field and an improved insulation on high voltage leads. In an axial gun, reported in [27], the gun is shielded from the magnetic field with the help of a magnetic flange. These approaches are possible in an axial e-gun. For a transverse e-gun, grounded metallic shield as reported in [28] has been used to prevent establishing a discharge by utilizing the concept of 'dark space'. A metallic shield is installed around all of the HV elements. The spacing between the shield and the HV elements is less than the dark space at a pressure .13 Pa or more. The dark space is also filled with controlled Argon gas such that the system chamber and the dark space can be effectively isolated.

While breakdown probability can be reduced drastically through optimized field configuration and gun operating condition, breakdowns cannot be eliminated completely. Hence, additional measures need to be provided to control after effects of the breakdown.

Quite frequently when this high voltage high frequency surges reach the power supply, it damages the circuit elements. Rectifiers used in the filament power supply are the most affected elements. In addition, controller ICs also fail due to the surges. In order to overcome this problem, low inductance capacitors are used across the filament supply and the high voltage supply. Capacitors absorb the energy of the surges at a low voltage level so that the reverse rating of the rectifiers are not exceeded. If the capacitor response frequency is lower than the frequency of HV surges, this protection is ineffective. A solution that is often used for protection against this breakdown problem is to detect the rapid increase in current [29] and switching off the power supply. High speed detection system consisting of tetrode electronic tube in series with the electron gun limits the flashover within 20 μs. The use of rapid switching off power supplies is acceptable when evaporation is performed in high vacuum better than 1x 10^{-2} Pa. For reactive evaporation, the electron beam source operates at high pressure due to external bleeding of gas to maintain stoichiometry. At such high pressure, the rapid occurrence of arc cannot be controlled by the rapid switching off power supplies. As an alternative to a power supply with a tetrode tube, high frequency or switch mode systems are used to decrease arcing energy and hence the extent of damage. The high frequency power source with transient signal controller which controls feedback signals at arcing is reported in [30]. When the power supply is switched off after detecting the initiation of arc, the power supply energy is dumped in the electron gun causing damage to the gun as well as the job being carried out. In [31], Features of current protection of power sources has been reported. Finally, a qualitative scheme for protection against surge voltages by providing a pair of electrical conductors being passed through high permeability toroid is reported in [32].

The present approach is to attenuate the breakdown current near the gun so that it does not propagate to the power source to cause any detrimental effect. Ferrite beads have been used to suppress the high frequency content of the breakdown signal and also the amplitude of the breakdown signal reduces. The breakdown signal is monitored using an induction sensor [33]. The bandwidth of the sensor is designed through calculation of the inductance [34] and capacitance [35] of the sensor coil. The selection of a suitable ferrite bead to reduce the high voltage breakdown related problem has been based on [36-37].

As an application to the electron beam based coating system, the reactive coating of alumina has been taken up. Thin film of Al_2O_3 (Aluminum oxide or alumina) finds various technologically important applications because of its several important properties. Its high dielectric constant is exploited in its use as passivation layers in MOS devices [38] and as protective optical coatings [39], while its high wear resistance property and inertness are used in applications as wear and corrosion resistance coatings [40, 41]. Various techniques have been used to deposit aluminum oxide thin films such as magnetron sputtering [42-49], filtered cathodic vacuum arc (FCVA) [50-51], atomic layer deposition (ALD) [52-53], pulsed laser deposition (PLD) [54], plasma enhanced chemical vapor deposition [55], spray pyrolysis [56-57] and electron beam evaporation [57-58].

In [45] alumina films were prepared by r.f. magnetron sputtering from an Al_2O_3 ceramic target (Al_2O_3 99.99% pure) in argon or in argon and oxygen mixtures. The O/Al ratios for these films, as determined by Rutherford backscattering spectrometry and X-ray fluorescence, were higher than or equal to the ratio expected from stoichiometric alumina. Sputtering, although controlled and scalable process, but fails to give films with high refractive index [45]. High refractive index films have been obtained by cathodic vacuum arc technique where specific precautions have to be taken to prevent deposition of macroparticles on the substrate [50, 51]. ALD is a process in which precursors are supplied into a reaction chamber in a multitude of alternating absorption and reaction steps. Thus, the material is deposited in a self-limited layer-by-layer growth mode. To analyze the crystallization behavior of thin Al_2O_3 films, the material was deposited on p-type silicon wafers by atomic layer deposition (ALD) [53]. Though relatively low cost and easily scalable process like spray pyrolysis yields films with good electrical properties, refractive index of the films are low [57]. On the other hand, electron beam evaporation is a relatively more controlled process with better control over evaporation rate and less probability of contamination [58]. Comparable refractive index has been obtained by PIAD technique [59] where an additional plasma source was used to bombard the e-beam evaporated film in-situ.

In the present study [60], reactive evaporation of alumina (Al_2O_3) has been successfully carried out in the indigenously developed e-beam evaporation system and this study has been carried out to obtain the optimum oxygen flow rate or partial pressure to achieve good quality films with reasonably high refractive index. Optical and morphological properties of the films have been studied by Spectroscopic Ellipsometry (SE) [61-65] and Atomic Force microscopy (AFM) [66-68], while densities of the films have been determined by Grazing Incidence X-ray reflectivity (GIXR) [69-70] and atomic ratios of oxygen to aluminum have been estimated by X-ray Photoelectron Spectroscopy (XPS) [71-73] measurements.

2.2 Contribution of the thesis

The process control of EBPVD based coating system is highly dependent on the performance of each subsystem of the EBPVD system. Though the electron gun technology has been evolving over the last few decades, there are several distinct specialized areas which require systematic investigation of electron gun. The motivation behind our work is to address the following problems to address hardware and computational issues which enhance EBPVD capabilities. Our work, if we may say, incrementally adds features in hardware meant for

EBPVD and produces desirable results not possible without these additions. These are outlined below.

- Design of high power electron gun which is suitable for high power evaporation system,
- Unhindered operation of the electron gun for nonmetallic coating to operate in an ambient of 10^{-1} Pa to 10^{-2} Pa so that stoichiometry issue can be tackled,
- Mechanism to protect high power source from breakdown to enable uninterrupted operation of electron gun, and
- Finally, we validate the effectiveness of the stoichiometry control through experimentation and characterization of a representative coating.
- Computation of vapor flux distribution at the deposit substrate using CFD to achieve more accurate thickness distribution in the deposited film. However, this is computational work in contrast to the hardware developmental work reported above.

The electron gun plays the most important role, therefore in this work the major emphasis is on the design of the electron gun. Electron beam evaporation system is generally 270^{o} bent beam type. Depending on the application the system is either high power type or low power type. For high power gun, the contribution in this thesis has been on an emitter design which overcomes the shortcomings of directly heated filament. The emission from directly heated cathode suffers due to cathode distortion and self-induced magnetic fields resulting in non-uniform distribution of heat flux on the work surface. In this direction the contribution has been on design of an indirectly heated cathode that provides longer cathode life and uniform temperature distribution over the cathode emitting area of interest.

In the low power regime, there has been significant contributions by various researchers. In this thesis, the emphasis has been given on gun design for reactive evaporation, which is carried out in the pressure range between 10^{-1} Pa to 10^{-2} Pa. At this high pressure the electron gun does not operate reliably due to high voltage flashover. To overcome this problem substrate chamber is isolated from gun chamber using a bifurcation plate. Using the differential pumping arrangement the gun chamber pressure is maintained at better than $5x10^{-3}$ Pa, whereas substrate chamber pressure is in the range between 10^{-1} Pa to 10^{-2} Pa. The coating experiment of alumina is carried out as reactive evaporation. Evaporation of alumina results in dissociation and loss of oxygen and hence reactive evaporation under oxygen-ambient has been carried out to compensate the oxygen loss. Pure (better than 99.9 %) quality oxygen gas (O_2) has been bled in the system during deposition and films have been deposited at various oxygen flow rates. Variations of the different properties of the Al_2O_3 films have been studied as a function of O_2 flow rate and the results of the different findings have been corroborated with each other. This study was to obtain the optimum oxygen flow rate or partial pressure to achieve good quality films with reasonably high refractive index.

The design of the electron gun to reduce process interruptions due to breakdown has been taken up. Besides process degradation, this phenomena poses threat to the feeding power source and associated control electronics. While breakdown probability can be reduced drastically through optimized field configuration and gun operating condition, breakdowns cannot be always eliminated completely. Hence, additional measures need to be provided to control after effects of the breakdown. In this thesis, ferrite beads have been used on both the feed cables to attenuate the breakdown current near the gun so that it does not propagate to the power source to cause any detrimental effect. The use of ferrite beads in both the conductors, as used in this work, offers attenuation to both common mode and also differential mode noise signals. The ferrite beads have been used to suppress the high frequency content through dissipation and also to reduce the amplitude of the breakdown signal. After the high frequency is filtered out and the surge amplitude is reduced, protection capacitors can take care of the balance protection requirements. Using the ferrite bead DC passes fully, but rejects best between 1-10 MHz and somewhat lesser extent a decade above and a decade below. Ferrites in this work act like a broadband reject filter without a sharp cut off.

2.3 Organization of the thesis

Electro-dynamic and thermo-mechanical design issues of indirectly heated cathode strip (110 mm length) electron gun and the details have been presented in Chapter 3. In the Chapter 4 the design of 270^{o} bent beam electron gun of non- axisymmetric configuration using non-uniform magnetic field to operate in an ambient of 10^{-1} Pa to 10^{-2} Pa has been presented. CFD modeling has been used for non-uniform temperature distribution on the evaporant surface. Also the reactive evaporation of yttria has been modeled using CFD. A detailed analysis of the breakdown signal has been presented in the Chapter 5. Reactive evaporation of Al_2O_3 films have been deposited in the indigenously developed e-beam evaporation system and this has been elaborated in the Chapter 6. The conclusion of the work has been enumerated in the Chapter 7 and also the future direction of the work is reported in this Chapter.

CHAPTER 3

Indirectly heated cathode for strip type electron gun

Strip electron beam is being increasingly used in multitude of industrial application involving surface modification through evaporation route. Electron gun is the most critical element because it not only acts as a source of electrons, but is also responsible for the primary shaping of the beam thereby regulating the incident power density on target. The electron gun can be directly heated type filament or indirectly heated type solid cathode. Due to thermal expansion, directly heated filament has the inherent disadvantage of filament distortion, change of shape and movement with respect to the focusing electrode. Moreover, directly heated filament generates strong self-induced magnetic field due to the filament heating current. The effects of cathode distortion and self-induced magnetic fields result in non-uniform distribution of heat flux on the work surface. On the other hand, indirectly heated type solid cathode guns are not besiezed with these issues resulting in uniform heating and longer electrode life. However, due to heat loss from the holding section of the solid cathode, considering first order heat effects, the temperature of the solid cathode tapers off from the centre to the edges along the length of the solid cathode resulting in smaller beam length on the target. In this research, attempts have been made to achieve 1) one to one correspondence between the solid cathode and the beam length 2) uniform current density by achieving uniform temperature on solid cathode. The uniformity of temperature on solid cathode depends not only on its structural design, its geometrical shape and thickness, but also on the near uniform heat flux arising out of filament to bombard the solid cathode. An indirectly heated cathode gun involves incorporation of one more electrode. The solid cathode is at positive higher potential than filament and floated at high acceleration voltage. The solid-cathode holder assembly must maintain its structural integrity during this high temperature operation and also minimize conduction heat loss from the solid-cathode. Here, a few electro-dynamic and thermo-mechanical design issues in a solid cathode strip (110 mm length) electron gun have been addressed. The critical issues examined include

- temperature uniformity on the surface of the cathode
- acceptable thermo-mechanical stress
- electron bombardment on solid cathode

3.1 Design basis

The major design features of the indirectly heated cathode are the following.

- It should be capable of providing desired power density.
- Temperature distribution should be uniform, namely, the difference in maximum temperature and minimum temperature must be less than 150 K (~5 %), over the entire length of the emitting surface.
- Cathode should not buckle/deform at the operating temperature
- Thermal stress should be in tolerable limit (Von Mises Stress) depending on the chosen material.
- Focusing electrode and the cathode should be optimally designed for a tailored beam interaction both through control of filament- cathode and cathode-anode target space.
- Avoidance of thermal runaway condition by working in the space charge limited zone.

3.2 Design of solid cathodes

In the design analysis five major variants of solid cathodes as detailed below have been examined. Each solid cathode is assembled with sliding contact with the focusing grid so that any deformation due to thermal expansion is avoided. The tantalum filament with emitting cross section of 110 mm x 3 mm, multi-segment type (made from six segments) is mounted 5 mm behind the solid cathode.

3.2.1 Rectangular Cathode with Rectangular Holdings without Fins (RCRHWF)

The solid cathode has a dimension of 194 mm x 4 mm x 2 mm with an emitting surface of 110 mm x 4 mm. A schematic of this cathode is shown in the Fig 3.1. The figure shows the holding part, middle section and the emitting area of the solid cathode. The holding part is in sliding contact with the focusing grid. The solid cathode, which is at a potential of 1.5 kV, is bombarded by the electrons emitted from the filament thereby raising the temperature of the solid cathode. The uniformity in temperature in the emitting area has been improved by modifying the holding section.

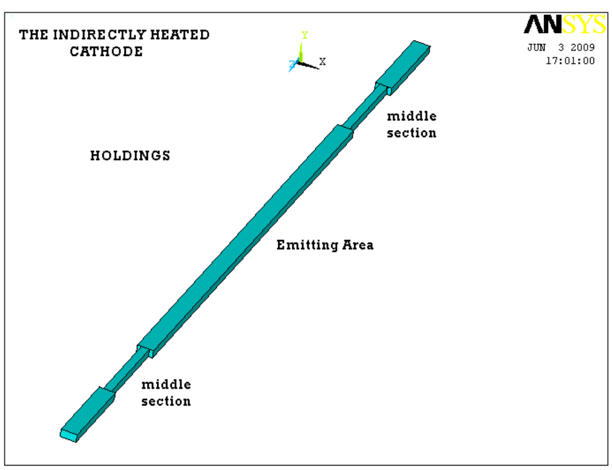

Fig. 3.1 Schematic of a solid cathode

3.2.2 Rectangular Cathode with Rectangular Holdings with Fins (RCRHF)

Fins (slots to reduce the contact area) have been provided at the holding section of the rectangular cathode to reduce the conduction from the solid cathode to the grid cup which acts as thermal resistance. This not only reduces the grid cup heating, but also provides better uniformity in temperature. Engineering drawing of cathode is shown in the Fig. 3.2 (a).

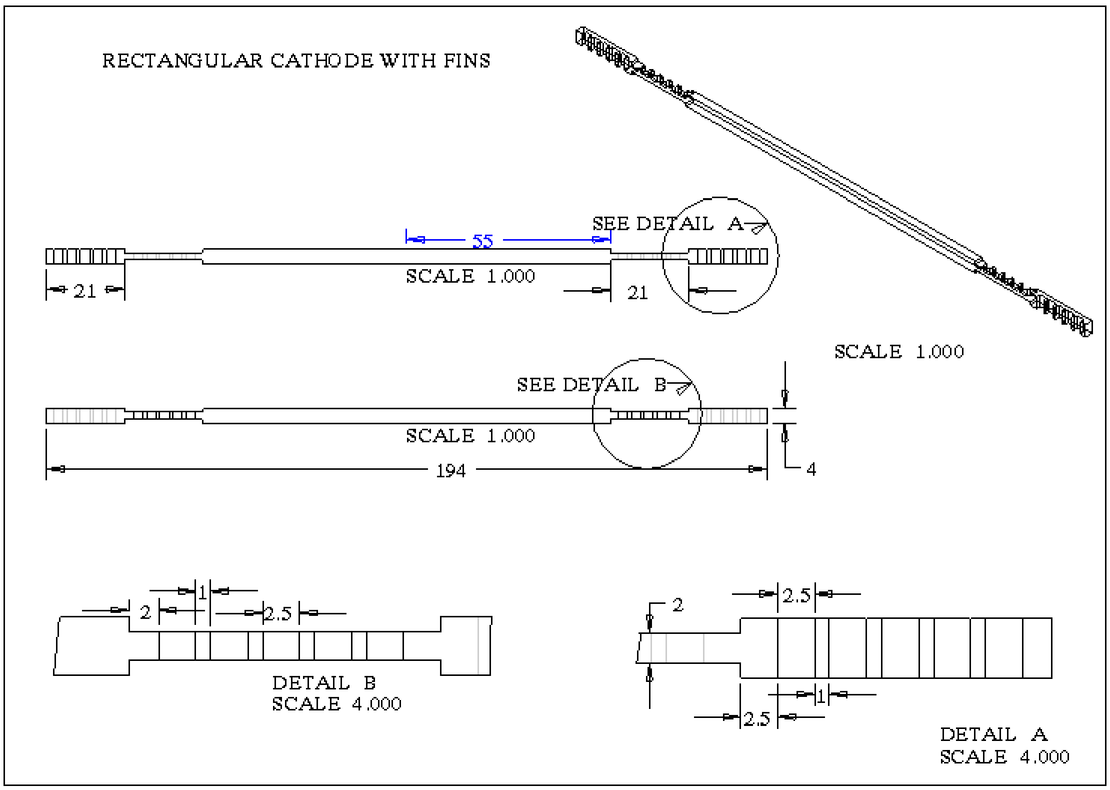

Fig. 3.2: (a) Drawing of rectangular cathode with rectangular holdings with fins

The solid model of this cathode is shown in the Fig. 3.3 (a) and the fabricated cathode is shown in the Fig. 3.4 (a). The fabricated focusing grid is shown in the Fig. 3.4 (c). Through the electron bombardment from the filament, the temperature of the solid cathode is raised to the emission temperature. Further, the EHT (40 kV acceleration voltage) is applied to extract the electron beam from the solid cathode. This results in multiple electron beam not only from the solid cathode, but also from the filament behind the solid cathode, which is undesirable. This happens due to the annular gap between the solid cathode and the focusing grid. Through this annular gap some electrons from filament escape, as they are influenced by EHT. So the main beam consists of not only electrons from solid cathode but also electrons from filament.

3.2.3 Trapezoidal Cathode with Trapezoidal Holdings without Fins (TCTHWF)

In order to tackle the problem of multiple beam in rectangular cathode, the solid cathode has been designed with trapezoidal cross section. The problem of escaping electrons in rectangular design is taken care by the trapezoidal cathode due to its slant lock between the sides of the cathode and the focusing grid. This ensures single stable beam. The solid model of this cathode is shown in the Fig. 3.3 (b).

3.2.4 Trapezoidal Cathode with Trapezoidal Holdings with Fins (TCTHF)

The solid cathode of trapezoidal cross section achieves better uniformity in temperature when fins are provided at the holding side. In this design the cross section of fins are trapezoidal. The solid model of this cathode is shown in the Fig. 3.3 (c). The engineering drawing for this cathode is shown in the Fig. 3.2 (b) and the grid cup for the trapezoidal cathode is shown in the Fig. 3.2 (c).

3.2.5 Trapezoidal Cathode with Rectangular Holdings with Fins (TCRHF)

The solid cathode of trapezoidal cross section with rectangular holding offers fabrication ease. The solid model of this cathode is shown in the Fig. 3.3 (d) and the fabricated solid cathode is shown in Fig. 3.4 (b). Rectangular holding offers less contact area with the focusing grid. Therefore the heat conduction loss at the end of the cathode to the focusing grid is reduced. Electrons emitted from the filament do not escape in this configuration providing better bombardment efficiency. So it is conceived that the uniformity in temperature and other relevant properties would be better with this configuration. This has been validated through simulation and experimentation. The solid cathode- grid cup assembly is shown in the Fig. 3.5.

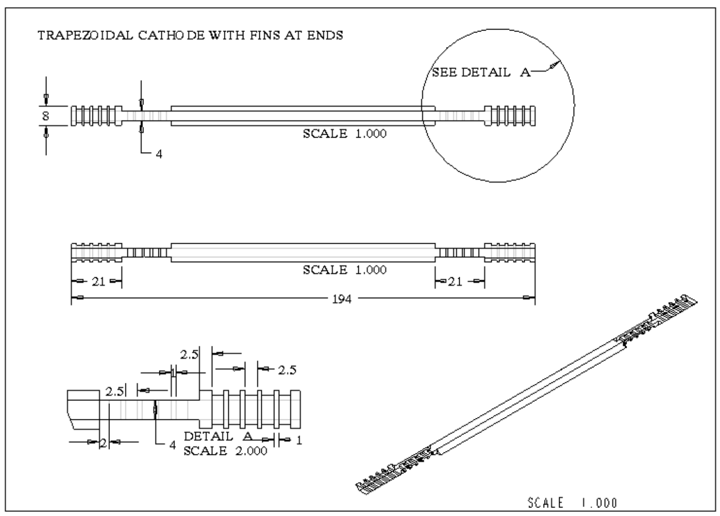

Fig. 3.2: (b) Detail drawing and views of trapezoidal cathode with fins

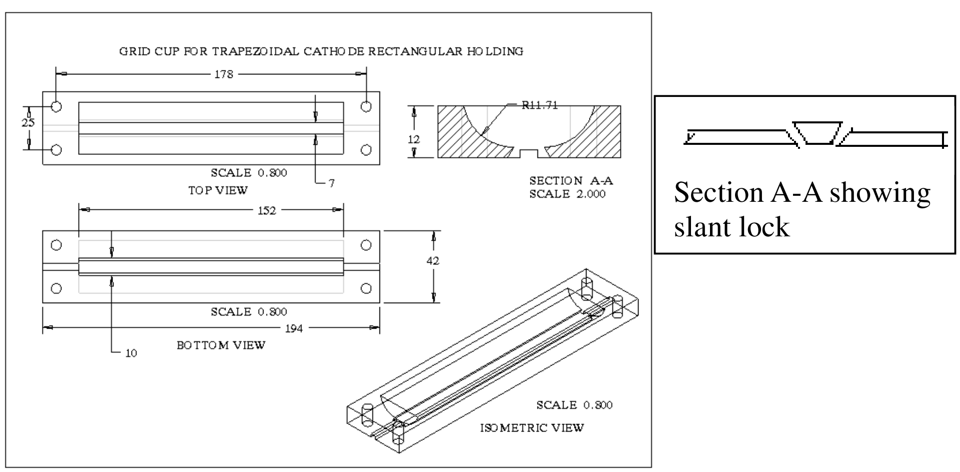

Fig. 3.2 : (c) Detail drawing and views of grid cup for trapezoidal cathode

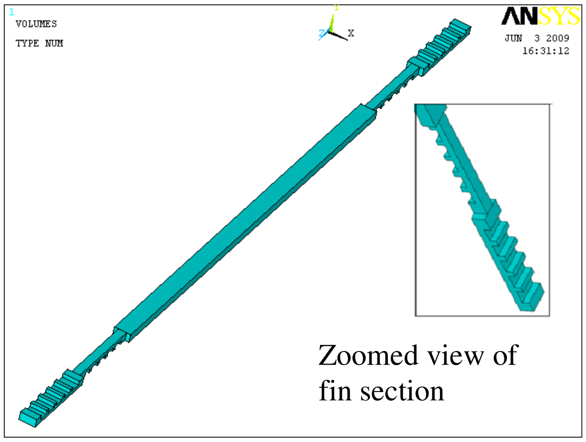

(a)

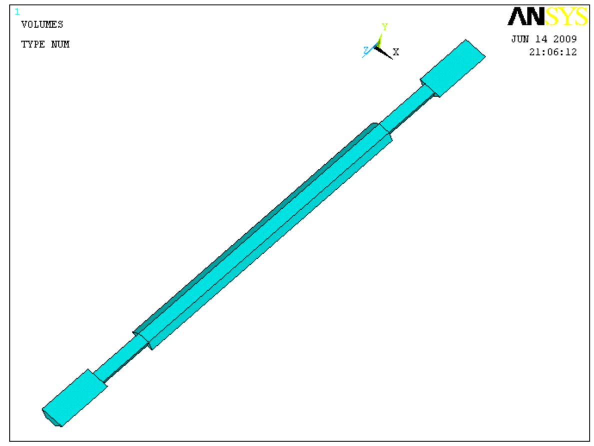

(b)

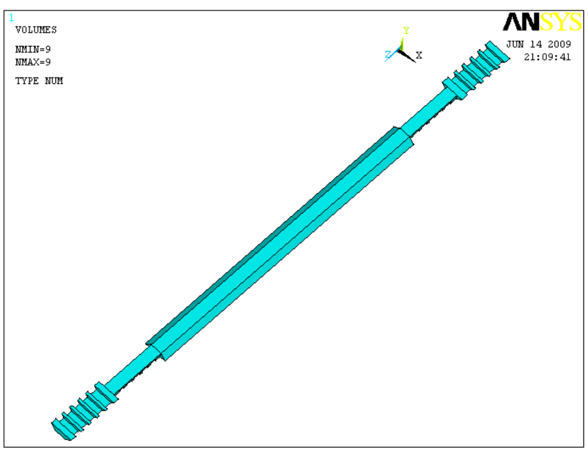

(c)

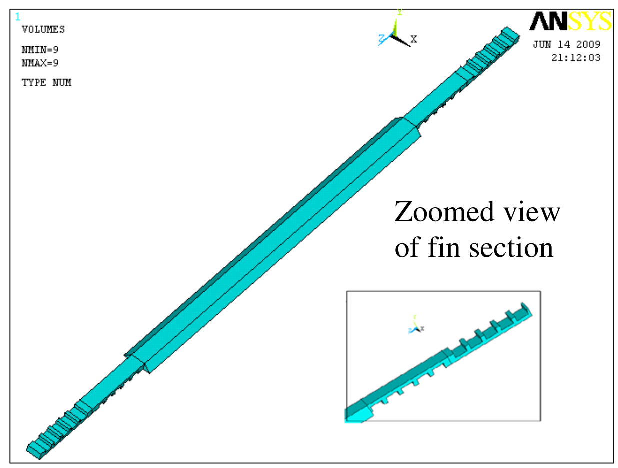

(d)

Fig.3.3 Solid model of different solid cathodes. (a) RCRHF (b) TCTHWF (c) TCTHF (d) TCRHF.

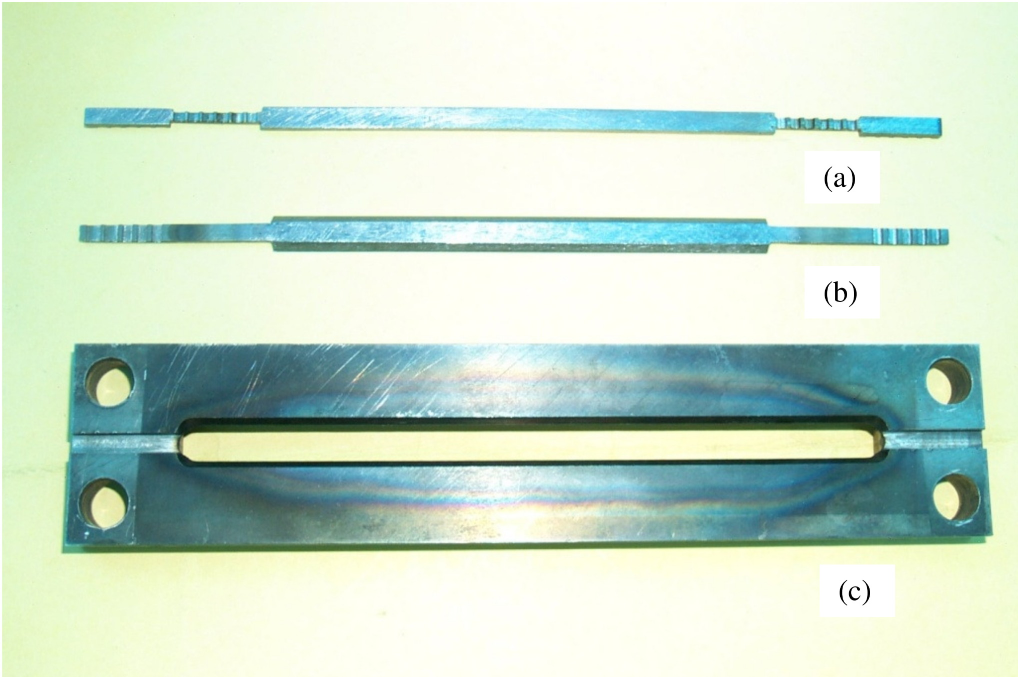

Fig 3.4 Solid cathodes and the grid cup. (a) Fabricated rectangular cathode RCRHF. (b) Fabricated trapezoidal cathode TCRHF. (c) Focussing grid.

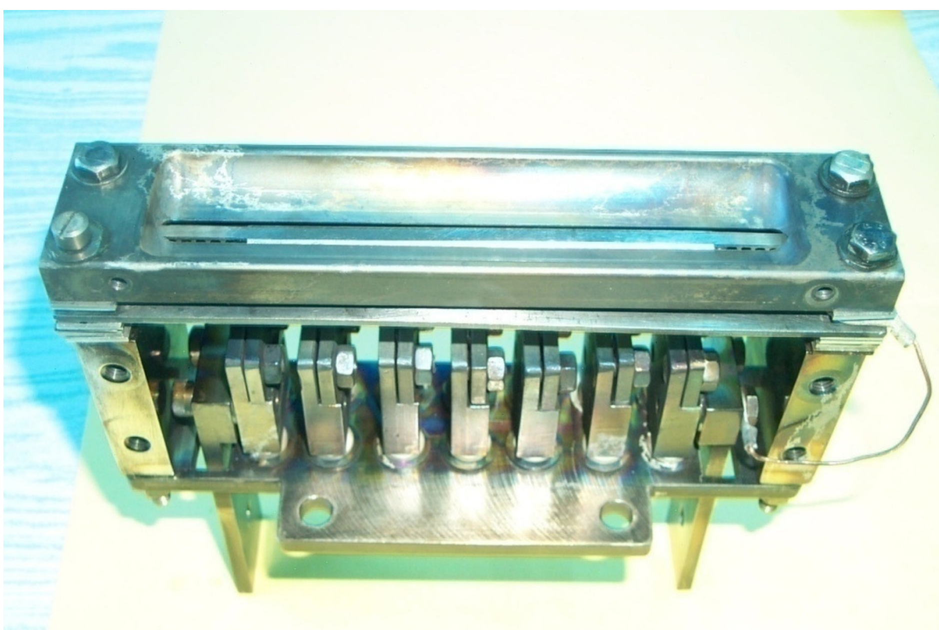

Fig 3.5 Solid cathode grid cup assembly.

3.3 Beam trajectory simulation

For tailored beam trajectories in the filament-cathode space, simulation has been carried out using an electron optics software EGUN© by SLAC [13]. This software calculates trajectories in electrostatic and magnetostatic fields. Poisson's equation is solved by finite difference equations using boundary conditions defined by specifying the type and the position of the boundary. Electric fields are determined by differentiating the potential distribution. Space charge calculations are done using Poisson's equation. Then the program uses four step Runge-Kutta method of solving the relativistic differential equations to compute the trajectories. POLYGON© translates the boundary conditions and the input parameters and provides the input to EGN2W©. EGN2W in turn computes the equipotential lines and the electron trajectories in the derived electric field. The electron trajectory and the current density are calculated in EGN2W and the output plots provide the desired information. The current density on the solid cathode largely depends on how the electrons emitted from the filament bombards the solid cathode.

To start with, a rectangular solid cathode with directly heated filament and a flat focusing electrode at the same potential as filament has been used for simulation. The electron trajectory from filament to the solid cathode is shown in the Fig. 3.6 (a) and the current density on the solid cathode is shown in the Fig. 3.6 (b). Fig. 3.6 (a) and 3.6 (b) show that a significant part of the electrons come out through the slit between the solid cathode and the focusing grid. This results in multiple beam on the target. The edge electrons have bunching effect, so the current density is highly non uniform as seen in Fig. 3.6 (b). So the filament focusing electrode has been optimally designed so that all the electrons coming out from the filament bombard the solid cathode as shown in the Fig. 3.7 (a). The current density distribution in the Fig. 3.7 (b) shows the near uniform distribution.

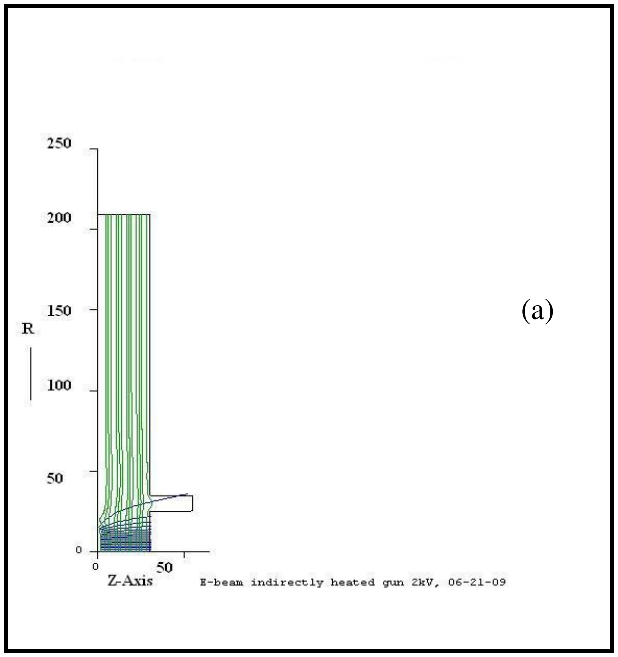

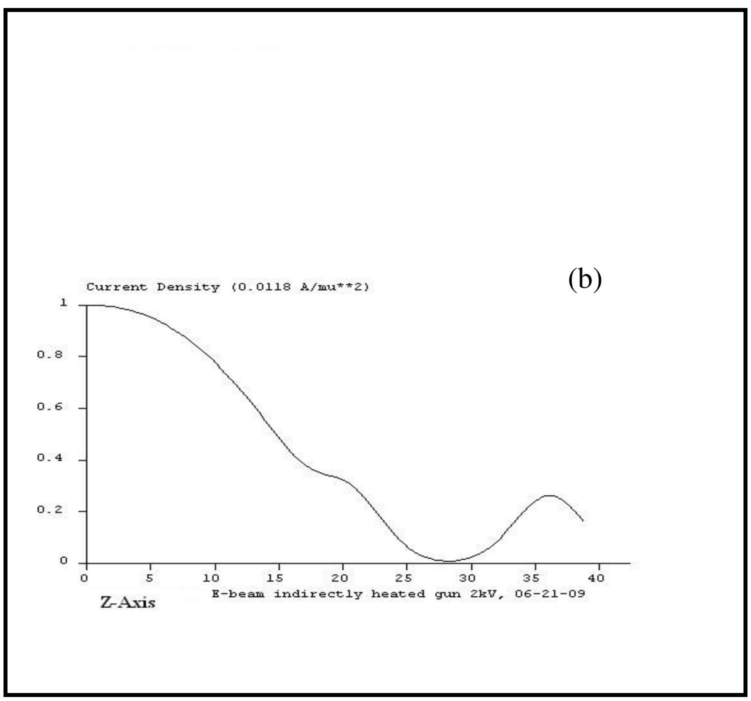

Fig 3.6 Electrons coming out from the annular space between the solid cathode and the grid cup (10 times magnified scale i.e. 50=5mm). (a) Electron trajectory plot. (b) Current density plot

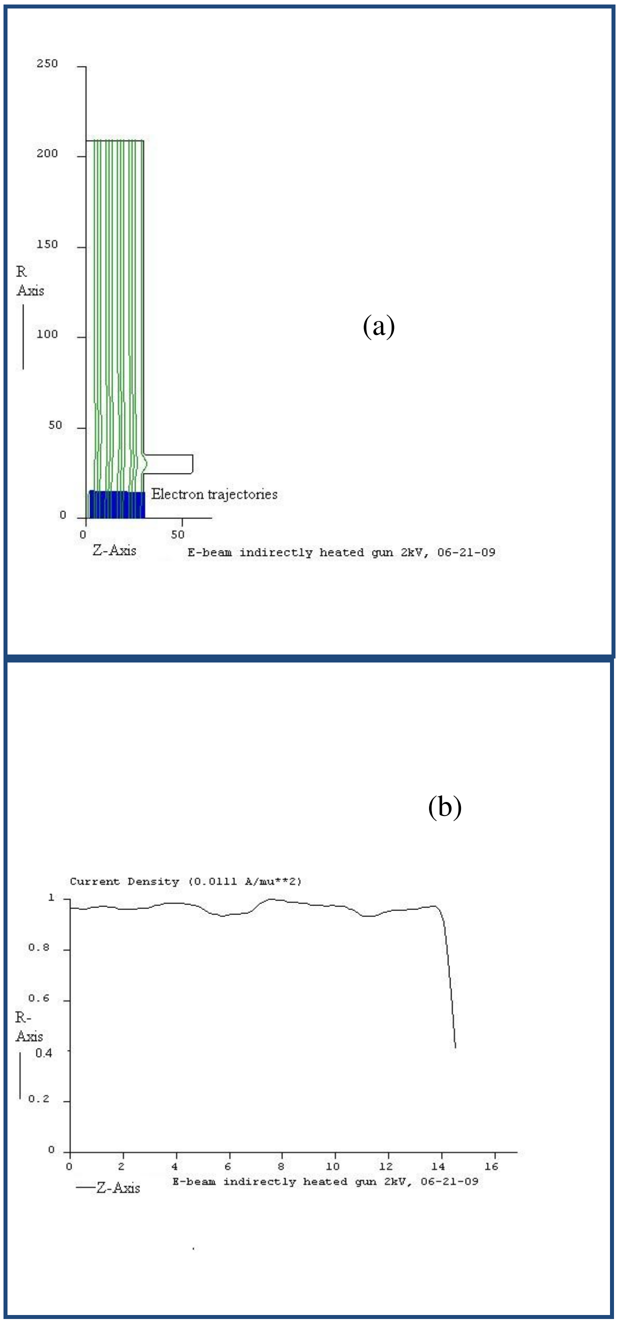

Fig. 3.7 Electrons are focused on to the solid cathode with near uniform current density (10 times magnified scale i.e. 50=5mm). (a) Electron trajectory plot. (b) Current density plot

3.4 Thermal model and analysis

A systematic thermal analysis approach has been adopted to arrive at an optimum solid cathode design. The schematic of an indirectly heated cathode model [12] is shown in the Fig. 3.8. The tantalum filament gains power by resistance heating from a DC source. It emits electrons on reaching the emission temperature. The emitted electrons are attracted towards the solid cathode due to relative positive potential of solid cathode with respect to the filament. Solid cathode gains power by electron bombardment and radiation heat from the filament. It loses power simultaneously by radiating heat to its surroundings and to sub-assemblies (focusing grid electrode and supports). Solid cathode will also loose heat by conduction to the grid cup as it slides over the grid cup.

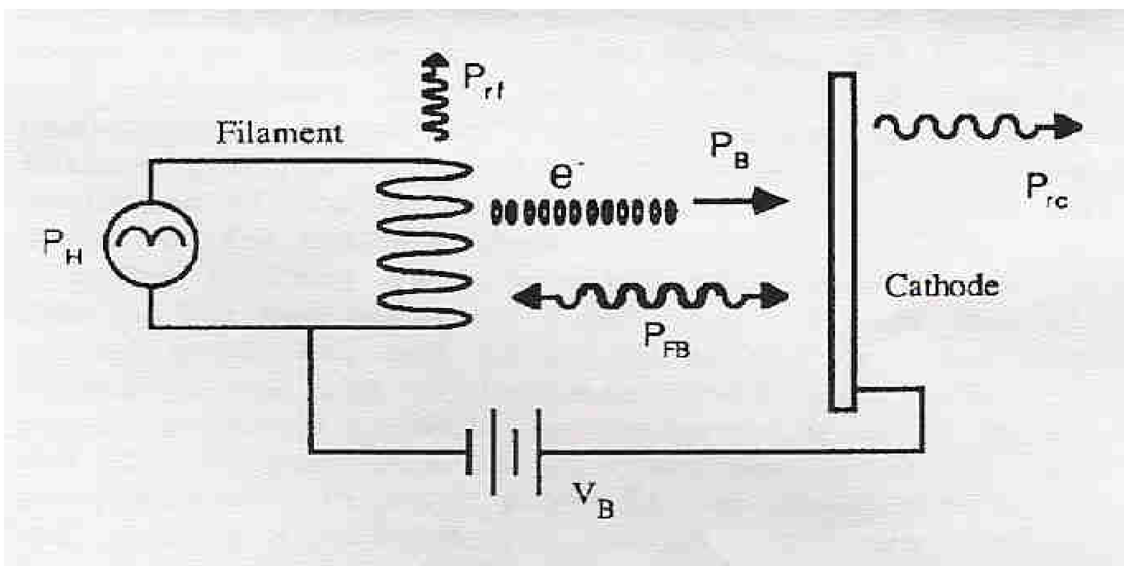

Fig 3.8: Schematic of an indirectly heated cathode model.

So the power balance equation for the solid cathode is as follows.

$$C_c \frac{dT_c(t)}{dt} = q + P_1 - P_2 - P_3 \tag{3.1}$$

$$q = I_b . V_b \tag{3.2}$$

Where ,

C_c = Specific heat of cathode,

T_c = Cathode temperature,

q = Power received from the filament to the solid cathode by the electron bombardment

V_b = Bombardment voltage

I_b = Electron current density

The electron current density is given by Richardson-Dushmann Equation

$I_b = C.T_f^2.\exp\left[\frac{-q\phi}{kT_f}\right]$

where, T_f = Filament temperature

C = Constant depends on the material

P_1= Heat input on the solid cathode due to radiation heat exchange with surrounding interacting surfaces having temperature higher than the solid cathode is same as the radiation heat input from the filament to the solid cathode. Hence,

$$P_1 = A.\varepsilon.\sigma.\left\{\left(T_f(t)\right)^4 - \left(T_c(t)\right)^4\right\}.F_{ij} \qquad (3.3)$$

A = heat transfer area

F_{ij} = view factor and is defined as the fraction of the radiation power leaving surface i and is intercepted by surface j

ε = Emissivity

t = Time

σ = Stefan- Boltzmann's constant = $5.67\ X\ 10^{-8} W/mK^4$

$T_f(t)$ = Filament temperature

$T_c(t)$ = Solid cathode temperature

P_2 = Heat output from solid-cathode due to radiation heat exchange with surrounding interacting surfaces with temperature lower than the solid-cathode,

$$P_2 = P_{21} + P_{22} + P_{23} + P_{24} = \sum_i \varepsilon.\sigma.\left\{\left(T_f(t)\right)^4 - \left(T_c(t)\right)^4\right\}.A_i.\,F_{2j} \qquad (3.4)$$

where,

P_{21} = Radiation heat transfer from the solid-cathode to grid Cup

P_{22} = Radiation heat transfer from the solid-cathode to grid cup supports

P_{23} = Radiation heat transfer from solid-cathode to other assemblies

P_{24} = Radiation heat transfer from the solid-cathode to space node

A_i = Heat transfer area of Interacting surface

F_{2j} = View factor between the interacting surfaces of the solid cathode and the j^{th} surface.

$P_3 =$ Conduction heat loss from the sold cathode to the sub-systems in contact,

A finite element software package ANSYS is used to deal with the thermo-structural modeling problem in which the radiation plays an important role during the period the solid cathode gets heated. The radiation matrix method is used to calculate the surface-to-surface radiation. Though the method takes more memory for its calculations and computations, it is the most accurate method to deal with the radiation problems. The method uses the basic Stefan Boltzmann's law as its governing equation for modeling the radiation. To include radiation effects in elements, the substructure element is used to bring in the radiation matrix. Then with the radiating surfaces and space node defined, substructure radiation matrix is created.

Solid modeling of the cathode and other sub assemblies (Fig. 3.9) is done in ANSYS itself. The process of discretization has been carried out for grid generation in finite element method. The size of the mesh plays a part in the accuracy and the convergence of results but only up to a certain extent. Finer the mesh size the better will be the accuracy of results. So, here 10 node solid tetrahedral elements have been taken to generate the mesh. For the radiation modeling, tetrahedral mesh is superimposed with shell elements to define the radiating surfaces.

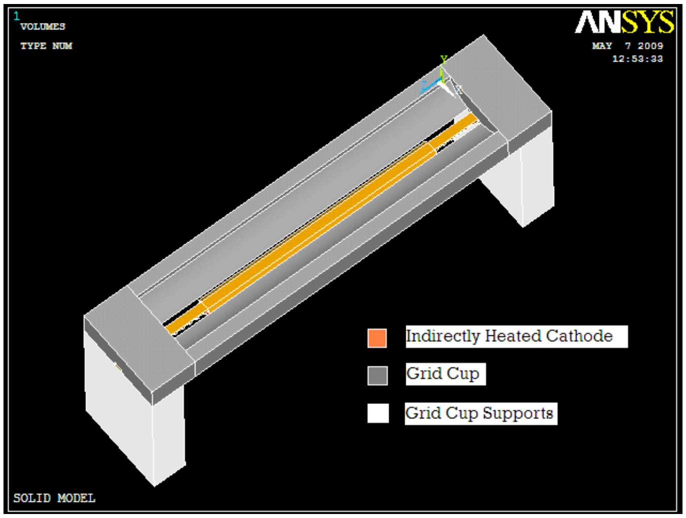

Fig 3.9: Solid model of solid cathode-grid assembly

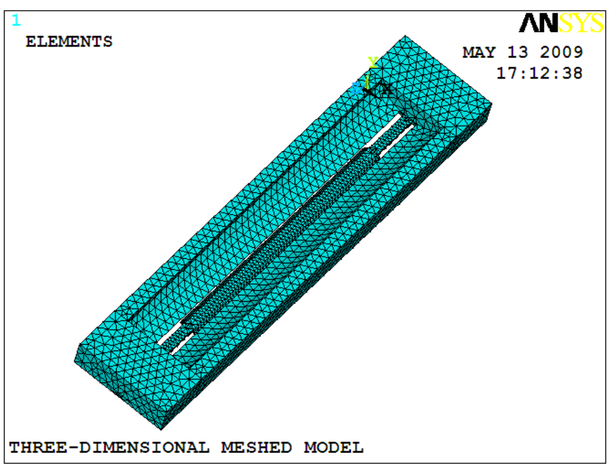

Fig 3.10: 10 node solid tetrahedral element mesh superimposed with shell elements.

Substructure element with proper boundary conditions is shown in the Fig 3.10. To raise the solid cathode temperature to 2528 K as per Stefan Boltzmann's law, one requires power of

500 W. This power is achieved by electron bombardment from filament and through radiative heat exchange between filament and the solid cathode. The power through the radiative heat exchange is negligible as both the solid cathode and the filament are at nearly the same temperature. So the bombardment power ($q = V_b.I_b$) mainly raises the temperature of the solid cathode. Through Richardson-Dushman's equation, current density of 0.296 A/cm^2 can be obtained by raising the filament temperature to 2500 K. There is a acceleration potential of 1.5 kV (V_b) between the solid cathode and the filament. Hence the power density (filament current density x V_b) required is 4.44 MW/m^2. Uniform heat flux has been assumed on solid cathode. It has been assumed that 50 % loss will occur on account of backscattering [23] and an additional 10 % on thermal electron, secondary electron etc. Therefore useful heat flux 1.776 MW/m^2 is applied to the solid cathode to attain the desired heating of the solid cathode.

3.5 Experimental set up

The gun assembly with the filament-cathode system has been tested in a vacuum chamber. The vacuum system consists of a diffusion pump backed by a rotary pump giving rise to a vacuum of 1x 10^{-3} Pa. The gun assembly is made of a tantalum filament as primary heat source, filament focusing electrode to shape the electron beam from the filament on to the solid cathode and also to stop stray electrons heating the assembly from sidewise, tantalum solid cathode as indirect heat source, focusing grid to shape the electron beam from the solid cathode so that it comes out as a strip through the anode opening and bent by 270^o by using uniform magnetic field on to the crucible target. A 45 kV, 200 kW power source with auxiliaries such as filament power supply (10 V, 70 A DC, floated at - 45 kV), solid cathode (1.5 kV, 1 A DC, floated at -43.5 kV), power supply for a pair of magnet coils in Helmholtz configuration (300 V, 1 A DC) has been used to energize the electron gun. The anode and the crucible are grounded. Temperature of the filament and the solid cathodes have been recorded using a two color pyrometer.

3.6 Results

First the simulation has been carried out and then the experimental validation has been done. The result of all the five invariants of solid cathode has been discussed below.

3.6.1 Rectangular cathode with rectangular holdings

The temperature distribution of the cathode is shown in the Figure 3.11 (a). The maximum temperature obtained at the emitting surface was 2813 K in the mid section of the area and at the ends it was around 2595 K; the temperature decreased linearly along the length. The end to end uniformity obtained was 218 K (the difference of two temperatures) which is quite high. The reason for this non-uniformity was the heat conduction at the ends of the cathode to the grid cup. The grid cup temperature distribution is shown in Figure 3.11 (b). Looking at the contours one can see the heat flow to the grid cup. The temperature is highest where the cathode is in contact with grid cup. The second mode of heat transfer in this analysis is radiation as the cathode is at high temperature. The temperature in the middle section of grid cup is high in comparison to other sections. To improve the non-uniformity in temperature distribution arising out of conduction, the cathode design has been modified by providing fins (slots) at the cathode ends.

Figure 3.11 (c) shows the temperature distribution contours for the design with fins. The maximum temperature at the centre was almost same at 2813 K but the measured temperature at the ends was considerably better at 2663 K. The end to end uniformity improves by 150 K. The heat transfer to grid cup by conduction was less as compared to heat transfer by radiation from the mid-section of the cathode (Figure 3.11 (d)).

The temperate distribution obtained from the thermal analysis was fed to structure analysis for calculation of stress and deformation. The stress distribution for both configurations (without fins and with fins) is shown in the Figure 3.11 (e) and Figure 3.11 (f) respectively. The stress is very less as compared to the yield strength of the tantalum (150 M Pa) at high temperature. This is because the cathode has not been constrained for the movements in longitudinal direction due to sliding contact. Theoretically, if a material at high temperature is not constrained any where there should be no stress. In this case, the existence of low stress is due to non-uniform temperature on the cathode though there is no constraint.

From the results of both the designs, it is seen that the stress is more in the design without fins as it deforms (longitudinal) less (Figure 3.11 (g)) at high temperatures (within the elastic limit) but when the fins have been provided, the stress decreased at the cost of deformation (Figure 3.11 (h)). This deformation would not produce desired beam shape.

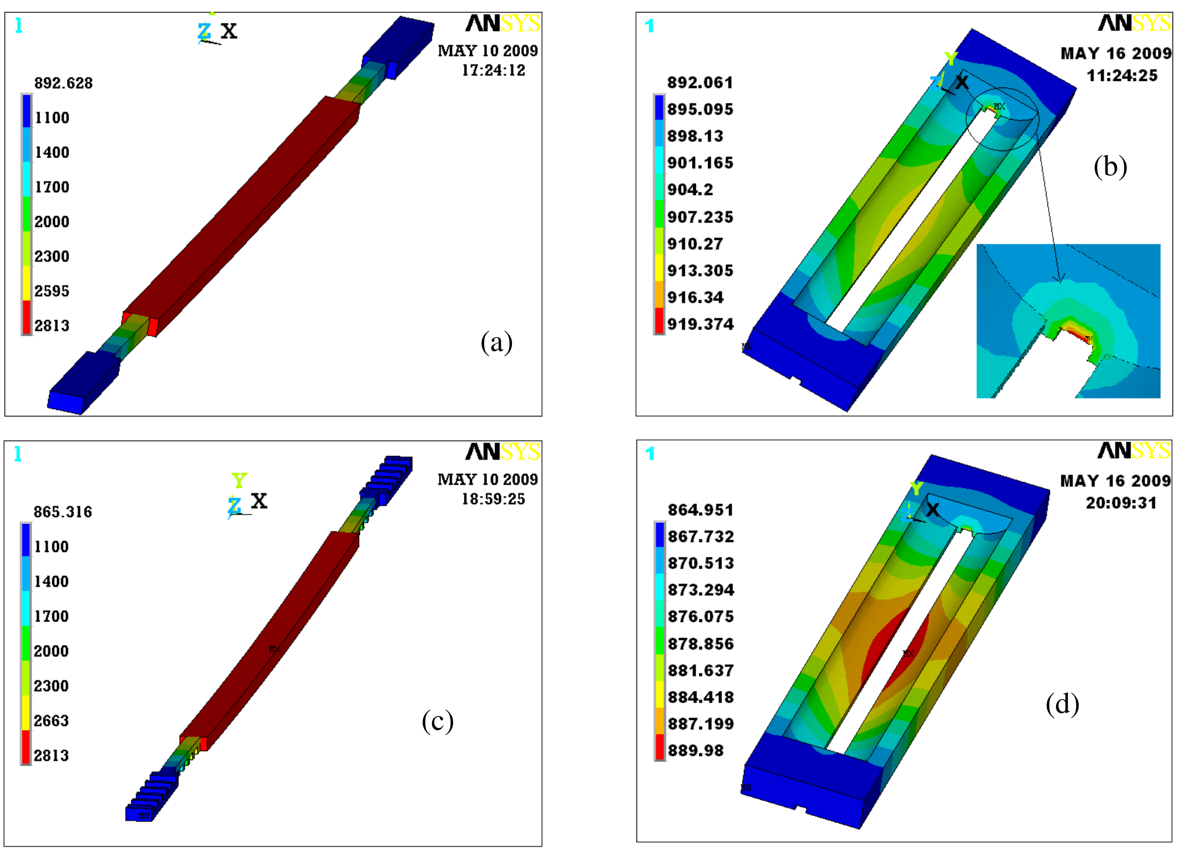

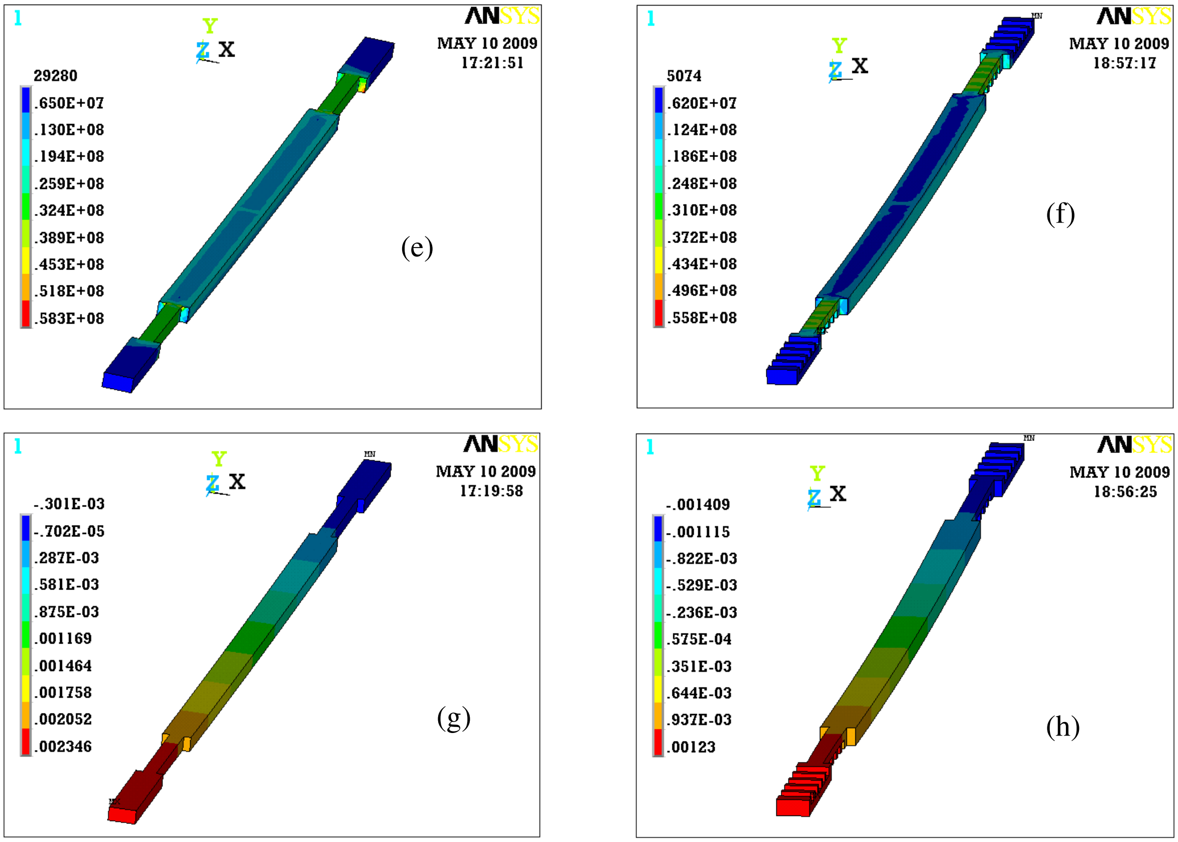

Fig.3.11 Results of rectangular cathode with rectangular holdings. (a) Temperature distribution of RCRHWF (b) Temperature distribution of grid cup of RCRHWF (c) Temperature distribution of RCRHF (d) Temperature distribution of grid cup of RCRHF (e) Stress distribution of RCRHWF (f) Stress distribution of RCRHF (g) Deformation of RCRHWF (h) Deformation of RCRHF.

One more problem with this design was observed during practical experiments. It was seen that during the electron bombardment from the tantalum filament to the lower surface of the cathode, some of the electrons were escaping through the gap between the cathode and grid cup producing an additional beam other than that from the cathode. This produces multiple beams on the target, placed on the crucible which is at 270^{o} location with respect to the gun. This is shown in the Figure 3.12. The cathode design, discussed subsequently, overcomes the shortcomings of the rectangular geometry.

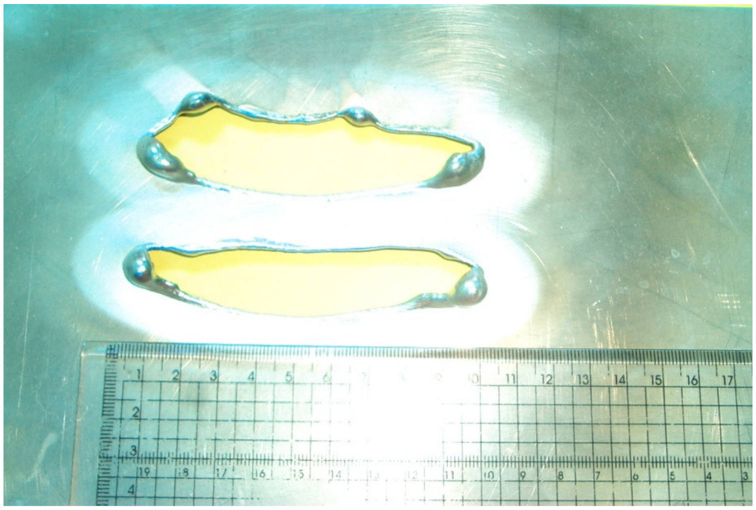

Fig 3.12: Multiple beams on the target due to rectangular cathode.

3.6.2 Trapezoidal cathode with trapezoidal holdings

The temperature contours of the trapezoidal cathode is shown in the Figure 3.13 (a). The temperature obtained in the middle section was 2575 K (less than the rectangular but enough to produce the required beam) and the end to end uniformity found was 255 K which is not acceptable. Also the heat transfer to the grid cup was more compared to rectangular designs as the area of contact was more (Figure 3.13 (b)). Therefore fins were provided in this cathode also and dimensions are also optimized considering the required uniformity and stresses at fins section and connecting ends. The temperature distribution obtained after providing the fins (trapezoidal cross section) in trapezoidal x-section cathode is shown in Figure 3.13 (c). The maximum temperature obtained at the center was same as the trapezoidal design without fins but a considerable improvement at ends is found; the end to end uniformity was calculated as 173 K. The heat transfer to the grid cup (Figure 3.13 (d)) is comparatively less with introduction of fins at the holding section.

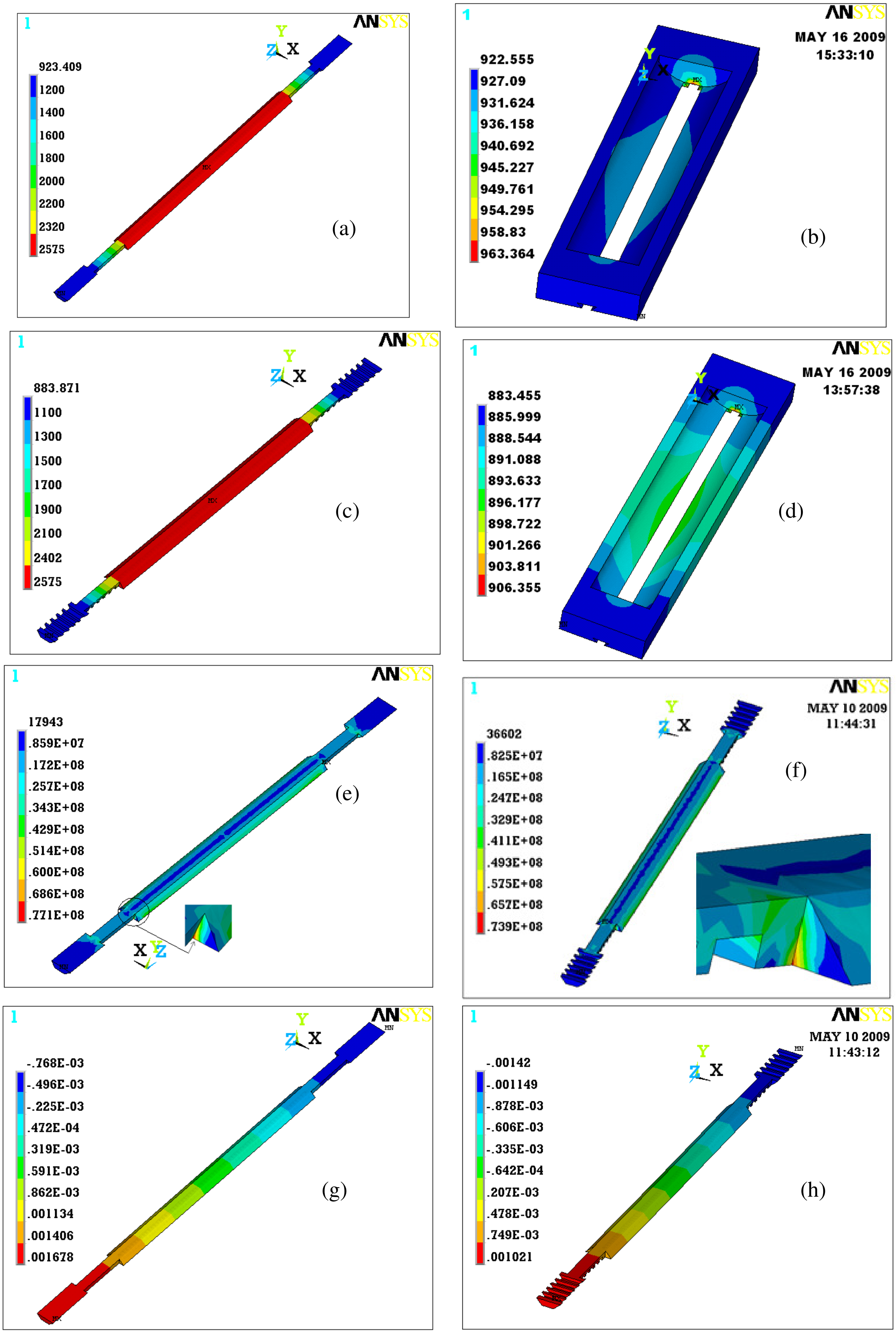

(a)
923.409
1200
1400
1600
1800
2000
2200
2320
2575
(b)
MAY 16 2009
15:33:10
922.555
927.09
931.624
936.158
940.692
945.227
949.761
954.295
958.83
963.364
(c)
883.871
1100
1300
1500
1700
1900
2100
2402
2575
(d)
MAY 16 2009
13:57:38
883.455
885.999
888.544
891.088
893.633
896.177
898.722
901.266
903.811
906.355
(e)
17943
.859E+07
.172E+08
.257E+08
.343E+08
.429E+08
.514E+08
.600E+08
.686E+08
.771E+08
(f)
MAY 10 2009
11:44:31
36602
.825E+07
.165E+08
.247E+08
.329E+08
.411E+08
.493E+08
.575E+08
.657E+08
.739E+08
(g)
-.768E-03
-.496E-03
-.225E-03
.472E-04
.319E-03
.591E-03
.862E-03
.001134
.001406
.001678
(h)
MAY 10 2009
11:43:12
-.00142
-.001149
-.878E-03
-.606E-03
-.335E-03
-.642E-04
.207E-03
.478E-03
.749E-03
.001021

Fig 3.13: Results of trapezoidal cathode with trapezoidal holdings. (a) Temperature distribution of TCTHWF (b) Temperature distribution of grid cup of TCTHWF (c) Temperature distribution of TCTHF (d) Temperature distribution of grid cup of TCTHF (e) Stress distribution of TCTHWF (f) Stress distribution of TCTHF (g) Deformation of TCTHWF (h) Deformation of TCTHF.

The stress distribution for the trapezoidal cathodes (without and with fins) are shown in the Figure 3.13 (e) and Figure 3.13 (f). The value of the stress is more as compared to the rectangular design but this stress is still less than half of the yield strength of tantalum. The deformation is considerably less in the trapezoidal cathodes as compared to the rectangular cathodes as can be seen in Figure 3.13 (g) (without fin) and Figure 3.13 (h) (with fin).

3.6.3 Trapezoidal cathode with rectangular holdings

The design of the trapezoidal cathode has been further improved by providing rectangular holdings (fins with rectangular cross section). The temperature distribution contour of the cathode and the grid cup are shown in Figure 3.14 (a) and Figure 3.14 (b) respectively. The temperature obtained in the middle section was 2575 K (same as the trapezoidal cathode with trapezoidal holding) and the end to end uniformity improved to 149 K. The grid cup temperature is also significantly reduced compared to trapezoidal holding. The stress (Figure 3.14 (c)) and the deformation (Figure 3.14 (d)) are comparable with rectangular geometry.

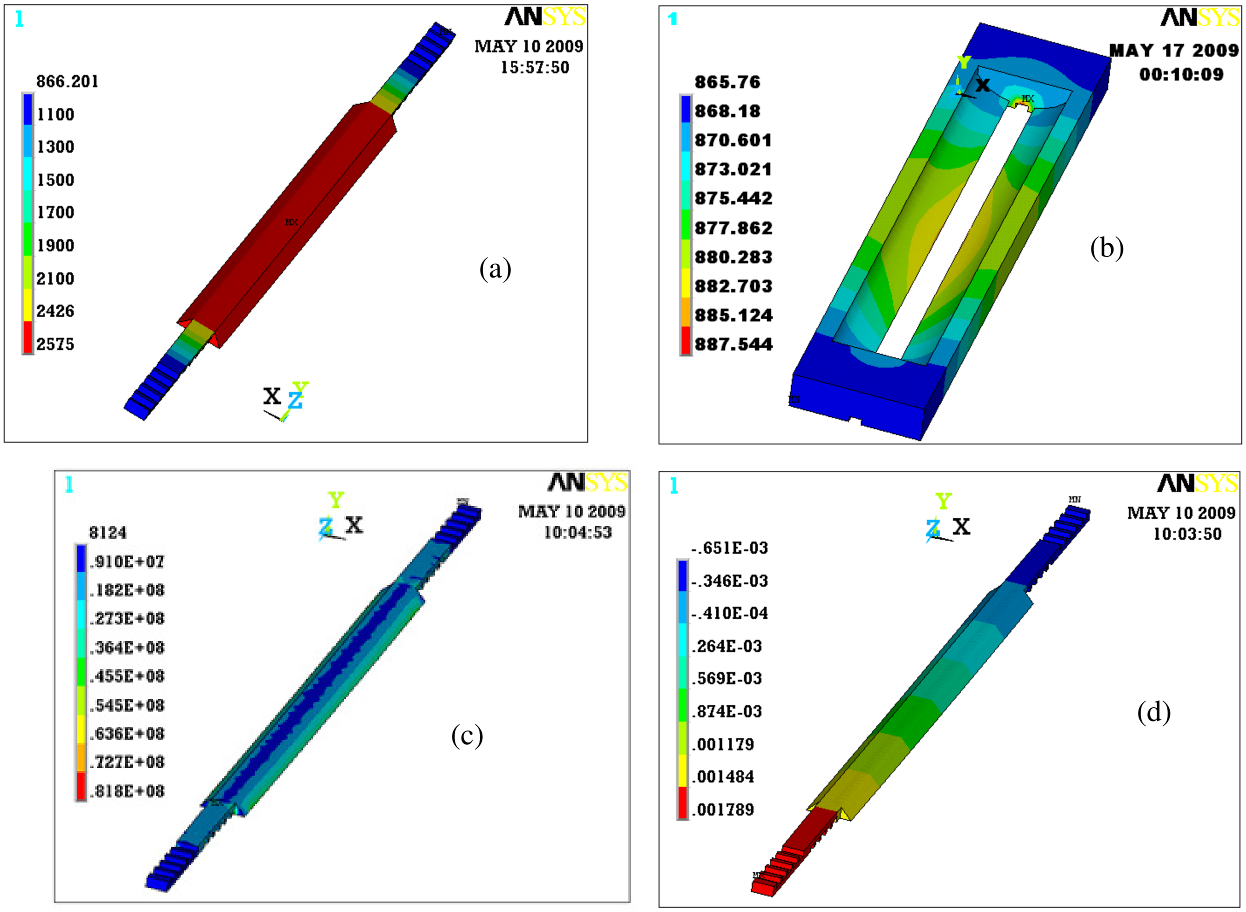

Fig 3.14: Results of trapezoidal cathode with rectangular holdings. (a) Temperature distribution of TCRHF (b) Temperature distribution of grid cup of TCRHF (c) Stress distribution of TCRHF (d) Deformation of TCRHF.

The uniformity of temperature distribution along the emitting length of various solid cathodes is shown in Figure 3.15. Result for the different designs of solid cathodes is tabulated in the Table I. For all the designs the ambient temperature was assumed to be 500 K. Simulations have been carried out at 300 K, 700 K and 1000 K ambient temperatures also. There was no appreciable change in the temperature distribution of the solid cathode. The grid invariance test was carried out by varying the number of elements.

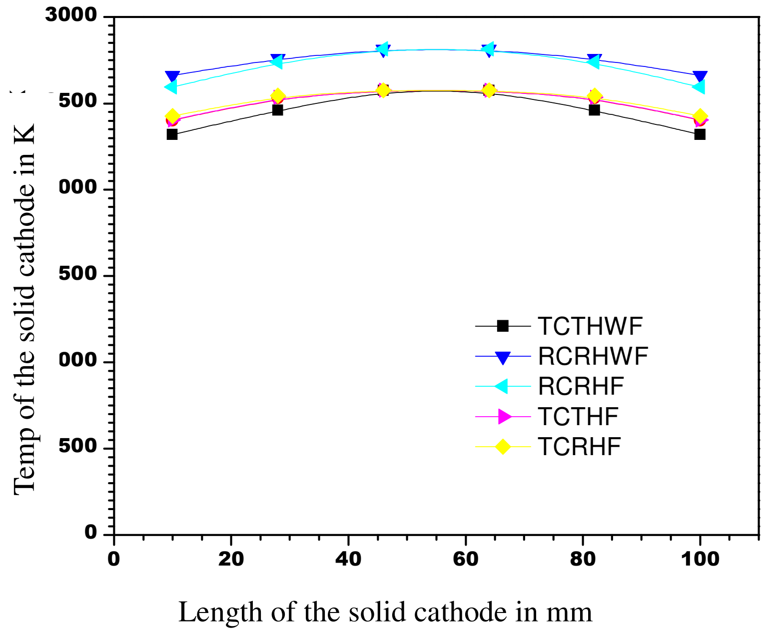

Fig 3.15: Temperature distribution of various solid cathode configurations

Table 3.1: Results for the different designs of solid-cathode

Solid cathode designs	SC_TEMP	UNIFORMITY	GRIDCUP_TEMP	X-DEFORM	Y-DEFORM	Z-DEFORM	VON-MISES STRESS
	K	K	K	mm	mm	mm	M Pa
RCRHWF	2595-2813	218	893-934	0.048	0.12	2.34	58
RCRHF	2663-2813	150	860-890	0.049	0.22	1.41	55
TCTHWF	2320-2575	255	920-963	0.065	0.03	1.68	71
TCTHF	2402-2575	173	880-910	0.065	0.072	1.42	73
TCRHF	2426-2575	149	866-890	0.078	0.098	1.75	81

Several thermal cycling of the solid cathodes have been performed. Temperatures of the solid cathode have been recorded using two color pyrometer along the length of the solid cathodes. The simulated data of the temperature distribution of the rectangular cathode and the experimental data are shown in the Figure 3.16 (a). After a few thermal cycling, sagging of the solid cathode was noticed. Figure 3.16 (b) shows the temperature distribution of the trapezoidal cathode and the experimental data. It shows that they are in close agreement. The stress and the deformation were not noticed through physical verification after several thermal cycles. There was no deformation of the trapezoidal cathode. In each cycle the cathode was kept at a temperature of more than 2500 K for more than 2 hours and there was no thermal rundown. The measured temperature of filament and the solid cathode using pyrometer is shown in the Figure 3.17. To test the uniformity of electron beam, as an initial experiment an axial beam was extracted applying acceleration voltage of 40 kV. Electron beam of cross section 110 mm x 5 mm (approx) could be observed axially at a distance 50 mm from the anode opening. Low power tracer beam on stainless steel plate is shown in the Figure 3.18. This beam traverses in an uniform magnetic field (generated by Helmholtz coils) and is bent by 270^o. Figure 3.18 shows maximum temperature at the extreme left of the beam. This is due to edge electrons from the filament in addition to the electrons from solid cathode. The length of the emitting section of the solid cathode and the filament is same. The narrower middle section of the solid cathode provides escape route to the edge electrons from the filament. This can be taken care by modifying the focusing grid suitably.

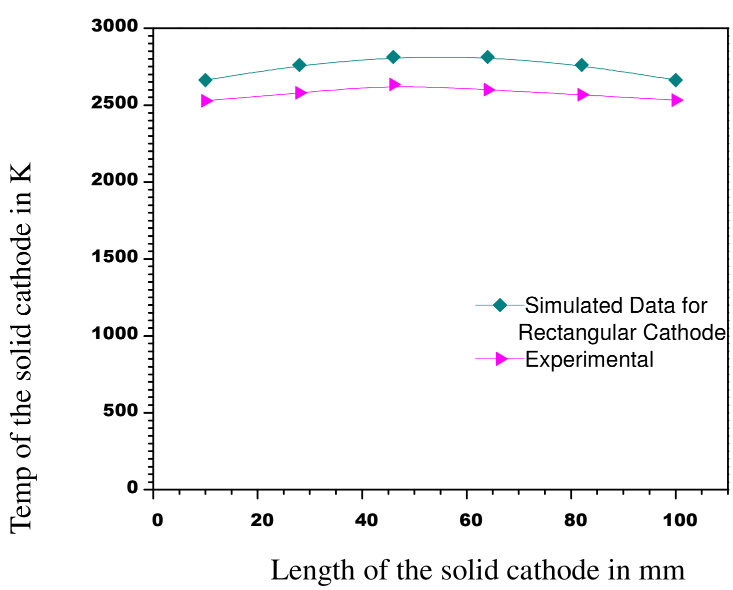

Fig 3.16 (a): Experimental verification of temperature distribution on solid cathode surfaces for rectangular cathode

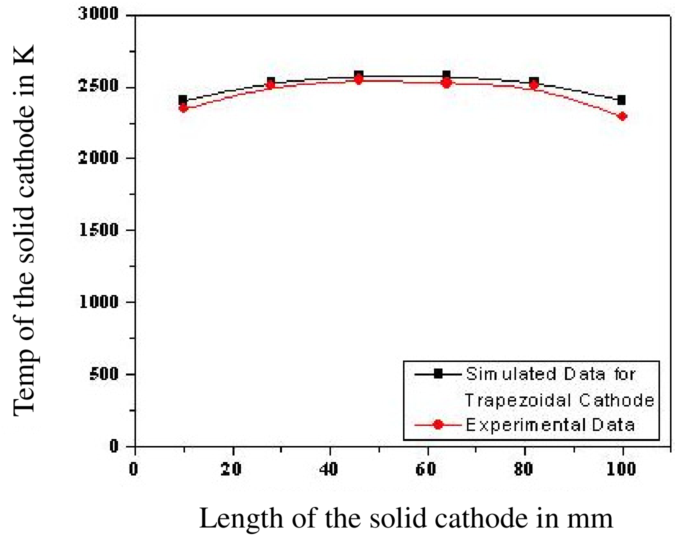

Fig. 3.16 (b) Simulated trapezoidal cathode versus experimental.

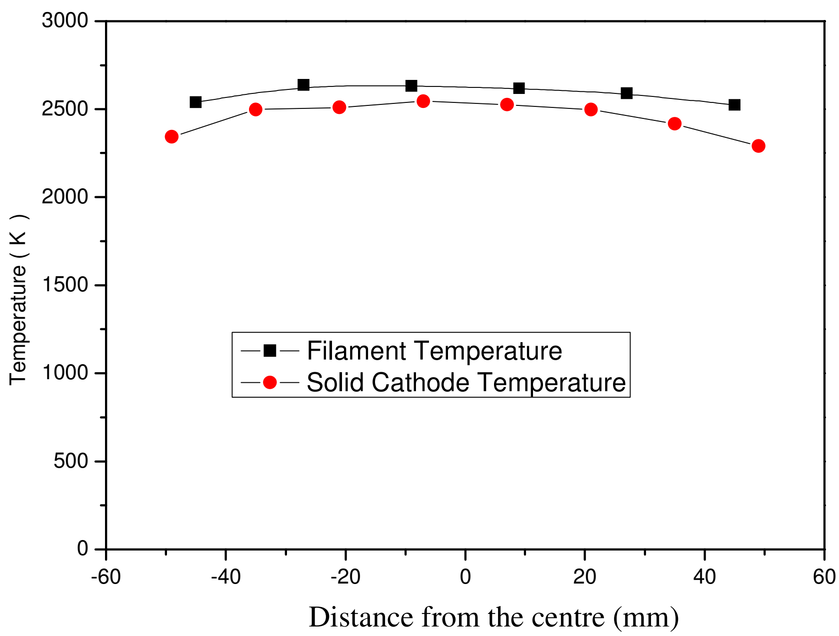

Fig 3.17: Experimental profile of the temperatures of filament and solid cathode

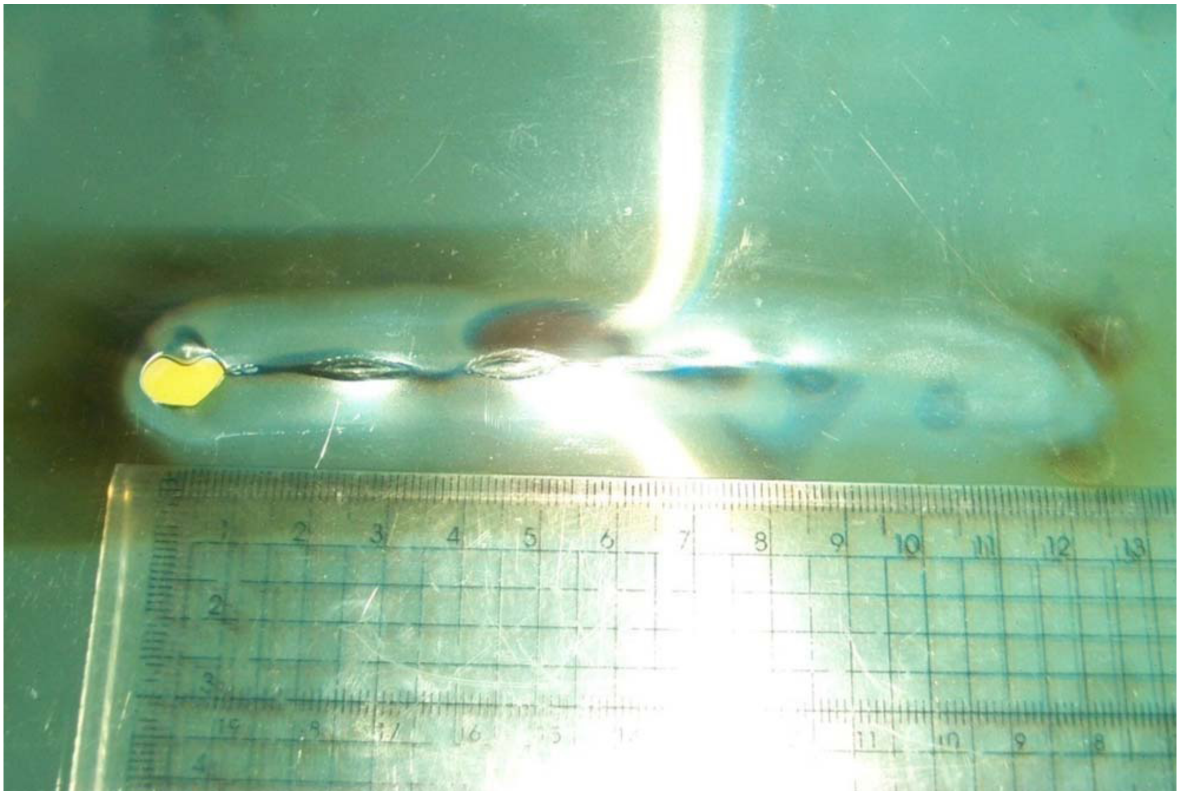

Fig 3.18: Low power electron beam drawn axially on stainless steel plate.

3.7 Discussion

Design issues of an indirectly heated cathode gun has been addressed. An optimized filament focusing electrode has been achieved through electron trajectory simulation and it provided the near uniform current density on the solid cathode. Optimization of solid cathode configuration has been analyzed on the basis of uniformity in temperature distribution on the surface of the cathode as well as with stress distribution for mechanical integrity of the gun. In case of rectangular cathode the uniformity has been improved from 7.7 % to 5.3 % and in case of trapezoidal cathode the uniformity has been improved from 9.9 % to 7.5 % by providing fins. Moreover, the fins were also helpful in reducing the heat transfer to the focusing grid. Experimental measurement shows that the uniformity of 5% has been achieved over 80 mm length. The drop in temperature (7.9 %) towards the holding section. is due to heat conduction to grid cup. The near uniform temperature of 2500 K over 110 mm length has been obtained with a band of 150 K which will give rise to desired emission in space charge limited region for the evaporation applications. One can achieve uniformity within 100 K by suitably modifying the fin structure. A linear beam of cross section 110 mm x 5 mm (approx) has been extracted axially.

CHAPTER 4

Transverse electron gun for electron beam based reactive evaporation system

Design of a 10 kV, 10 kW transverse electron gun has been presented in this work through systematic modeling and simulation approach. This work has been carried out through a) electron gun design and modeling, b) vapor transport modeling c) and validating the above models through experimentation. The reactive coating of desirable properties can be achieved in the pressure range of 10^{-1} Pa to 10^{-2} Pa. At this high pressure the electron gun does not operate reliably due to high voltage flashover. In order to overcome this problem the gun crucible system has been modified. The substrate chamber is isolated from gun chamber using a bifurcation plate. On this bifurcation plate, aperture is provided for beam emergence from the gun chamber to the substrate chamber. Using the differential pumping arrangement the gun chamber pressure is maintained at better than 5×10^{-3} Pa, whereas substrate chamber pressure can be between 10^{-1} Pa and 10^{-2} Pa. The dimension of the aperture has to be such that the beam will not hit the crucible body and the desired pressure differential is maintained. Also the beam should fall on the crucible pocket. Evaporant material is kept on the crucible pocket in order to carry out coating experiment. The gun has been fabricated and mounted in the gun chamber of dimension 800 mm x 800 mm x 250 mm. The substrate chamber of dimension, (800 mm x 800 mm x 750 mm), has been isolated from the gun chamber using a bifurcation plate on which rectangular aperture of appropriate size has been provided for the e-beam to emerge from the gun to the crucible pocket facing the substrate chamber. Since two guns have been used, two apertures have been provided. The gun chamber accommodates two 10 kV, 10 kW e-guns and the housing of two water cooled rotatable crucible, each with 4 pockets. The crucible indexing mechanism can rotate the crucible and bring a particular pocket for e-beam to hit that evaporant material. Individual pumping modules are connected to the gun chamber and the substrate chamber. Vacuum system for the gun chamber consists of a diffusion pump of capacity 12,000 lps backed by 175 m3/hr rotary pump. Vacuum system for the substrate chamber consists of turbo molecular pump of capacity 550 lps backed by 292 m3/hr rotary pump. The schematic of the system is shown in the Figure 4.1 and the internal of the gun-substrate chamber is shown in the Figure 4.2.

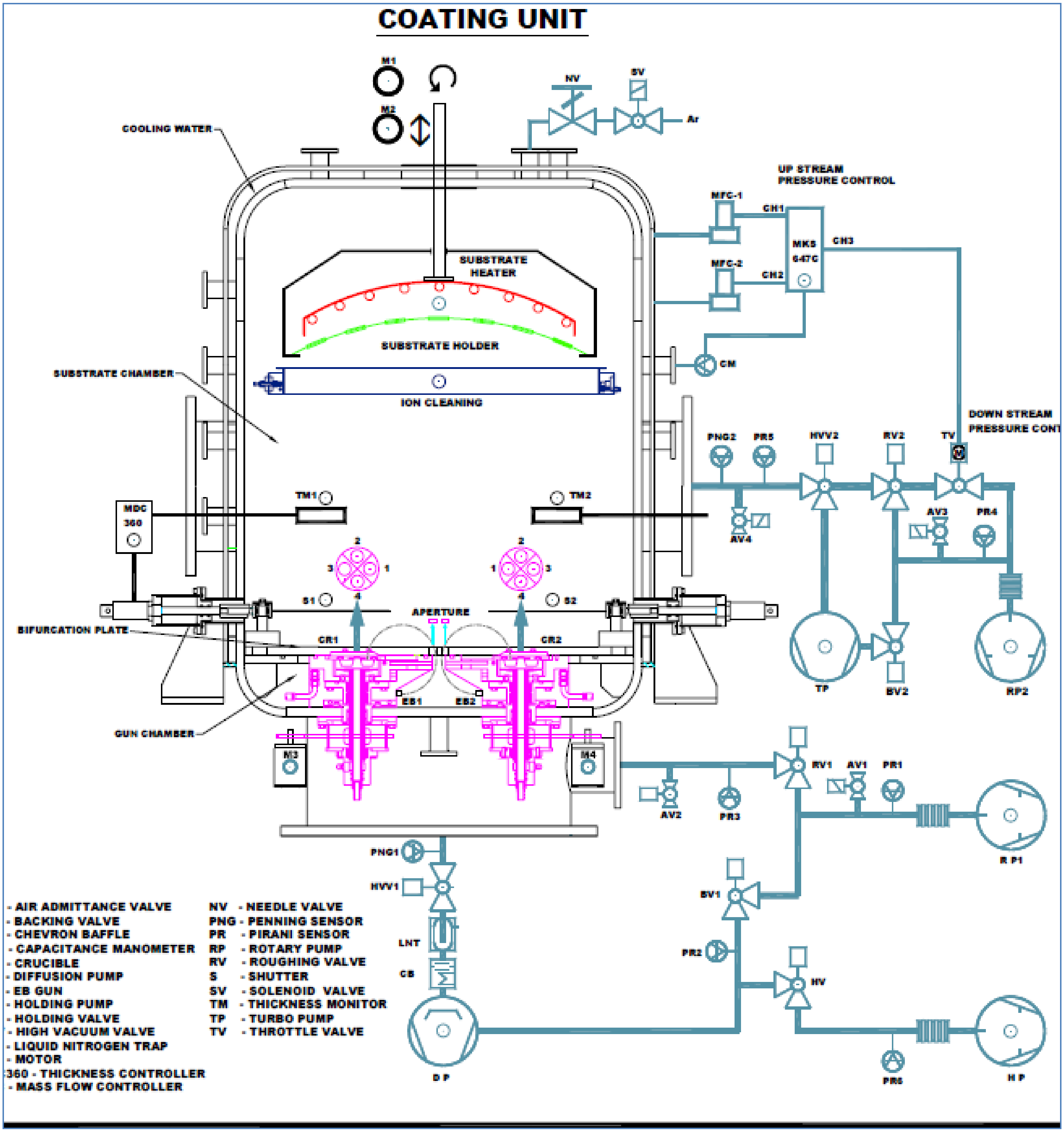

Fig 4.1. Schematic of coating system

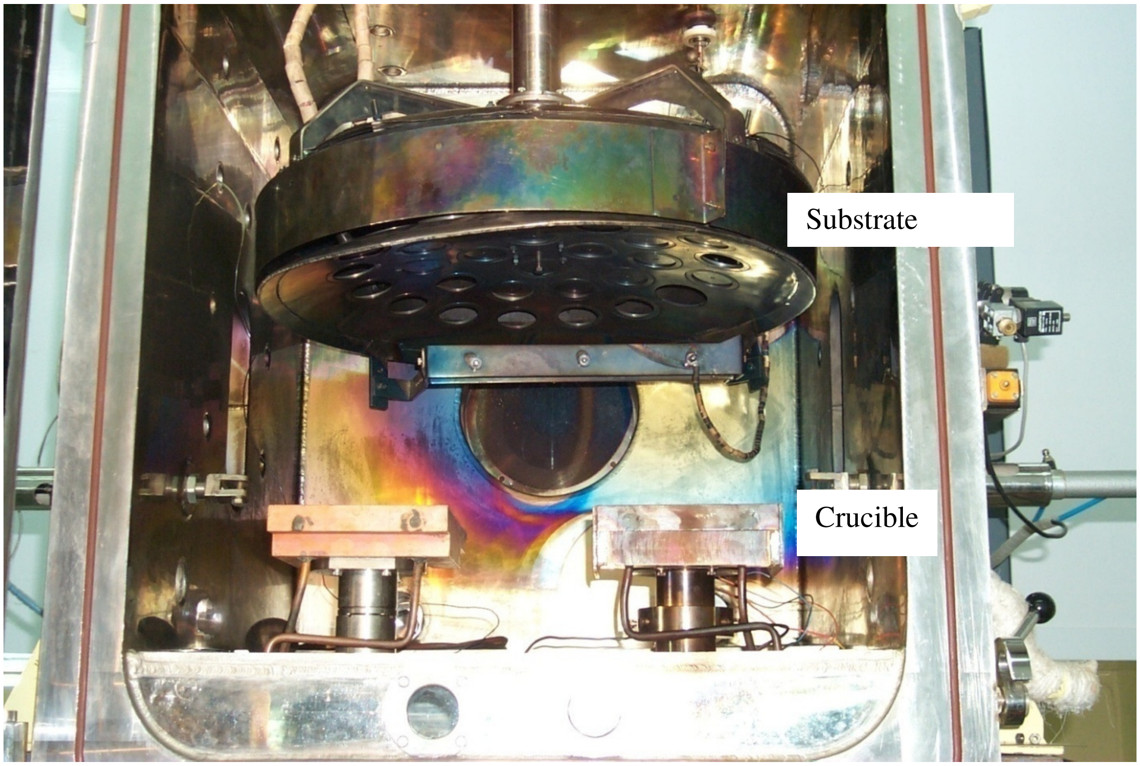

Fig 4.2. Internal of the gun-substrate chamber

4.1 Electron gun design

4.1.1 Electron gun design and trajectory analysis

The major considerations for the gun design were to attain required beam power, maintain the differential vacuum and at the same time make sure that the beam fall on the crucible pocket without hitting the crucible body. In order to attain these design criteria, the overall design of the system included the filament design, shaping of the electrodes and the magnetic circuit to suitably bend the beam onto the crucible. The filament wire of 0.78 mm diameter is made of tungsten material and has been shaped in a helical form with 6 turns each turn of 1.8 mm inner diameter. The pitch of the helix has been adjusted to make the length of 9 mm. The beam former which is non- axisymmetric in shape is kept at filament potential. The anode is also non-axisymmetric in shape and acceleration voltage of 10 kV between the filament and the anode of the electron gun provides the electrostatic field. The assembly of an electron gun is shown in the Fig. 4.3. In order to reduce the vapor coating on the high voltage insulator a shadow cap has been provided over the insulator thereby reducing flashover problems.

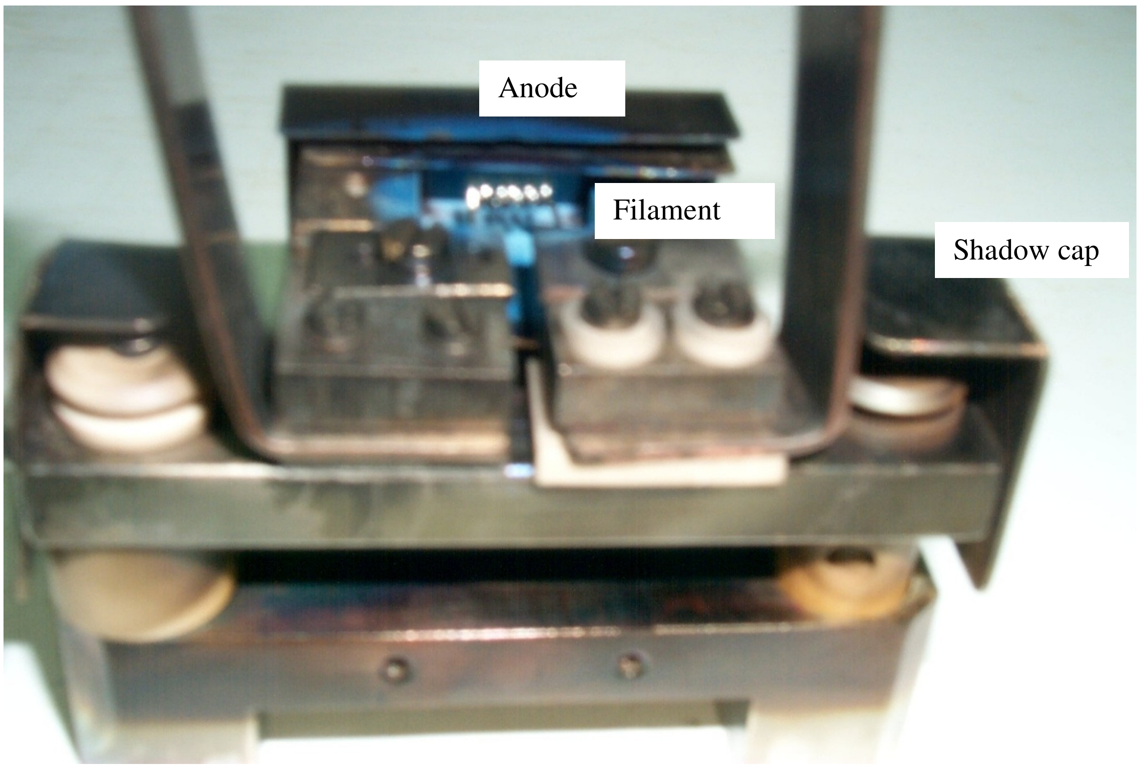

Fig 4.3 . Electron gun assembly

The magnetic field is available in the gun-crucible region using the pole extender from the permanent magnet, which is mounted at the rear side of the crucible to avoid loss of magnetism due to heating in the gun region and by using electromagnet around the beam emergence aperture. This magnetic field is non-uniform. The schematic of the magnetic circuit is shown in the Fig. 4.4. The crucible assembly which includes the magnetic circuit is shown in the Fig. 4.5. At the rear side of the crucible, two Nd-Fe-B permanent magnets have been supported by a mild steel bar in between the magnets. At the magnet pole, 1.4 kG magnetic field is available, this is reduced to nearly 60 G in the front section of the crucible by using pole extender. The pole extender is tapered in the gun region and also shunts have been used to further reduce the magnetic field. This magnetic field provides fixed bending of the beam.

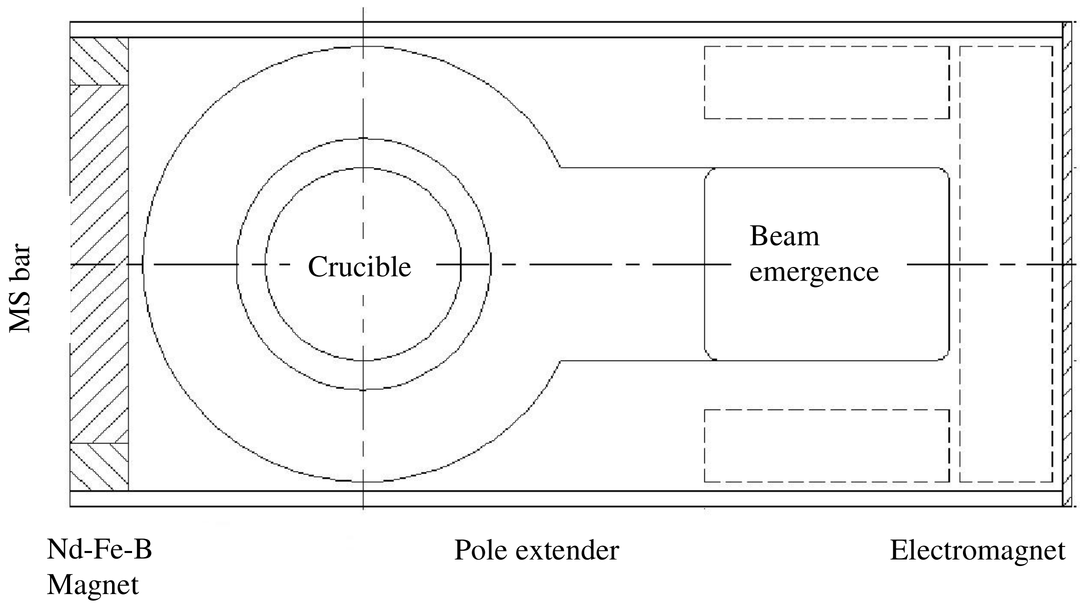

Fig 4.4. Schematic of magnetic circuit

Fig 4.5 Crucible assembly showing magnetic circuit

In order to maneuver the beam over the crucible, electromagnets have been designed and mounted around the beam emergence slot. In order to manuver the beam in the longitudinal direction, a solenoid of 500 turns with 0.88mm diameter enameled copper wire has been used. Using the solenoid, variable +/- 10 G magnetic field is available in the slot opening. This magnetic field is superimposed with the fixed magnetic field by permanent magnet. In order to maneuver the beam in the lateral direction, two half solenoids each with 250 turns have been mounted in perpendicular direction to the longitudinal solenoid thereby forming a 'C' shape around the beam emergence slot. The magnetic field at the filament tip is 31 G and varies to 51 G at the beam emergence slot which is about 80 mm above the filament tip. The beam trajectory simulation has been carried out using an electron optics software EGUN© by SLAC using rectangular coordinates. POLYGON© translates the electrode boundary conditions alongwith designated potentials, magnetic field data and other input parameters into a data file compatible with EGN2W of EGUN© code. This data file provides the input to EGN2W. EGN2W in turn computes the equipotential lines and the electron trajectories.

4.1.2 Results

First the trajectory analysis of the electron gun has been carried out without magnetic field using EGUN, which is shown in the Fig. 4.6 The scale is magnified 8 times in both the X - axis and the Y - axis. The cross over point of the beam is in between the anode and the former. Using non-uniform magnetic field, the trajectory simulation is shown in the Fig. 4.7. The magnetic field values in Gauss are shown in the right hand side along the Y-axis of the figure. The X-axis, is 11 times magnified and in mm. The left hand Y-axis showing the upward traverse of the electron beam is 11 times magnified and in mm. The bifurcation plate is kept about 80 mm above the filament tip level which is at the 900 level (in the Fig. 4.7) in the Y-axis. The beam emergence slot (90^o position) and the crucible (270^o position) are both at

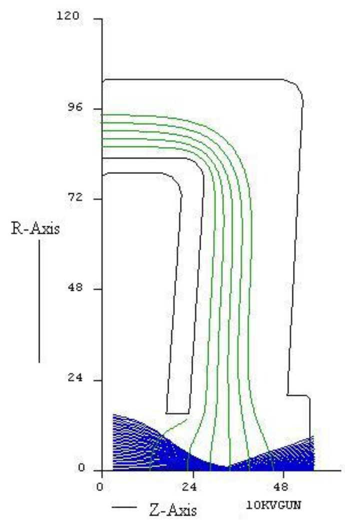

Fig. 4.6 Electron beam trajectory using electrostatic field

this level. From the trajectory in the Fig. 4.7 it can be seen that the beam widening of 14 mm takes place at the beam emergence and on the crucible the beam diameter is 10 mm. The center to center distance between the beam emergence and the crucible is 112 mm. This has been validated through the experiment using a dummy stainless steel plate on the bifurcation plate. In Fig. 4.8, the experiment shows that the beam widening is 17 mm at the beam emergence and the beam diameter on the crucible is 10 mm. The center to center distance between the beam emergence and the crucible is 108.5 mm. A puncture experiment has been conducted at low beam power which is shown in the Fig. 4.9. Here the effect of gun mounting at various heights has been shown by the two beam spots. When the gun is mounted closer to the bifurcation plate, the beam radius decreases due to larger local magnetic field and the center to center distance between the beam emergence and the crucible reduces. Based on the beam trajectory analysis, the beam emergence aperture of dimension 15mm x 18mm for each crucible has been provided on the bifurcation plate for differential pumping operation between the gun chamber and the substrate chamber.

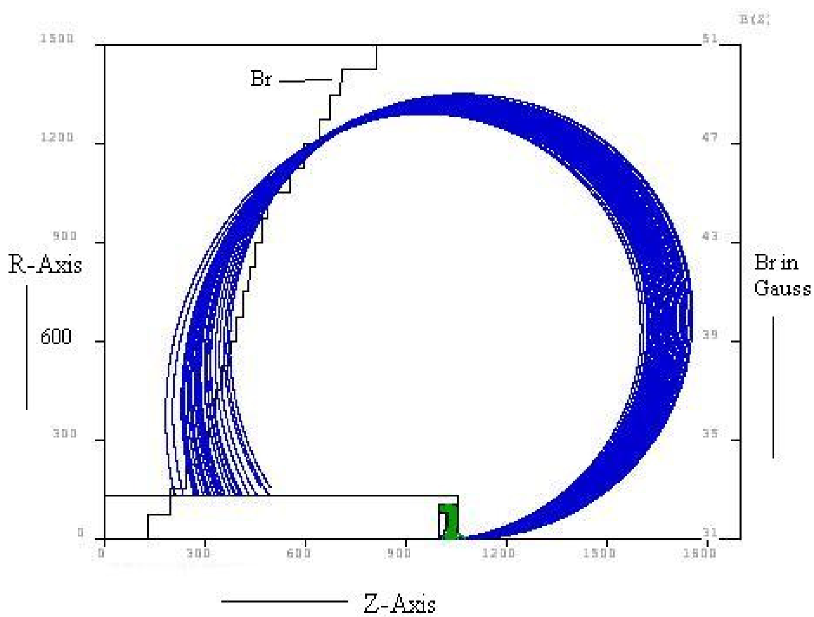

Fig. 4.7 Electron beam trajectory using magnetic field

tungsten block up to 10 kW power. Metal coating of titanium has been done at 2 kW power. Reactive coating of alumina [60] has been also performed.

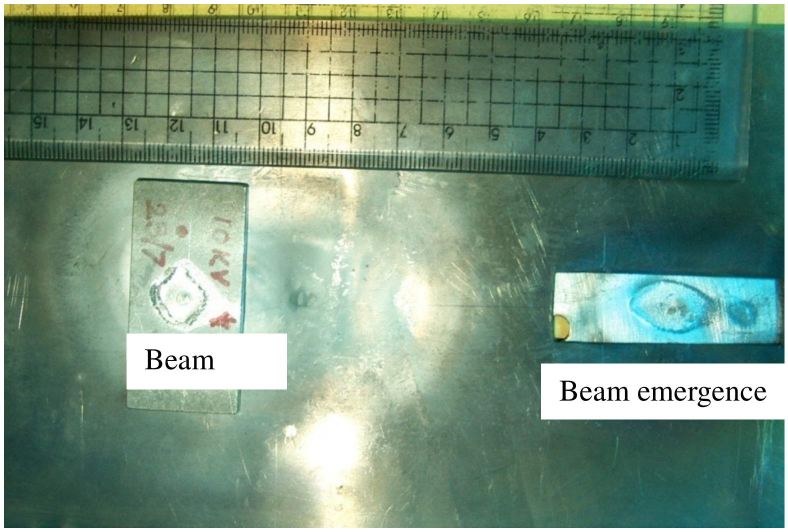

Fig 4.8. Experimental beam on the stainless steel plate

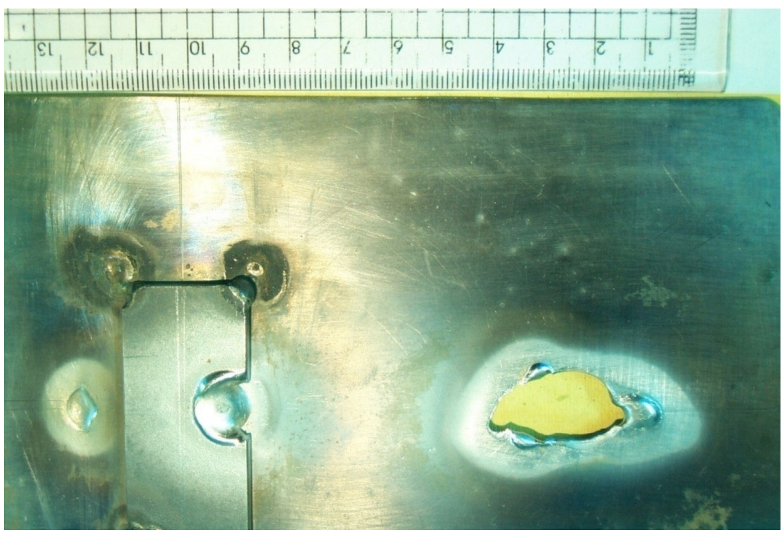

Fig 4.9. Puncture experiment of electron beam

4.2 Modeling of vapor transport of electron beam coating system

The modeling of vapor transport of an electron beam evaporation based coating system has been carried out in this work. Computational fluid dynamics (CFD) modeling has been tailored to analyze the evaporation and deposition of titanium material. Based on the physical model, the model relates the output power of the electron gun and the temperature profile on the evaporant surface. The simulated vapor distribution helps in predicting the coating thickness. On the evaporant surface, the saturated vapor pressure of Titanium (0.37 Pa @1660°C) (as a representative material) prevails. Following the vapor pressure contours as reported in [23], the Knudsen number is found to be less than 0.1 in the computational domain. Therefore, CFD modeling can be applied to obtain vapor flux distribution.

4.2.1 CFD modeling for vapor transport

Electron beam evaporation from water cooled crucibles is highly lossy [23]. The value of heat transfer coefficient for the bottom surface of the titanium block was deterimed by measuring the temperature rise of the water which cools the crucible. The problem of computing evaporation and subsequent transport of vapor in the computational volume is divided into two parts. In the first part the temperature distribution in the crucible is computed by solving the energy conservation equation on the evaporant material. Evaporant material is cylindrical in shape of 3 cm diameter. Using the temperature distribution at the evaporant material surface, rate of evaporation is calculated using Langmuir equation. This is done in a coupled manner to incorporate the effect of heat of vaporization on the surface temperature distribution. Only the energy conservation equation is solved on the evaporant surface as in (4.1).

$$\nabla \cdot \left(\frac{k}{\rho c} \nabla T \right) = 0 \qquad (4.1)$$

where, k is the conductivity, ρ is the density and c_p is the heat capacity.

At the electron beam- crucible interface, equation (4.2) has been used to calculate net heat flux into the evaporant material.

$$q_{net} = q_{ebeam} - q_{rad} - q_{vaporization} \qquad (4.2)$$

Where, q_{ebeam} = ebeam power * efficiency and

ebeam power = V x I, V = Acceleration voltage and I = Beam current

$$q_{rad} = 4\pi\varepsilon T^{4}$$

$$q_{vaporization} = R_{vaporization} * Q_{vaporization}$$

Here, $Q_{vaporization}$, $R_{vaporization}$ are enthalpies and rate of vaporization respectively.

Rate of vaporization is calculated using the Langmuir equation (4.3), namely,

$$a_v = \alpha \text{ x } 4.4 \text{ x } 10^{-4} \text{ x } p_s \text{ x } (M_D/T_v) \quad (4.3)$$

where, a_v is specific evaporation rate measured in g cm^{-2} s^{-1}, α is the evaporation coefficient which becomes 1 for idealized evaporation, and M_D the molecular weight of an evaporant, p_s is the saturated vapor pressure at the temperature T_v.

After computing the temperature distribution on the evaporant material surface and evaporation rate, the flow of vapor in the chamber is calculated. Values of temperature and evaporation rate at the evaporant surface are used as mass flow inlet conditions of the fluid domain. Flow is assumed to be laminar. In the fluid domain titanium vapor is treated as an incompressible ideal gas.

Following equations have been solved in the fluid domain.

Mass conservation equation

$$\text{div}\,(\rho\vec{u}) = 0 \quad (4.4)$$

x-momentum conservation equation

$$\nabla.(\rho\vec{u}\vec{u}) = \frac{\partial p}{\partial x} - \nabla.(\mu\nabla\vec{u}) \quad (4.5)$$

y-momentum conservation equation

$$\nabla.(\rho\vec{u}\vec{v}) = \frac{\partial p}{\partial x} - \nabla.(\mu\nabla\vec{v}) \quad (4.6)$$

z-momentum conservation equation

$$\nabla.(\rho\vec{u}\vec{w}) = \frac{\partial p}{\partial x} - \nabla.(\mu\nabla\vec{w}) \quad (4.7)$$

Energy conservation equation

$$\frac{\partial(\rho\vec{u}h)}{\partial x} = p\,\nabla.\vec{u} - \frac{\partial(k\frac{\partial}{\partial x}h)}{\partial x} \quad (4.8)$$

Where,

p is the pressure,

ρ is the density, $\vec{u}$ is the x component of the velocity

$\vec{v}$ is the y component of the velocity,

$\vec{w}$ is the z component of the velocity, k is the conductivity

h is enthalpy, and μ is the kinematic viscosity.

4.2.2 Results

The result of the vapor transport has been reported with the help of CFD modeling. The CFD has been applied upto 4 kW power and the results have been obtained. The experiments have been carried out at about 2 kW, as the coating operation of titanium has been carried out at this power. Fig. 4.10 shows the temperature profile on the crucible surface at various powers. It shows that the temperature distribution is not uniform. This nonuniformity is a result of heat losses at the crucible boundary. The rate of rise in peak temperature with electron beam power shows a decline indicating that at higher electron beam power, heat losses due to evaporation and radiation have a significant contribution. In Fig. 4.11, the evaporation rate from the crucible at different powers is presented. Since the temperature is nonuniform, the evaporation rate is also nonuniform in nature. Fig. 4.12 shows the temperature distribution inside the crucible for different electron beam power. Fig. 4.13 shows the computed distribution of temperature, velocity magnitude and velocity vectors in the fluid domain. The presence of a high pressure gradient results in a high vapor flow velocity. As the distance between the substrate and the crucible is much larger than the dimension of the evaporation zone, it is treated as the point source in order to compute the deposition rate on the substrate. The fraction of vapors deposited was calculated using the value of solid angle the substrate makes on the vapor source. Table 4.1 shows the estimated coating thickness computed using

CFD methods for a duration of 1 hour. Experiments have been conducted for titanium coating at 8 kV, 250 mA for 1 hour. The substrate is 30 mm in diameter and coating thickness of 5.2 micron could be achieved which is in close agreement with the estimated 7.2 micron using CFD.

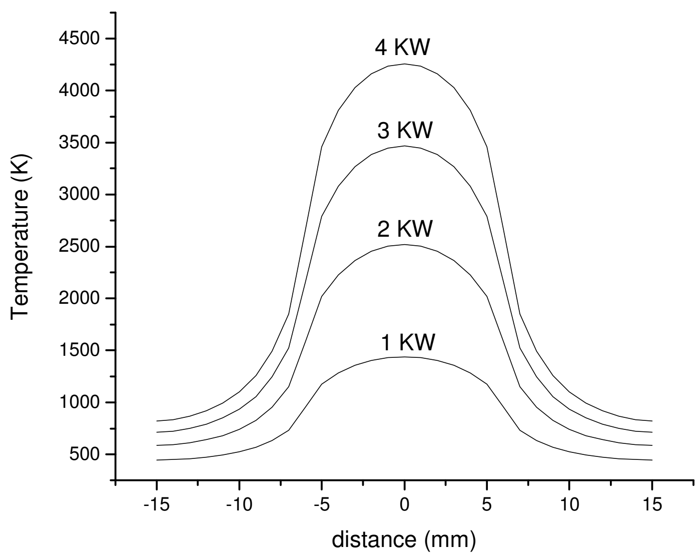

Fig. 4.10 Temperature profile at the crucible top face for different electron beam power

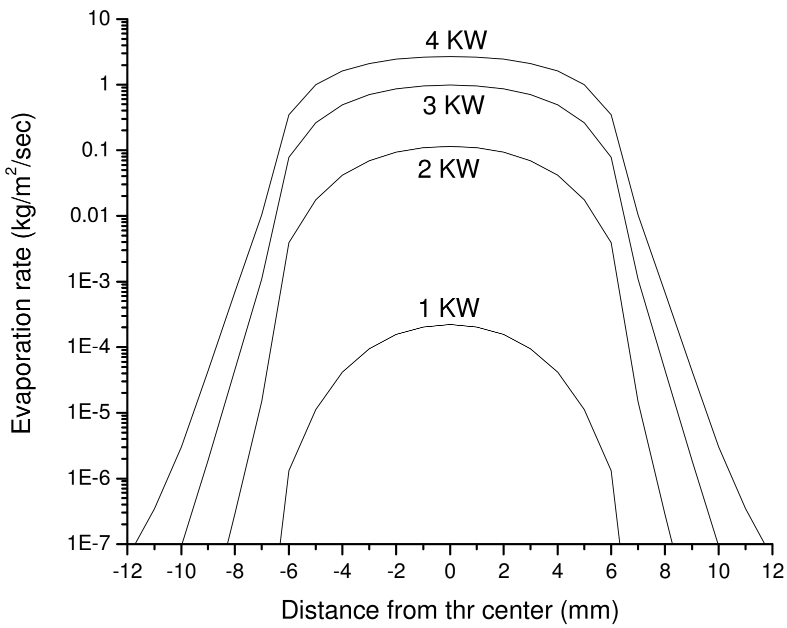

Fig. 4.11 Evaporation rate profile for different electron beam power

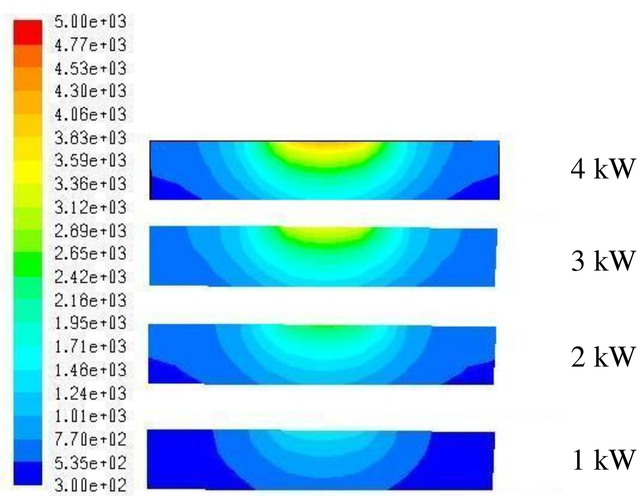

Fig. 4.12 Temperature distribution inside the crucible for different electron beam power

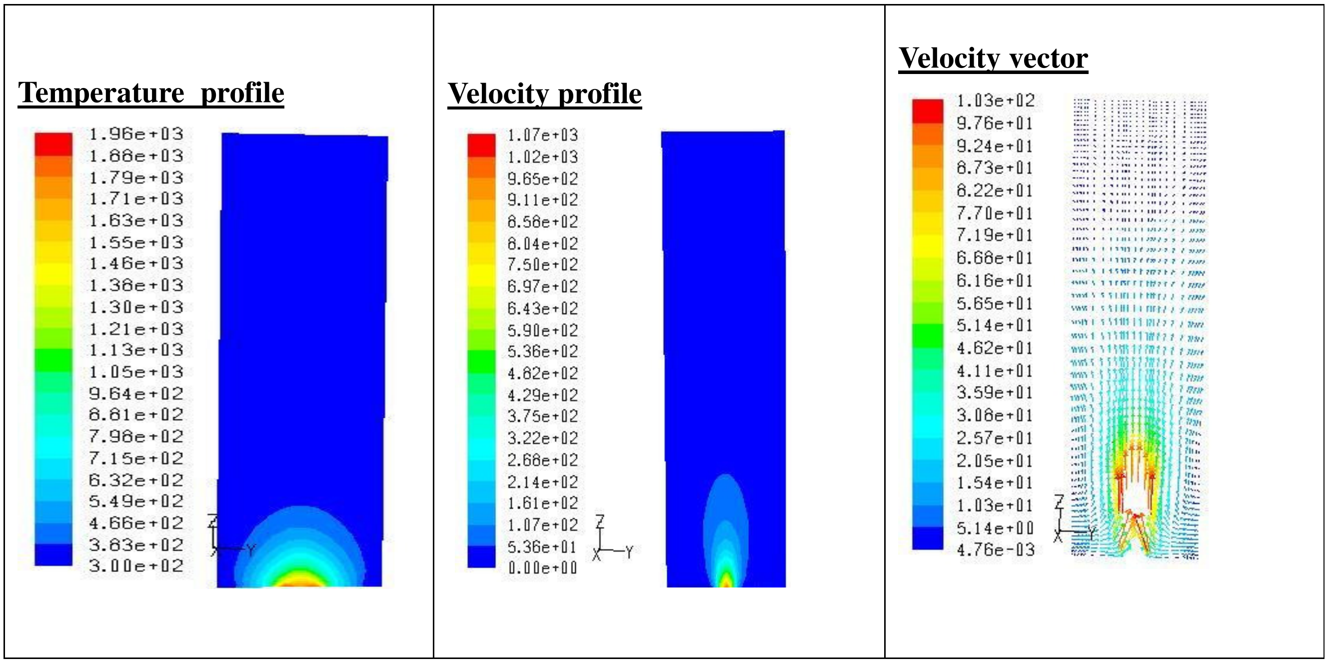

Fig. 4.13 CFD results for 2 kW power

Table 4.1 Estimated coating thickness of titanium using CFD

Ebeam Power (Kw)	Net evaporation rate (Kg/s)	Net deposition rate (Kg/s)	Coating thickness (micron)
1	$2.5*10^{-15}$	$1.875*10^{-18}$	$3.97 *10^{-9}$
2	$8.5*10^{-6}$	$6.375*10^{-9}$	7.21
3	$2.07*10^{-5}$	$3.7*10^{-10}$	17.558

4.2.3 CFD modeling for reactive coating

For metallic coating the vapor transport mechanism is not influenced by any external inlet. Whereas, for any reactive coating, the vapor transport is influenced by external inlet. As a representative case we have considered the coating of yttrium oxide.

As the Yttrium-oxide (Y_2O_3) is heated above 2410^0C, it transforms in vapor phase. It is a compound of yttrium and oxygen, so at a high temperature chemical reactions take place. The products will be YO, O and Yttrium. Yttrium metal reacts readily to form yttrium oxide

(Y_2O_3) in the presence of oxygen. Therefore external oxygen is bled into the system. The possible reactions [24] are as follows:

$$Y_2O_{3(s)} \xrightarrow{above\ 2073\ K} 2YO_{(g)} + O_{(g)} .$$

$$YO_{(g)} \xrightarrow{above\ 2373\ K} Y_{(g)} + O_{(g)}.$$

$$2Y + \frac{3}{2}O_2 \rightarrow Y_2O_3$$

$$4Y + 3\,O_2 \rightarrow Y_2O_3$$

These reaction equations clearly show that at a high temperature yttrium-oxide is dissociated, and again yttrium-oxide is formed at a low temperature near the substrate with the help of added oxygen. CFD calculates the rate of reactions, products of reaction and mass fraction by using the Arrhenius rate equation. Laminar finite rate turbulence chemistry model is used to calculate the rate of reaction. It computes only the Arrhenius rate and neglects turbulence-chemistry interaction. Pre-exponential factor and activation energy of each reaction data is used for implementation in CFD.

4.2.4 Discussion

An electron gun has been designed for a differentially pumped reactive evaporation system. The beam emergence aperture of dimension 15mm x 18mm for each crucible could be designed and fabricated on the bifurcation plate for differential pumping operation between the gun chamber and the substrate chamber. The gun operates reliably when substrate chamber pressure is at the range 10^{-1} Pa to 10^{-2} Pa. All aspects of design of an electron gun for a differentially pumped reactive evaporation system has been detailed in this work. Since all the parts are integrated for a specific end use, modifications to suit special requirements are within our control and can be exploited as and when necessary.

Using CFD modeling, the vapor transport analysis on titanium has been validated with the experimental result. Experiments have been conducted for titanium coating at 8 kV, 250 mA for 1 hour. The substrate is 30 mm in diameter and coating thickness of 5.2 micron could be achieved which is in close agreement with the estimated 7.2 micron using CFD.

CHAPTER 5

Attenuation of electron gun generated surges

Vacuum breakdown is a very commonly occurring phenomenon during the operation of any electron gun. This not only spoils the job, it also causes lot of damage to the electronics of the system. Breakdown can occur due to various reasons such as, 1) material chosen for the gun electrodes, 2) inter-electrode distance, 3) outgassing of the material at high temperature, 4) degassing from molten metal. Breakdown especially occurs when the pressure inside the vacuum chamber increases. More specifically, as the material in the crucible evaporates, positive metal vapor ions may be generated, which may go back to the emitter along the same path taken by the electron beam causing erosion in the emitter. All these factors sometimes make it difficult to ascertain the reliable high voltage performance of the electron gun. To overcome the breakdown problem, one tries to maintain the electric field as uniform as possible. Safe limit is followed while choosing the inter-electrode gap and also the creepage path of the insulator. Electrode profiles are modified to maintain the electric field at acceptable level. After following all the necessary high voltage related guidelines, the breakdown reduces considerably. But the risk of breakdown and the resulting effect still persists. So additional measures need to be provided to control the breakdown problem.

The approach in this thesis is to attenuate the breakdown current near the gun so that it does not propagate to the power source to cause any detrimental effect. In this paper ferrite beads have been used to suppress the high frequency content and also to reduce the amplitude of the breakdown signal. Though the use of ferrite beads in transient suppression is not new, the main contribution of the work reported is (a) to identify, using spectral analysis, certain characteristics of a breakdown signal, (b) using this to compute the value of L (inductance) required to filter out high frequency components of the signal, thereby leading to the determination of the number of ferrite beads required and (c) experimentally verifying that the right choice of the number of ferrite beads does indeed smoothens the breakdown signal. An induction coil has been designed to monitor the breakdown signal. A detailed analysis of the breakdown signal has been presented in this thesis.

5.1 Design of sensor to measure the breakdown signal

An induction coil sensor has been designed to measure the gun breakdown current. It is a 10 kV, 10 kW gun and the sensor has been accordingly designed. It has been reported in [33] that an induction coil sensor is the simplest sensor which provides excellent sensitivity and bandwidth. It can measure the high frequency current in a nonintrusive way and additionally provides an excellent galvanic isolation from the measured circuit. The current carrying conductor produces magnetic field and the magnetic field is orthogonal to the current. When the sensing coil is placed perpendicular to the conductor, maximum flux linkages can be achieved. Based on Faraday's law (5.1) the sensor coil is designed and the output of the coil can be suitably modified based on the measurement requirement.

$$V = -N \frac{d\phi}{dt} \qquad (5.1)$$

where, V is the output voltage of sensor coil, N is the number of turns in the coil and $\frac{d\phi}{dt}$ is the rate of change of flux linkage.

The evaporation gun is a diode type for which the filament is floated at -10 kV and the anode is grounded. The electrons emitted from the filament are accelerated to the grounded crucible. The gun is energized through two filament terminals that are connected to two cables using high voltage feedthrough. These cables are connected to the transformer-rectifier system. The breakdown in the gun is monitored close to the gun just after the feedthrough termination. It is calculated that a coil of 100 turns, 27 mm length and 27 mm mean diameter can provide 0.196 V when 1 A transient current passes through the conductor of 10 mm diameter.

Inductance of this coil has been calculated based on Wheelers formula [34] as stated in the (5.2).

$$L\,(uH) = \frac{31.6 * r_1^{\,2} * n^2}{(6 * r_1 + 9 * l + 10 * (r_2 - r_1))} \qquad (5.2)$$

where , r_1 = inside coil radius in meter

r_2 = outside coil radius in meter

n = no. of turns of the coil

l = length of the coil in meter

The computed value of the inductance is 166.8 µH using (5.2). The self capacitance value has been estimated using the empirical relation by Medhurst [35] as in (5.3).

$$C = \left(\frac{4\varepsilon_0}{\pi}\right) * l * \left[1 + 0.7096\left(\frac{D}{l}\right) + 2.3950\left(\frac{D}{l}\right)^{1.5}\right] Farad \qquad (5.3)$$

Where, D = Average. Diameter of the wire in meter

l = Solenoid length in meter, ε_0 *is in Farad/meter*

The calculated capacitance value is 12.5 pF. The bandwidth of the sensor is mainly determined by the first resonant frequency f $= \frac{1}{2\pi\sqrt{LC}}$. Using the calculated parameters the resonant frequency is identified to be 3.5 MHz. The bandwidth can be improved based on the sensor coil parameters. Fig. 5.1 shows a block diagram of the system layout.

Fig. 5.2 shows the experimental setup, showing the location of sensor coil and ferrite beads on the incoming cable to the gun of the evaporation system.

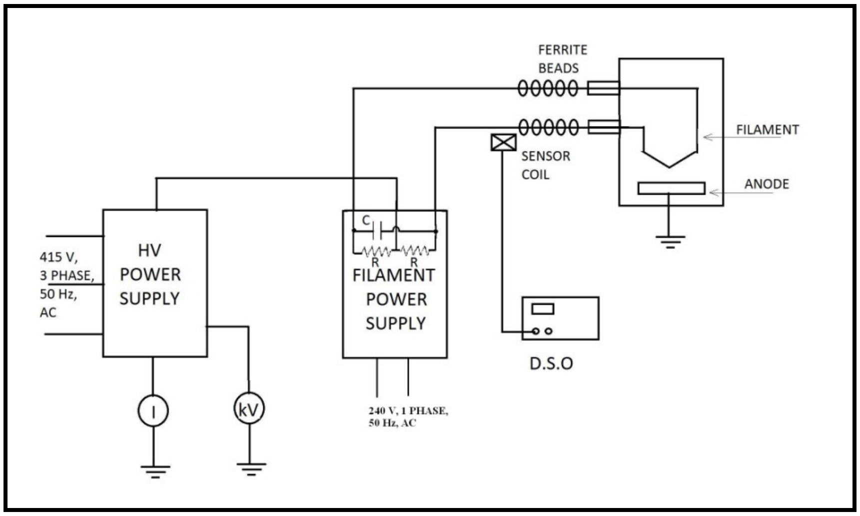

Fig. 5.1 Block diagram of the system layout

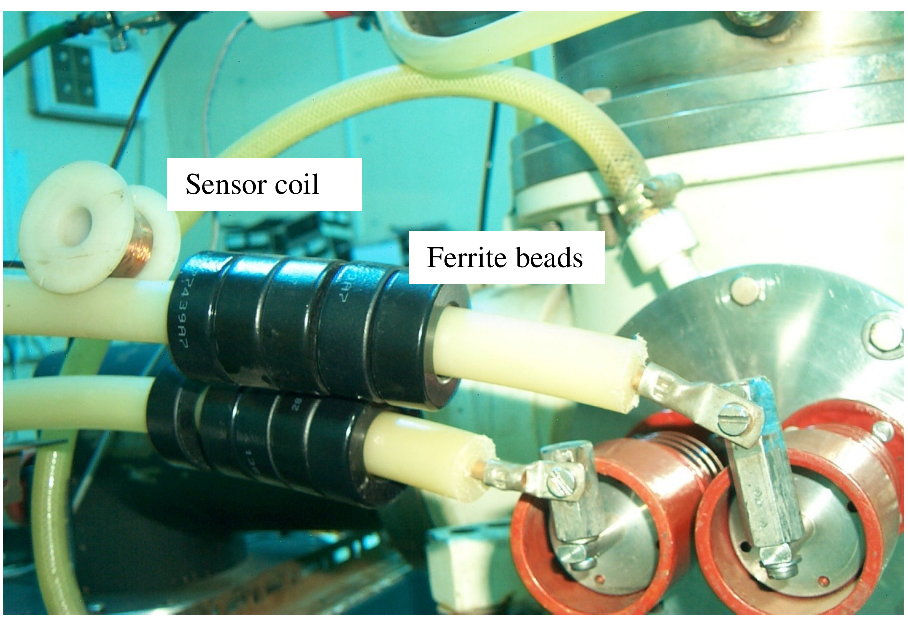

Fig 5.2 Breakdown signal monitoring setup

Using the sensor coil the gun breakdown signal is captured using a 200 MHz digital storage oscilloscope, Model TDS2024B, TEKTRONIX make. The breakdown signal is analyzed using Fast Fourier transform (FFT) to find the spectral or frequency content of the signal. This spectral analysis provides all the necessary information related to the breakdown signal, that needs to be attenuated before it propagates to the power source.

5.2 Use of ferrite bead for transient suppression

The ferrite beads are used as passive low pass filter. It passes DC fully, but rejects best around the desired frequency band. It is an inductor with very low Q factor and by design it filters out the high frequency content. It acts as high resistance to high frequency signals and low resistance to low frequency signals. This property of ferrite bead has been exploited to suppress the high frequency content of the signal. Manganese zinc ferrite offers high permeability for transient suppression in the frequency range 10 kHz to 50 MHz [36]. When selecting a ferrite bead inductor, it is necessary to consider the impedance in the transient frequency band of interest. The impedance characteristic varies depending on the material and the structure. The breakdown during reactive evaporation has likely hood of more high frequency content, therefore breakdown signal has been monitored on yttria evaporant and one representative signal is shown in the Fig. 5.3. The FFT of this signal in Fig.5.4 shows that the dominant frequency is in the range of 10-14 MHz in the higher frequency side. To suppress the transient in the range of 0.5 MHz to 20 MHz the minimum inductive impedance required is 1 KΩ [36]. The impedance response [36] is shown in the Fig. 5.5.

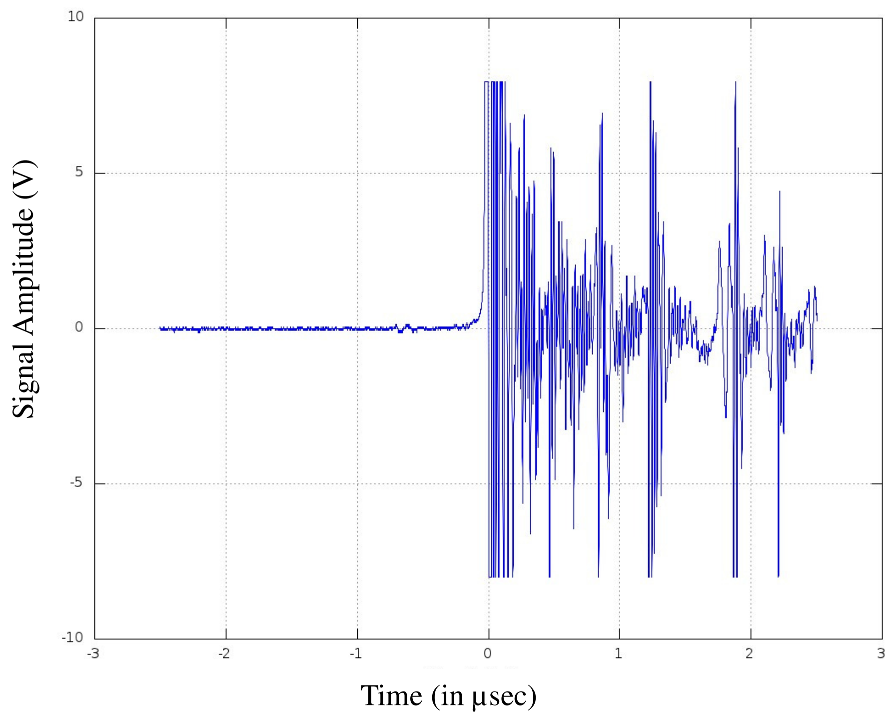

Fig 5.3: A Sample breakdown signal using yttria as evaporant material

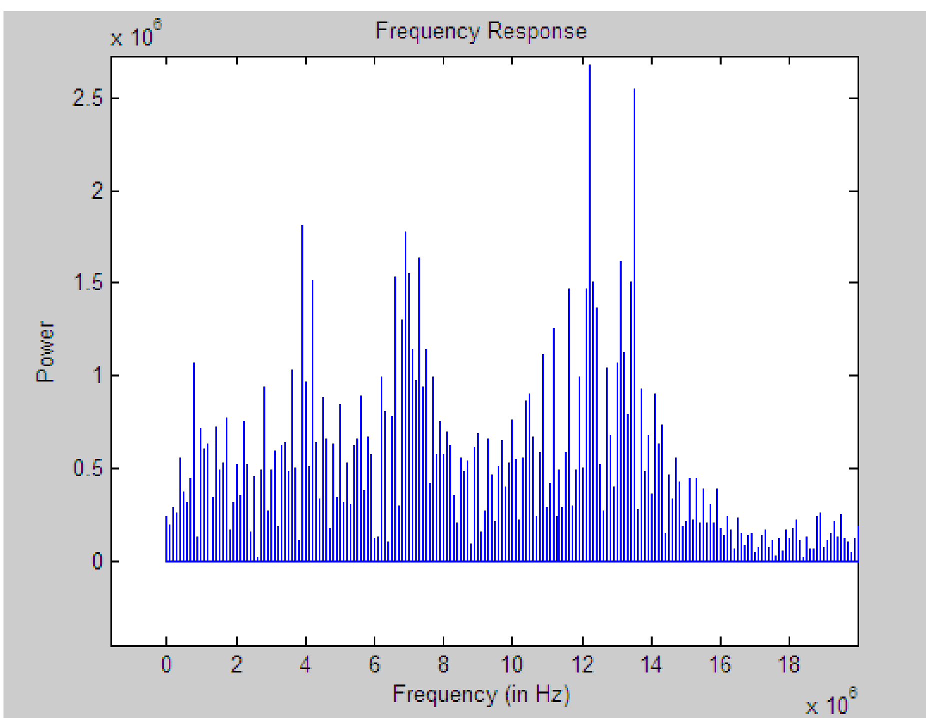

Fig 5.4: Spectral analysis of breakdown signal shown in Fig. 5.3.

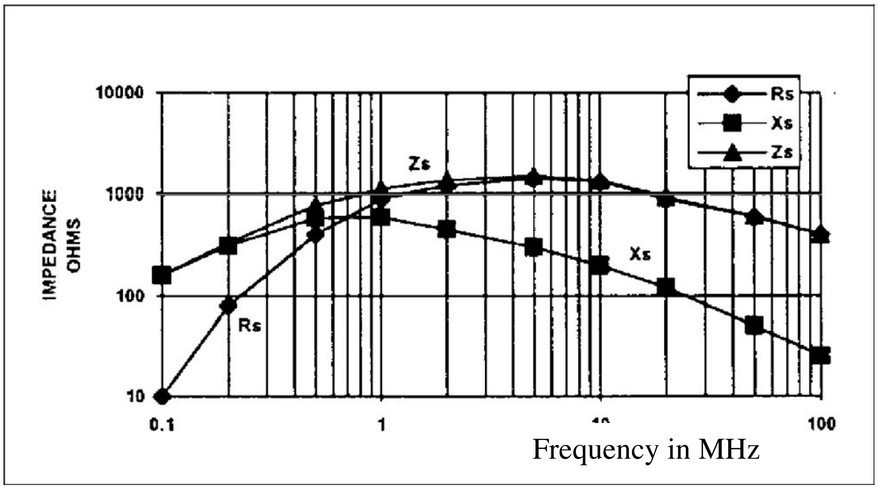

Fig 5.5: Impedance response of the ferrite

Hence the minimum inductance (L_{min}) required is calculated to be about 15.9 μH using (5.4).

$$L_{min} = 1000\ \Omega / (2\ \pi\ 10000000\ \text{Hz}) \qquad (5.4)$$

Kool Mμ type powder core [37] offers superior performance than gapped ferrite core. Therefore the selected bead is a Kool Mμ type powder core with outer diameter 46.7 mm and inner diameter 18 mm, Part No. 55438A2. The inductance factor (A_L) for this core is 135. Therefore 10 turns of the bead provide inductance of 13.5 μH from (5.5), which closely matches the required minimum inductance.

$$N = 1000(L/A_L)^{1/2} \qquad (5.5)$$

where, N = Number of turns, namely, 10 beads in our case

L = Inductance (mH)

A_L = Inductance factor in mH/1000 turns

The high voltage cable connected to the evaporation system has outer diameter of 24 mm and the ferrite beads are inserted on it. Ten such beads used in the experiment are shown in the Fig. 5.2.

5.3 Experimental Results

The breakdown studies have been carried out in an indigenously developed 10 kV, 10 kW, 270 deg bent-beam electron gun based evaporation system. The vacuum system consists of a diffusion pump backed by a rotary pump and it provides a base pressure of 1x 10^{-3} Pa.

Experiments have been conducted using aluminum metal as evaporant material in the evaporation system. The transient signal is measured using the sensor coil and 2 GS/s, 200 MHz storage oscilloscope. Initially breakdown signal is measured without inserting the ferrite beads. Subsequently breakdown signal is measured after inserting the ferrite beads. Fig. 5.6 shows representative signals with and without ferrite bead using aluminum evaporant. The coating experiment of aluminum has been carried out at 8kV, 150 mA. Clearly the rise time and fall time increases and the settling time reduces with the use of ferrite bead. The breakdown signals have been analyzed using Fast Fourier Transform (FFT). FFT plot of the breakdown signal with and without ferrite bead is shown in the Fig. 5.7. It shows that the high frequency components upto 6 MHz is present in the signal with ferrite bead, which reduces drastically with ferrite bead. Also there is power spectrum reduction by a factor of nearly nine. In an another set of experiment yttria has been used as evaporant. The yttria coating is carried out as reactive evaporation where external oxygen is bleeded into the system during coating. Experiment of yttria has been carried out at 8 kV, 250 mA. The oxygen bleeding was done at 0.5 Sccm and the system pressure rose to 5x 10^{-3} Pa. At this operating condition, the Fig. 5.8 shows breakdown signals of yttria with and without ferrite bead. FFT plot of the breakdown signal with and without ferrite bead is shown in the Fig. 5.9. It shows that the high frequency components are present in the entire spectrum without ferrite bead which reduce drastically with ferrite bead and the power spectrum reduction is found to be approximately 9. In the Fig. 5.10, the breakdown signal has been monitored at 150 mA, 250 mA and 400 mA with acceleration voltage at 8 kV. The power spectrum in the Fig. 5.11 shows that the higher beam current does not saturate the ferrite bead causing reduction in the spectrum.

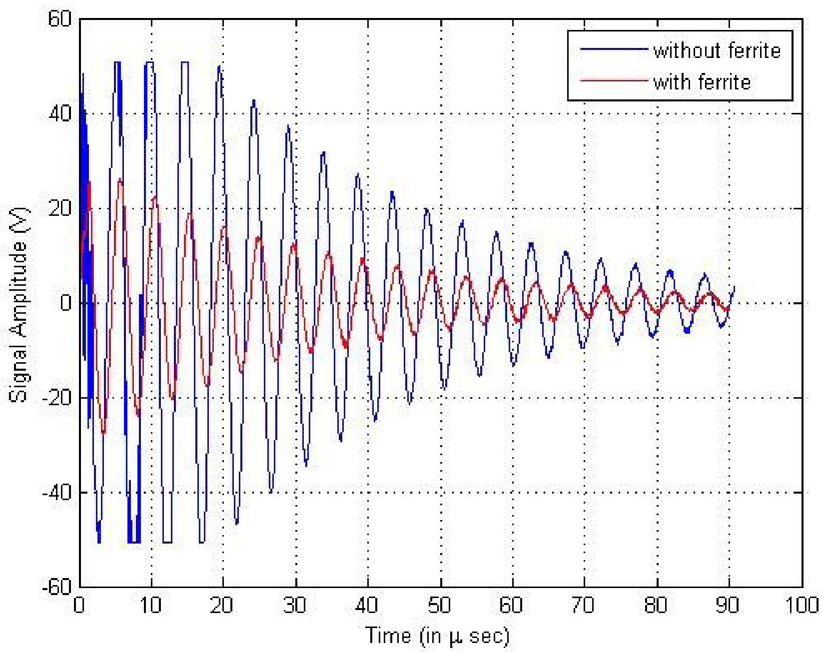

Fig 5.6: A sample breakdown signal using aluminum evaporant with ferrite (red) and without ferrite (blue)

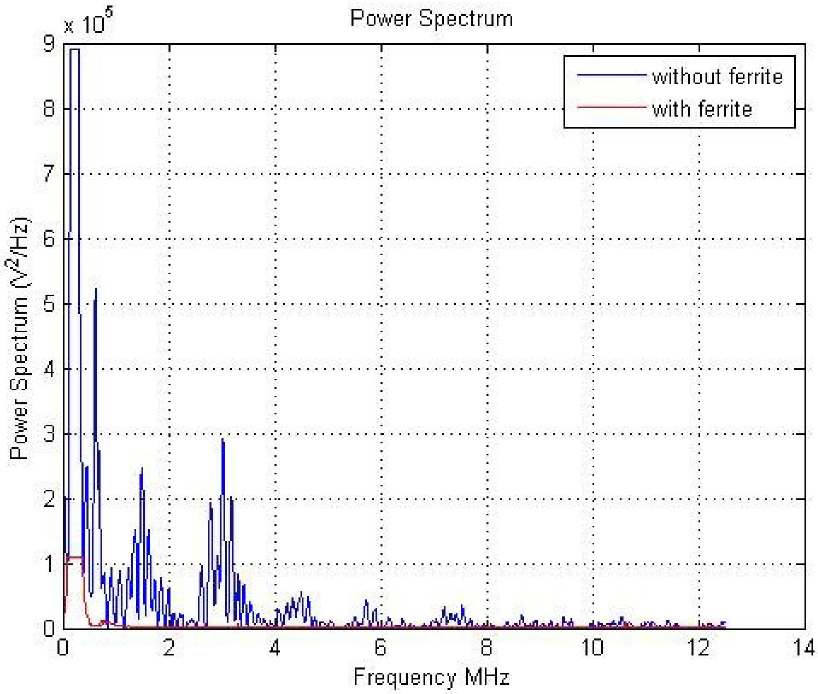

Fig 5.7. Power spectrum of the aluminum evaporant

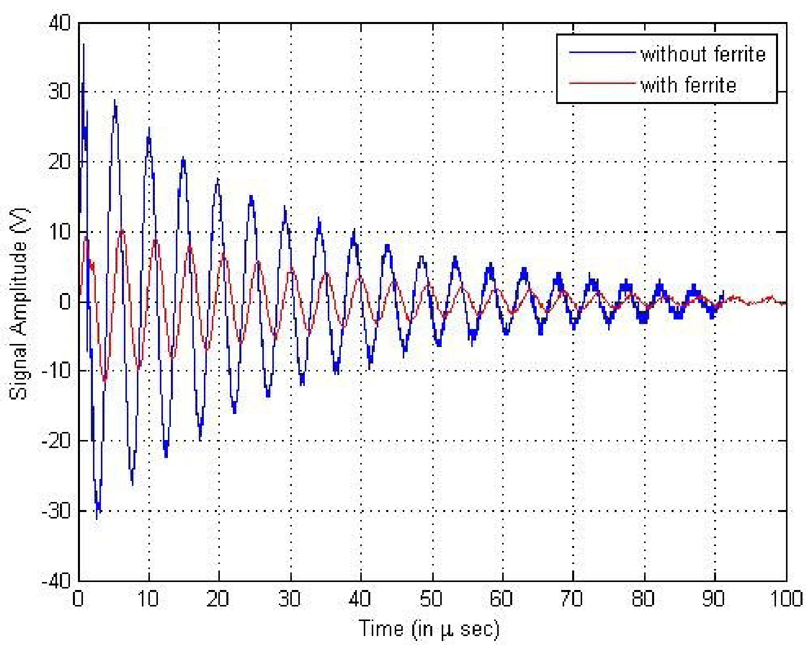

Fig 5.8: A sample breakdown signal using yttria evaporant with ferrite (red) and without ferrite (blue)

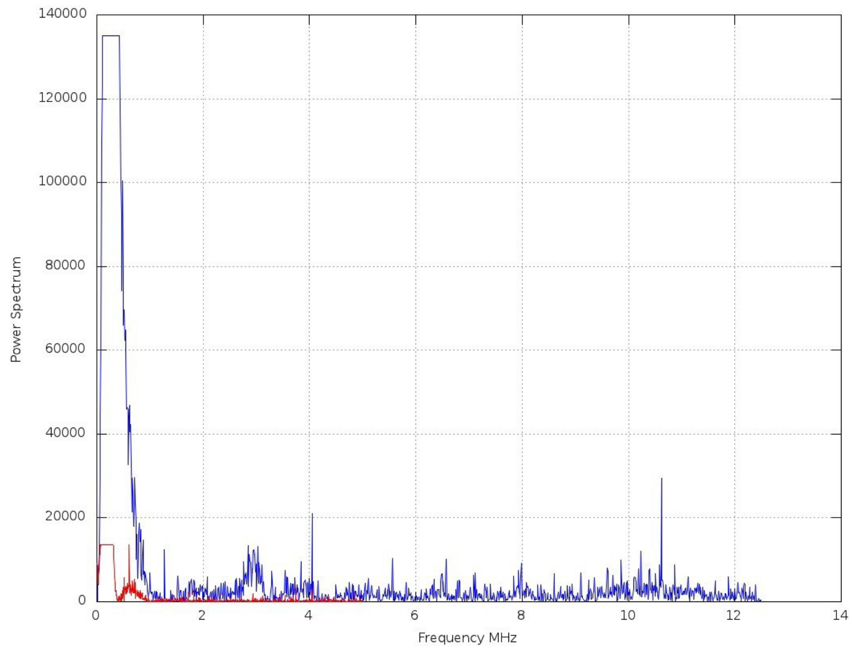

Fig. 5.9 Power spectrum of yttria evaporant

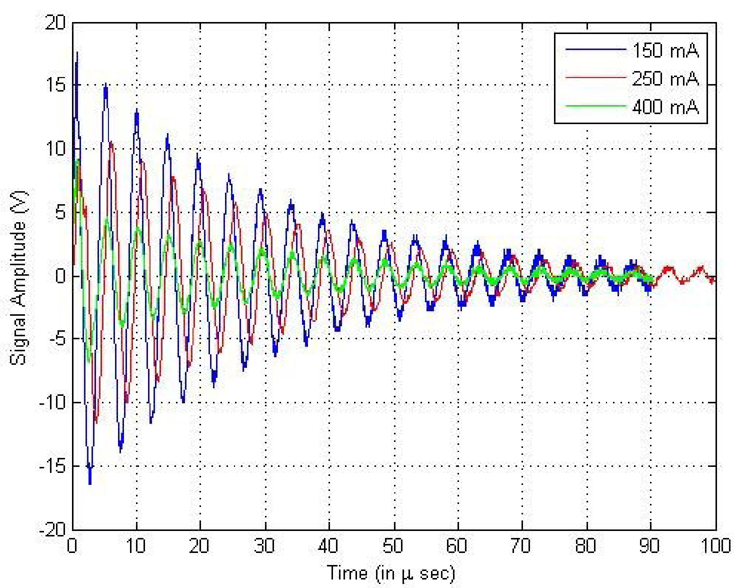

Fig 5.10: Breakdown signal at varying beam current

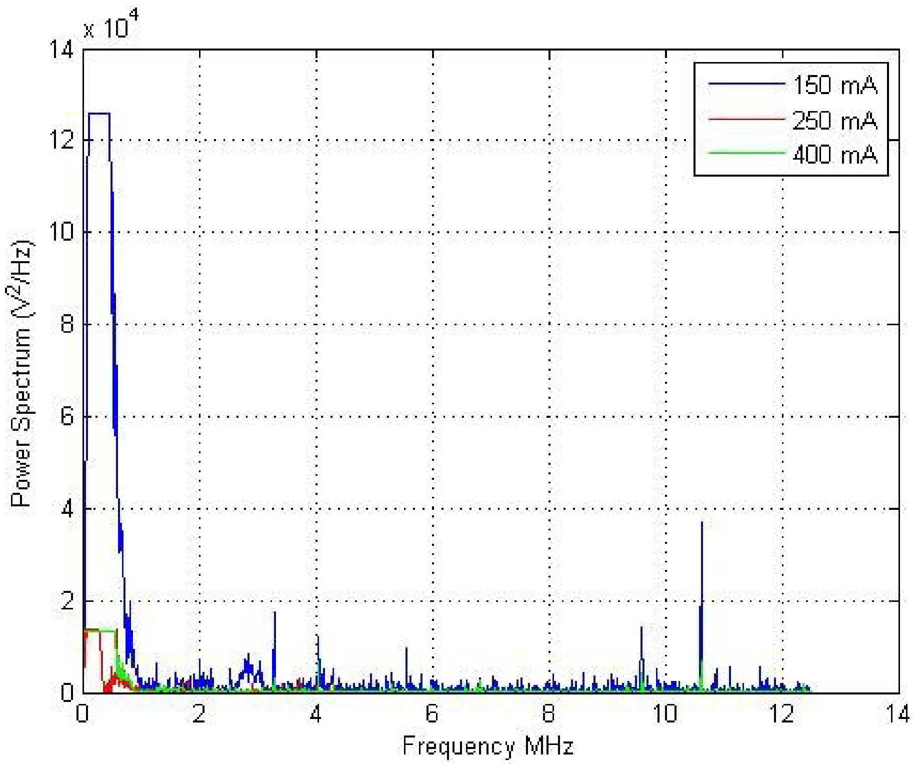

Fig 5.11: Power spectrum at varying beam current

5.4 Discussion

Breakdown current signal has been monitored using the sensor coil and captured using a storage oscilloscope. Spectral analysis provides the frequency components of the breakdown signal which helps in designing and selecting the ferrite bead to reduce the breakdown problem. The power spectrum of the breakdown signal reduces by a factor of nine when ferrite bead is used. Also the rise time, fall time of the breakdown signal increase and the settling time reduces due to use of ferrite bead. Using the ferrite bead DC passes fully, but rejects best between 1-10 MHz and somewhat lesser extent a decade above and a decade below. Our ferrites act like a band reject filter without a sharp cut off.

CHAPTER 6

Optimization of parameters on microstructure and optical properties of aluminum oxide coating

Evaporation of alumina results in dissociation and loss of oxygen and hence reactive evaporation under oxygen-ambient has been carried out to compensate the oxygen loss. Pure (better than 99.9 %) quality oxygen gas (O_2) has been bled in the system during deposition and films have been deposited at various oxygen flow rates. Optical and morphological properties of the films have been studied by Spectroscopic Ellipsometry (SE) and Atomic Force microscopy (AFM), while densities of the films have been determined by Grazing Incidence X-ray reflectivity (GIXR) and atomic ratios of oxygen to aluminum have been estimated by X-ray Photoelectron Spectroscopy (XPS) measurements. Variations of the different properties of the Al_2O_3 films have been studied as a function of O_2 flow rate and the results of the different findings have been corroborated with each other. The motivation of this study was to obtain the optimum oxygen flow rate or partial pressure to achieve good quality films with reasonably high refractive index.

Aluminum oxide thin films have been deposited by reactive electron beam evaporation technique in a 10 kV, 10 kW, 270 deg bent-beam type electron beam evaporation system. The vacuum system consists of a diffusion pump backed by a rotary pump and it provides a base pressure of 1x 10^{-4} Pa. Evaporation grade alumina granules have been used as the evaporant material which is placed on water cooled copper crucible and silicon substrate has been mounted 180 mm above the evaporant surface without any external heating. The oxygen flow rate has been varied to adjust the working pressure in the range of 4x 10^{-2} Pa to 1x 10^{-2} Pa. As the addition of oxygen increases the pressure inside the chamber by an order of magnitude, the partial pressure of oxygen can be taken as 90 % (approx) of the total pressure.

The optical properties of the coatings have been studied by SE technique using a phase-modulated ellipsometer (Model UVISEL™ 460, ISA JOBIN-YVON SPEX) in the wavelength range of 300-1200 nm. The surface morphology has been measured by AFM using NT-MDT's Solver P-47H multimode ambient based Scanning Probe Microscope system. The measurements have been carried out in the "contact mode" to reduce the noise level and the built-in statistic module of the control software "NOVA-SPM" was employed to determine the various parameters relevant to surface topology. GIXR measurements have been carried out in a Grazing Incidence X-ray Reflectometer (SOPRA, France) using a Cu K_α (1.54Å) source. The measurements have been carried out in the grazing angle of incidence range of 0-3° with an angular resolution of 0.001°. Rocking curve measurement has been done prior to each measurement for proper alignment of the sample. XPS measurements were carried out using a VSW ESCA machine equipped with a hemispherical analyzer and an Al K_α source with resolution of 0.9eV. The base pressure in the analysis chamber was maintained below $6.0x10^{10}$ Torr. All the XPS spectra were recorded after sputter-cleaning with 500eVAr^+ ion beam with beam current of 17μAmp/cm^2. C (Carbon)1s line was taken as internal reference with a binding energy of 284.6eV due to adventitious carbon on the surface.

6. 1 Results and discussion

6.1.1 Spectroscopic ellipsometric measurements

Most of the measurements on optical properties of the Al_2O_3 films have so far been made by transmission measurements using spectrophotometer or by ellipsometric measurement at a single wavelength. Although spectrophotometry can effectively be used to extract optical constants in case of homogeneous films, it becomes highly inefficient and inaccurate if the films contain inhomogeneity due to presence of voids/roughness which is very common for e-beam evaporated dielectric films. In such cases, SE provides a reasonably accurate method for the determination of optical constants of dielectric thin films.

In ellipsometry, the variation of the amplitude and the phase difference between the parallel (p) and the perpendicular (s) components of the reflected light polarized with respect to the plane of incidence are measured by the two quantities, viz. 1) which measures the amplitude ratio and 2) which measures the relative phase change.

These are given by [61]:

$$\rho = r_p/r_s = \tan\psi \exp(i\Delta) \tag{6.1}$$

where, r_p and r_s are the reflection coefficients for the p and s component of the waves respectively. Conventional ellipsometry techniques suffer from the drawback of slow data acquisition process and limited spectral range. However, the Phase Modulated Spectroscopic Ellipsometry technique employed in this study, offers fast and precise data acquisition over a large wavelength range. In this technique, a photo-elastic modulator, which is actually a fused silica bar, is subjected to periodical stress induced by a piezoelectric transducer at a frequency of 50 kHz. Due to its photo-elastic property, the modulator induces a phase shift between the two eigenmodes. The modulated intensity signal is detected and Fourier analysed to generate the parameters of interest viz., Ψ and Δ [62].

Fig.6.1 (a) and (b) show the experimental Ψ and Δ spectra respectively over a wavelength range of 300-1200 nm for a representative Al_2O_3 film (sample no: 10) deposited on c-Si substrate with an O_2 flow rate of 4 Sccm. The measured ellipsometry data are then fit with an appropriate theoretical model assuming a realistic two-layer sample structure with a bulk-like dense layer on the substrate and a top surface roughness layer. As the film thickness increases during deposition, the deeper lying atoms are subjected to stronger inter-

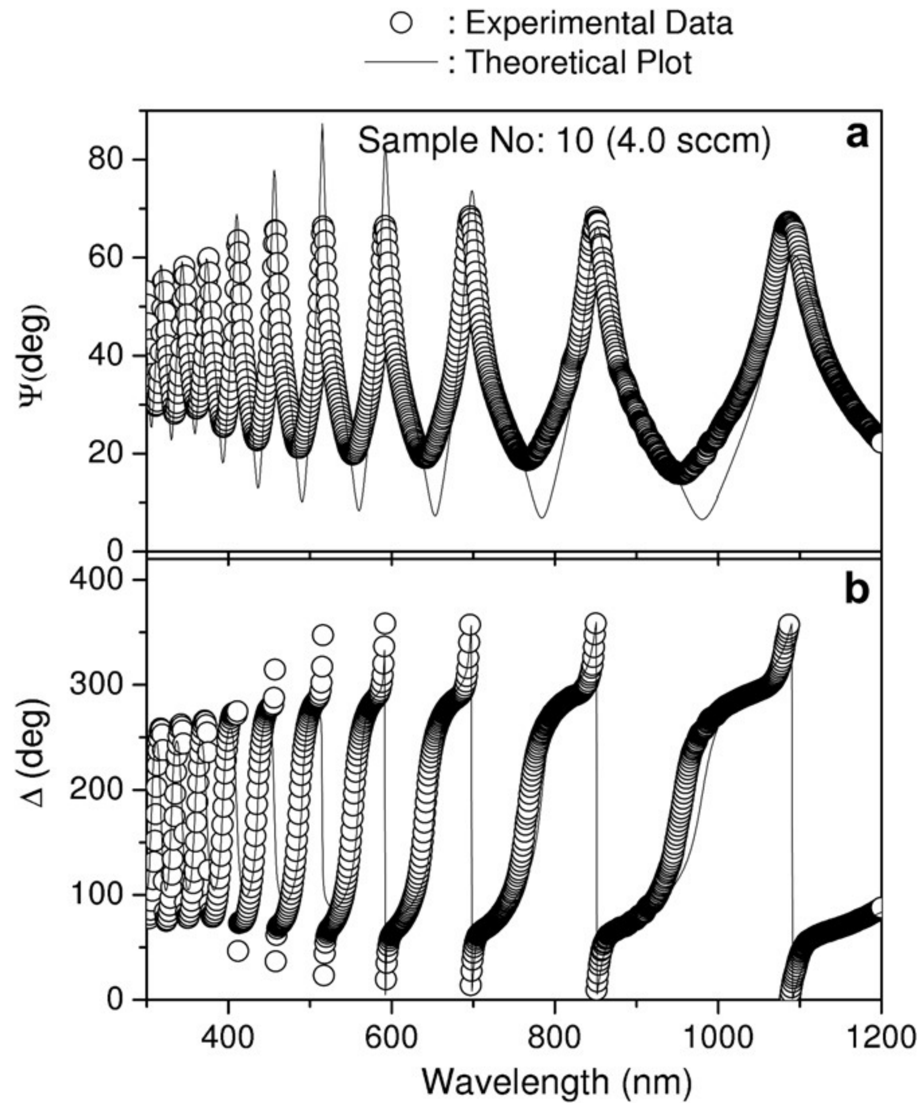

Fig.6.1: Ellipsometric spectra of a representative Al_2O_3 film along with best-fit theoretical spectra: (a) ψ vs. wavelength and (b) Δ vs. wavelength.

atomic forces and form a compact structure whereas the atoms near the surface are subjected to less inter-atomic force and thus form a spongy loose packed structure resulting in the surface roughness [63]. The surface roughness layer is modeled as a homogenous mixture of 50% material and 50% void which is a usual practice in ellipsometric analysis of thin films [64]. A model dispersion relation, has been used to describe the variation of optical constants of Al_2O_3 as a function of wavelength. Since X-ray Diffraction studies on these Al_2O_3 films do not show any crystalline structure, in ellipsometric analysis we have applied the Tauc-Lorentz (TL) dispersion model, proposed by Jellison and Modine [65] for amorphous materials, as the theoretical dispersion relation for optical constants of Al_2O_3. For layers containing voids, the calculation of the effective dielectric constant has been done using Bruggeman Effective Medium Approximation (EMA) model [59]. Assuming the above sample structure the theoretical ellipsometric spectra are generated and fitted with the measured ellipsometric spectra by minimizing the squared difference (χ^2) between the measured and calculated values of the ellipsometric parameters The maximum number of iterations allowed is 100 and the criteria for convergence used is $\delta\chi^2 = 1 \times 10^{-6}$.

Fig.6.1 (a) and (b) also show the best fit theoretical ellipsometric spectra for the sample no. 10. The best fit sample structure for the above sample, as obtained from the ellipsometric fitting, has been shown in Fig. 6.2 along with the dispersion of refractive index generated with the best fit parameters of the dispersion model. The above exercise has been carried out on several samples deposited with different O_2 flow rates and the relative thickness (d_s) of the top layer of the Al_2O_3 films (in percentage of total thickness) have been presented in Fig.6.3 (a) for all the samples as a function of O_2 flow rate used during deposition. It is found that though all the films have a top void-prone roughness layer, the relative thickness of the top layer is rather low (within 6% of the total thickness) for all the films and hence refractive index of the films should be close to that of the bulk layers, as obtained from the SE measurement for the respective films. The refractive index values in the near infrared region (i.e., @1200 nm) as obtained from the ellipsometric analysis have been shown in Fig.6.3 (b) for all the samples as a function of O_2 flow rate used during deposition. It has been observed from Fig.6.3 (b) that with the increase in the O_2 flow rate, refractive index increases and

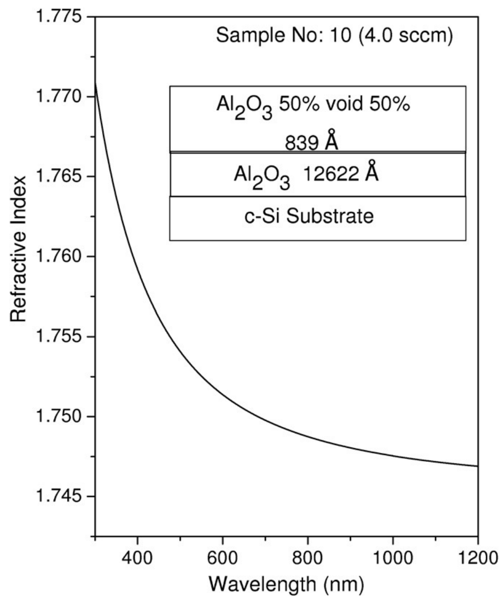

Fig.6.2: Refractive index vs. wavelength of the representative Al_2O_3 film alongwith best-fit sample structure

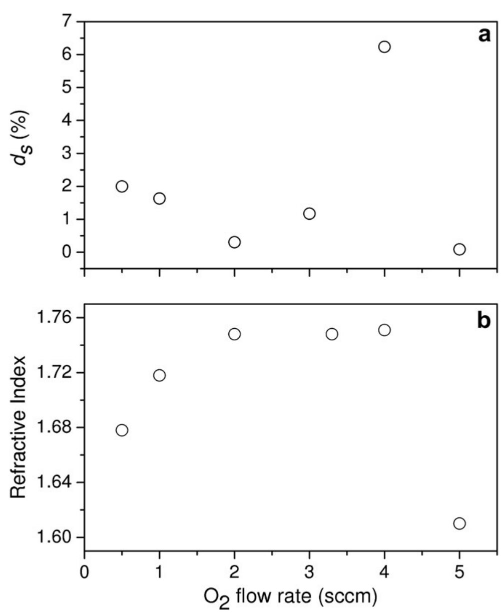

Fig.6.3: (a) Thickness (d_s) of the top layer of the Al_2O_3 films (in percentage of total thickness) vs. O_2 flow rate. (b) Refractive index of Al_2O_3 films vs. O_2 flow rate.

achieves a maximum ~ 1.75 for O_2 flow rate in the range of 2-4 sccm. The refractive index values of these Al_2O_3 films are found to be reasonably high when compared with Al_2O_3 films deposited by most of the other techniques and even by e-beam evaporation technique by other workers [57,58]. Comparable refractive index has been obtained by PIAD technique [59] where an additional plasma source was used to bombard the e-beam evaporated film in-situ. FCVA technique [50-51] has also been able to produce films with similarly high refractive index. Zhao et al [51] has found that in case of Al_2O_3 films deposited by FCVA technique, the refractive index of the films decreases as O_2 pressure in the deposition ambient is increased. However, reverse trend has been found in case of the present e-beam evaporated films except for the film deposited at flow rate above 4 sccm, for which the refractive index decreases. The possible reason for the observed refractive index variation might be morphological or stoichiometric/density changes in the samples which have been investigated subsequently by AFM, GIXR and XPS measurements.

6.1.2 AFM measurement

The morphology of the films has been characterized by AFM measurements. For all the samples, from the discrete height measurement data on the 2.5 µm x 2.5 µm area of the samples, a height–height correlation function $H(r)$ defined as follows has been generated [66]:

$$H(r) = \left\langle \left[h(r) - h(0) \right]^2 \right\rangle \qquad (6.2)$$

where, $h(r)$ is the surface height at position $r\left[=(x, y)\right]$ on the surface and the notation $\langle ... \rangle$ means the statistical average over all the points on the surface. Fig.6.4 (a) shows the AFM micrograph of a representative sample (sample no.10) while fig. 6.4 (b) shows the $H(r)$

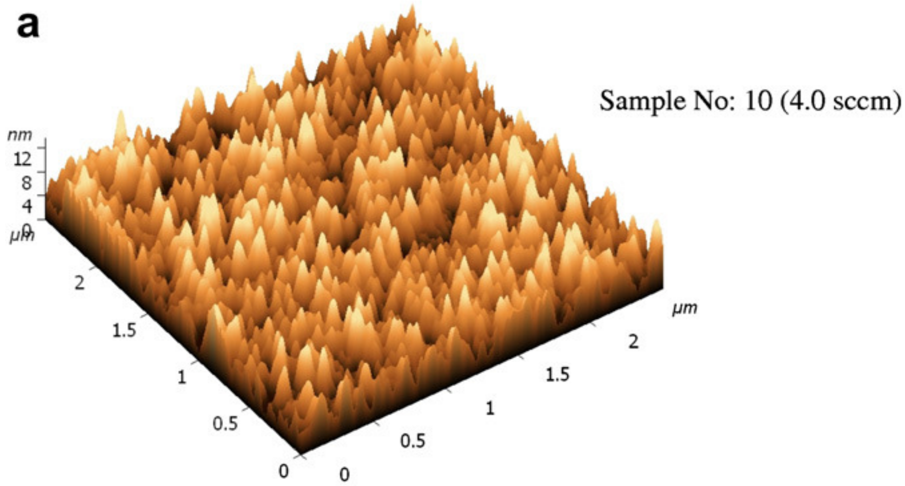

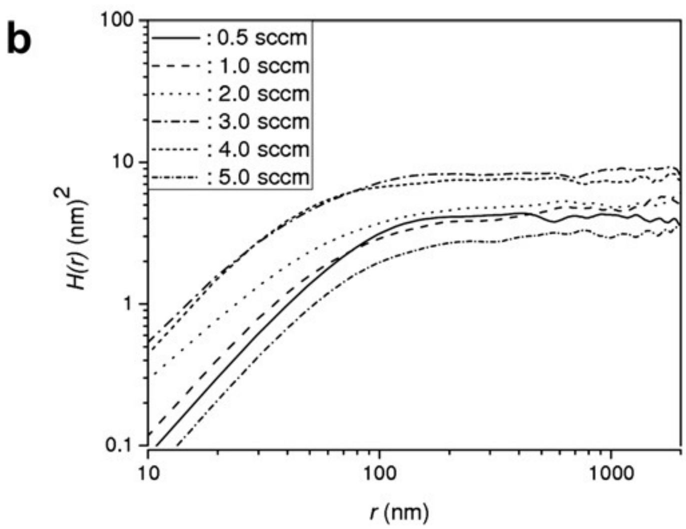

Fig 6.4: (a) AFM micrograph of a representative sample.

(b) Height–height correlation function $H(r)$ vs. position $r\left[=(x, y)\right]$ on the surface.

function for all the samples derived from their respective AFM micrographs. As expected it has been observed that, $\ln H(r)$ increases linearly with $\ln(r)$ for small values of r, depicting a power-law behavior represented by $H(r) \propto r^{2\alpha}$ and ultimately leads to saturation for large r. Thus empirically the above function can be written as [67]:

$$H(r) = 2\sigma^2 \left[1 - \exp\left\{ -\left(\frac{r}{\xi} \right)^{2\alpha} \right\} \right] \qquad (6.3)$$

Where ξ is the lateral correlation length, σ is the average interface width or rms roughness and α is the roughness exponent or Hurst parameter which controls the short range fractal dimension of the surface. All these parameters have very special significances with respect to the qualitative as well as quantitative behavior of the surface morphology. The roughness exponent (α), is indicative of the "jaggedness" of the topography of the surface, where large values of α signify less high frequency fluctuations. The lateral correlation length ξ describes the largest distance upto which the surface points can be considered correlated. It is to be further noted that ξ provides a length scale which distinguishes the short-range and long-range behaviors of the rough surface [68]. The interface width or r.m.s. roughness (σ), is a measure of the surface height fluctuation, i.e., it signifies the r.m.s. fluctuation about the mean height.

The $H(r)$ functions obtained for all the samples have been fitted with the expression (3), the parameters σ, ξ and α have been derived in each case and figs. 6.5 (a), (b) and (c) respectively show the variation of these parameters as a function of O_2 flow rate used during deposition. It has been found that the r.m.s. roughness (σ) values for the films are low (1-2 nm) considering the large thickness of the films (~1-2μm) and σ does not have any significant variation as a function of the O_2 flow rate except for marginal decrease for films deposited at O_2 flow rate above 4 Sccm. The correlation length (ξ) also improves for film deposited a high O_2 flow rate (5 Sccm) while the Hurst parameter increases monotonically with the increase in O_2 flow rate.

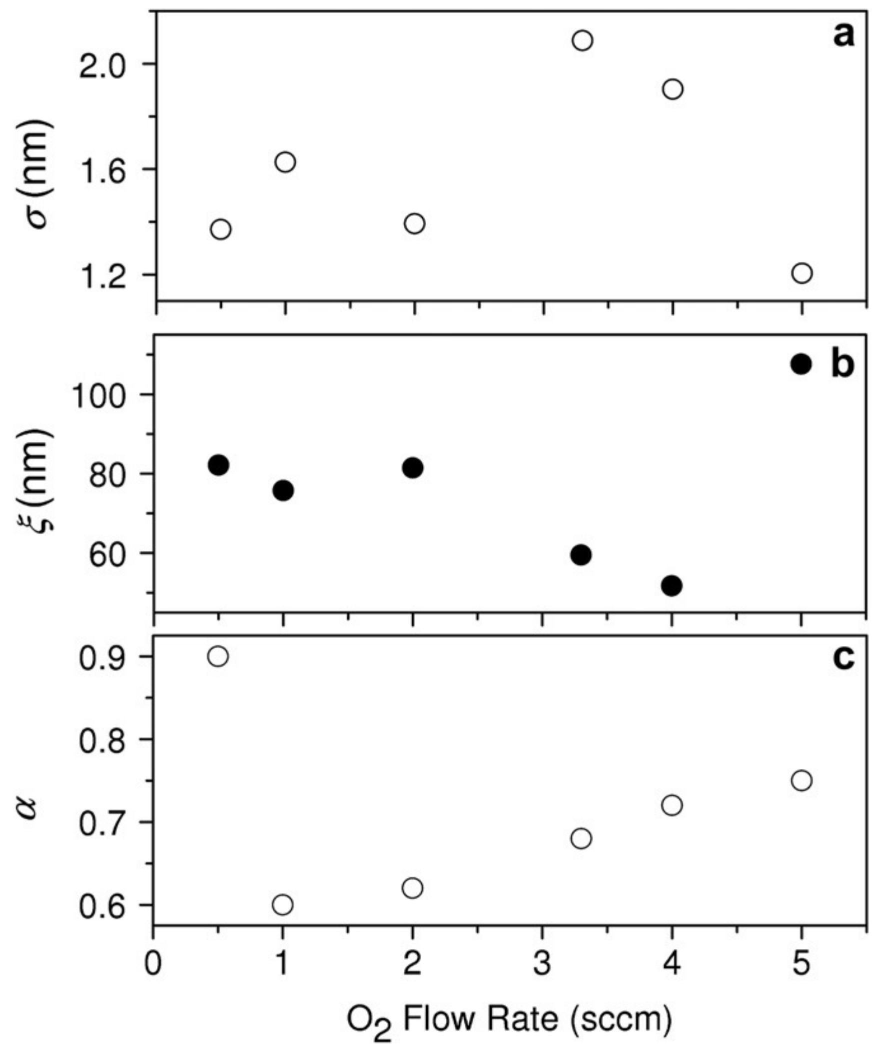

Fig 6.5: (a) R.M.S. roughness (σ) vs. O_2 flow rate.(b) Correlation length (ξ) vs. O_2 flow rate. (c) Roughness exponent (α) vs. O_2 flow rate.

Huang et al. [58] have observed that roughness increases as the O_2 partial pressure increases for their e-beam evaporated films and have attributed it to the enhanced collision among the vapor species and oxygen molecules. Koski et al. [46] have also made similar observations for r.f. magnetron sputtered Al_2O_3 films, where roughness and density of the films increase with higher gas pressure in the sputtering chamber. However in the present case, it has been observed that for films deposited at O_2 flow rate above 4 sccm, surface roughness decreases along with refractive index of the films. Since the decrease in refractive index in these films cannot be attributed to any significant morphological detoriation in the samples, investigations on the density of the samples have been carried out by GIXR measurements.

6.1.3 GIXR measurement

The basic theory of X-ray reflectivity is derived from classical optics and Frensel theory, modified slightly for X-ray. The complex refractive index (η) of an element in the X-ray region is given by [69]:

$$\eta = 1 - \delta - i\beta \tag{6.4}$$

where,

$$\delta = \left\{ \frac{r_0 \lambda^2}{2\pi} \right\} N_A \left(\frac{\rho Z}{A_w} \right) \tag{6.5}$$

and

$$\beta = \left(\frac{\mu \lambda}{4\pi} \right) \tag{6.6}$$

where, r_0 is the classical electron radius (2.82 x 10^{-13} cm), N_A is the Avogadro number, ρ is the density, Z is the atomic number, A_w is the atomic weight of the element and μ is the linear absorption coefficient of the material at the particular wavelength λ. The quantity $\left[N_A (\frac{\rho Z}{A_w}) \right]$ actually gives the number of electrons per cm^3 of the particular element.

Under the well-known Parrat formalism [63], the reflectivity of X-rays from a plane boundary between two media can be obtained using Fresnel's boundary conditions of continuity of the tangential components of the electric field vector and its derivative at the interface. Since refractive index of all materials in hard X-ray region is < 1, X-ray reflectivity at very low grazing angle of incidence is ~1 (total external reflection regime) and for grazing angle of incidence above the critical angle value defined by:

$$\theta_c = \sqrt{2\delta} \qquad (6.7)$$

X-rays start penetrating inside the layer and the reflectivity falls off at a rate defined by the absorption of the stack and in case of a thin film, is characterized by oscillations defined by the thickness of the film. Hence analysis of the X-ray reflectivity spectrum can yield information regarding density and thickness of a thin film accurately.

However, the Fresnel's reflectivity gets modified for a rough surface by a 'Debye-Wallar -like' factor as follows [70]:

$$R_0 = R_p \exp(-\frac{q^2\sigma^2}{2}) \qquad (6.8)$$

where, q is the momentum transfer factor (= $4\pi\sin\theta/\lambda$), R_0 is the reflectivity of the rough surface and R_p is the reflectivity of an otherwise identical smooth surface and σ is the r.m.s. roughness of the surface.

In fig.6.6, X-ray reflectivity spectrum of one representative sample (sample no.11, deposited at 0.5 sccm O_2 flow rate) has been shown along with the best-fit theoretical spectrum. It should be noted that the disagreement between experimental and theoretical spectra below the critical angle is due to the "foot-print effect", where the long foot print of the X-ray beam at extreme grazing incidence extends beyond the finite size of the sample. Since the thickness of the Al_2O_3 films are too large (~ 1-2μm) to be resolved by oscillations in X-ray reflectivity spectra, thickness values obtained from SE measurements has been accepted and kept invariant during the GIXR fitting of the respective samples and the other two parameters viz., density and surface roughness of the films have been derived from the fitting. The variation in surface roughness (σ_{GIXR}) of the films as a function of O_2 flow rate

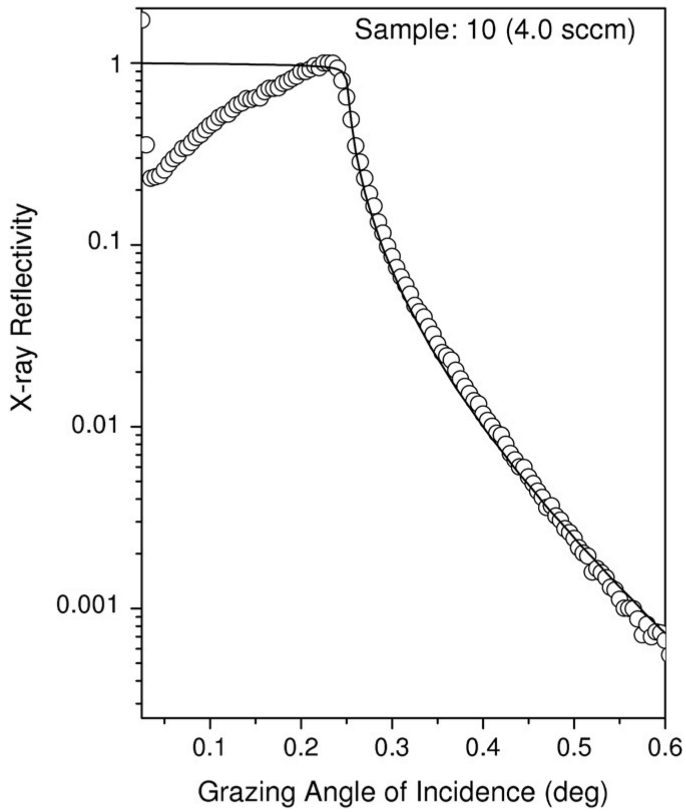

Fig 6.6: GIXR spectra of a representative Al_2O_3 film

has been shown in Fig.6.7 (a) which shows that σ_{GIXR} values quantitatively agree well with σ values (obtained from AFM measurements) for the films and do not show any significant variation with O_2 flow rate. The variation in density of the samples as a function of O_2 flow rate has been shown in Fig 6.7 (b) which shows that the density decreases both at lower (0.5 sccm) as well as higher (5 sccm) O_2 flow rate and is higher for the film deposited at a O_2 flow rate in the range 2-4 sccm. The density variation pattern of the films, as a function of O_2 flow rate, matches with the refractive index variation pattern and hence the refractive index variation can be attributed to the variation in density of the films. To further investigate the origin of the density variation the O/Al ratio in the films has been estimated by XPS measurements.

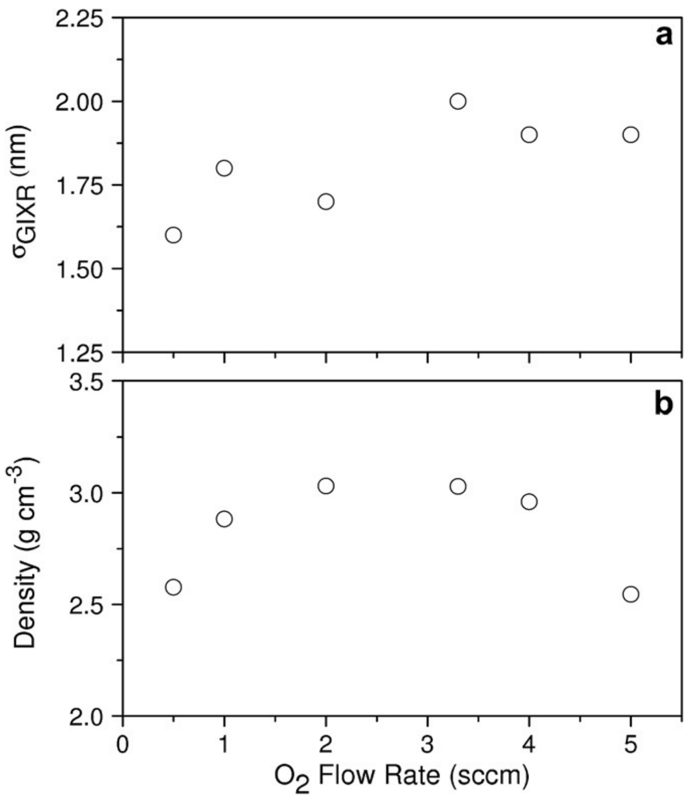

Fig.6.7: (a) Surface roughness (σ_{GIXR}) of Al_2O_3 films vs. O_2 flow rate.

(b) Density of Al_2O_3 films vs. O_2 flow rate.

6.1.4 XPS measurement:

Fig. 6.8 shows the XPS survey scan of a representative Al_2O_3 film (sample no: 2, deposited at 3.3 sccm O_2 flow rate) recorded in the binding energy range of 0-600eV. The positions of the Al and O peaks in the spectrum agree well that reported by Zhang et al. [71] for Al_2O_3 film prepared by Atomic layer deposition technique. For determining atomic ratios of aluminum and oxygen in the samples, narrow-range XPS scans for O_{1s} and Al_{2p} core levels have been taken for all the samples. Quantitative analysis of atomic ratios was carried out by determining the elemental peak areas, following Shirley background subtraction by the usual

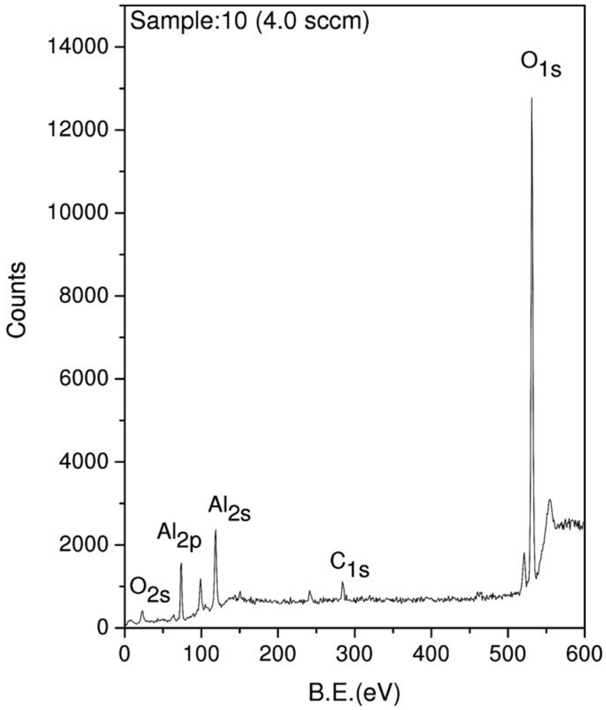

Fig.6.8: XPS survey spectrum of a representative Al_2O_3 film.

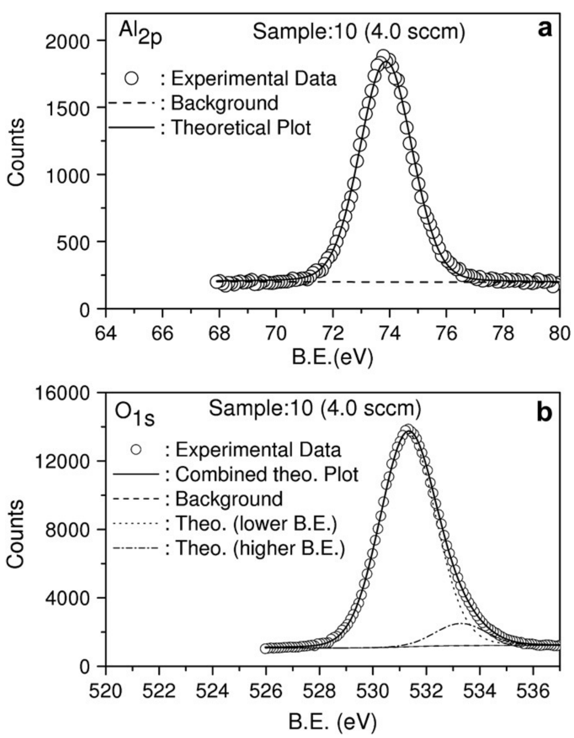

Fig.6.9: Narrow-range XPS spectra along with theoretical fit. (a) Al_{2p} (b) O_{1s}

procedure [72] and using the sensitivity factors supplied with the instrument. Fig.6.9 shows the Al_{2p} and O_{1s} core level spectra for a representative sample (sample no: 2, deposited at 3.3 sccm O_2 flow rate) along with the theoretical fittings. As can be seen from figure 6.9, the Al_{2p} peak could be fitted with only one peak, showing that aluminum may be present only in Al_2O_3 form in the film whereas the O_{1s} spectrum could be best fitted with two peaks. The oxygen peak (minor one) at higher binding energy may be related to the presence of carbon contamination (typical for oxygen bonded to carbons) [73], while the major peak at lower binding energy can be assigned to oxygen bonded with aluminum in Al_2O_3 form and the later has been considered for calculating the atomic ratios. The variation in O/Al atomic ratio in the Al_2O_3 films, estimated from the XPS spectra as discussed above, has been shown in Fig.6.10 as a function of O_2 flow rate used during deposition of the films. It is found that atomic ratio (O/Al) values for Al_2O_3 films are more than 1.5 for all the samples indicating oxygen rich stoichiometry of the films. Also the figure shows higher oxygen contents for films deposited at O_2 flow rates of 5 sccm and at 0.5 sccm, which explains the decrease in density and refractive index of the samples prepared at these flow rates. The relatively higher oxygen-content in the films prepared at higher O_2 partial pressure is well understood to be due to higher rate of supply of oxygen than the rate of dissociation of Al_2O_3. Figure 6.10 also shows relatively lower oxygen content at 3.3 sccm as shown by rectangular legend. This is due to high deposition rate at 3.3 sccm as shown in the figure 6.11.

6.2 Discussion

Thin films of alumina (Al_2O_3) have been deposited by a conventional e-beam evaporation system through reactive evaporation of alumina under high purity O_2 flow. The films have been characterised by Spectroscopic Ellipsometry (SE), Atomic Force Microscopy (AFM), Grazing incidence x-ray reflectivity (GIXR) and X-ray photoelectron Spectroscopy

(XPS) measurements and the effect of oxygen flow rate on the properties of the Al_2O_3 films has been determined. It has been observed that films prepared under O_2 flow rate of 2-4 sccm show reasonably high refractive index ~ 1.75, while, refractive index is low for films prepared under both higher (~5 sccm) and lower (~0.5-1 sccm) O_2 flow rates. Such variation in refractive index with O_2 flow rate could not be attributed to morphological changes since AFM measurements show no significant variation in surface roughness with change in O_2 flow rate. However, GIXR measurement reveals that the densities of the films prepared at both higher and lower O_2 flow rates are low, while higher density is obtained for films prepared at O_2 flow rate in the range 2-4 sccm, which explains the observed variation in refractive index. XPS measurements in turn, reveal that the observed variation in density of the films is due to a variation in O/Al ratio in the films.

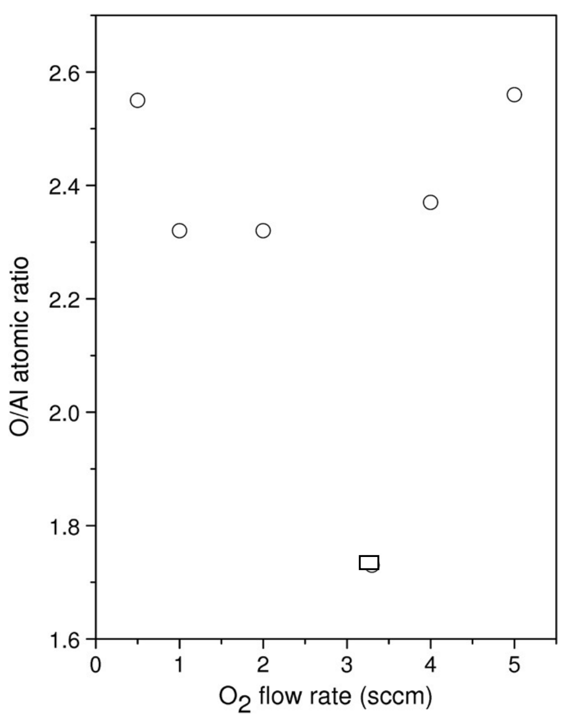

Fig.6.10: O/Al atomic ratio of Al_2O_3 films vs. O_2 flow rate.

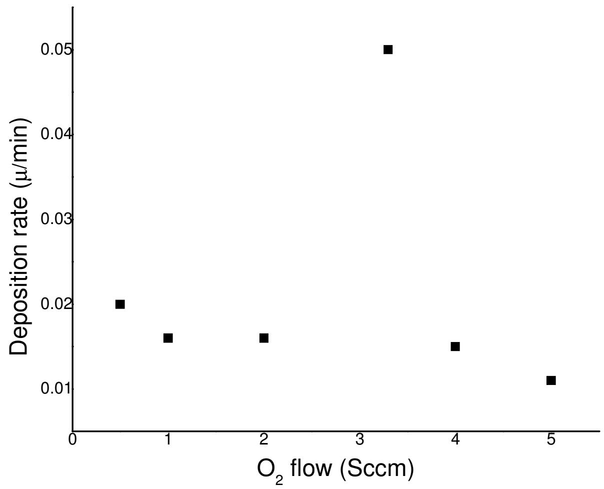

Fig.6.11: Deposition rate vs. O_2 flow rate.

CHAPTER 7

Summary and future directions

1. High power strip electron gun finds a lot of usage in reactive and large area coating. Development of an indirectly heated cathode overcomes all the shortcomings of a directly heated cathode. Also one cannot use an indirectly heated cathode with simple rectangular cross section due to multiple beam problem. Therefore the indirectly heated cathode of trapezoidal cross section has been designed. Optimization of solid cathode configuration has been analyzed on the basis of uniformity in temperature distribution on the surface of the cathode as well as with stress distribution for mechanical integrity of the gun. The near uniform temperature of 2500 K over 110 mm length has been obtained with a band of 150 K which will give rise to desired emission in space charge limited region for the evaporation applications. One can achieve uniformity within 100 K by suitably modifying the fin structure.

   In the future scope, the uniformity of temperature on the solid cathode using (a) a multi-segmented filament with variable height as the primary heat source and (b) trapezoidal shaped single long filament as the primary heat source can be improved.

2. Design of a 10 kV, 10 kW transverse electron gun has been presented in this work through systematic modeling and simulation approach. The reactive coating of desirable properties can be achieved in the pressure range of 10^{-1} Pa to 10^{-2} Pa. At this high pressure the electron gun does not operate reliably due to high voltage flashover. In order to overcome this problem substrate chamber is isolated from gun chamber using a bifurcation plate. All aspects of design of an electron gun for a differentially pumped reactive evaporation system has been detailed in this work.

Since all the parts are integrated for a specific end use, modifications to suit special requirements are within our control and can be exploited as and when necessary.

3. When the coating process is modeled suitably, the desired coating can be predicted apriori and therefore the parameters required to obtain it. In this work, CFD modeling has been used to simulate the vapor transport for metallic coating as well as reactive coating. Metallic coating result has been validated with the help of titanium coating. In case of reactive coating, yttria has been used, various reactions involved has been demonstrated. The validation with the help of experiments can be a part of future course of actions.
4. Thin films of alumina (Al_2O_3) have been deposited by reactive electron beam evaporation technique in a 10 kV, 10 kW, 270 deg bent-beam type electron beam evaporation system under high purity O_2 flow. The films have been characterised by Spectroscopic Ellipsometry (SE), Atomic Force Microscopy (AFM), Grazing incidence X-ray reflectivity (GIXR) and X-ray photoelectron Spectroscopy (XPS) measurements and the effect of oxygen flow rate on the properties of the Al_2O_3 films has been determined. It has been observed that films prepared under O_2 flow rate of 2-4 sccm show reasonably high refractive index ~ 1.75, while, refractive index is low for films prepared under both higher (~5 sccm) and lower (~0.5-1 sccm) O_2 flow rates. Such variation in refractive index with O_2 flow rate could be attributed to a variation in O/Al ratio in the films.
5. During the operation of any electron gun, the vacuum breakdown not only spoils the job but also causes a lot of damage to the electronics of the system. Our approach is to attenuate the breakdown current near the gun, so that the surge does not propagate to cause any detrimental effect on the power source and thereby on the job. In this work, ferrite beads have been used to suppress the high frequency content and reduce the

amplitude of the breakdown signal. Spectral analysis provides the frequency components of the breakdown signal which helps in designing and selecting the ferrite bead to reduce the breakdown problem. The peak amplitude of the breakdown signal reduces by a factor of two when ferrite bead is used. Also the rise time, fall time of the breakdown signal increase and the settling time reduces due to use of ferrite bead. The selection of a suitable ferrite bead can help reduce the high voltage breakdown related problem in the electron beam evaporation system.

REFERENCES

1. J.R. Pierce, "Theory of Design of Electronic Beams," D. Van Nostrand Company Inc., New York, New York, (1954).

2. B.N, Lewis, H.T. Tran, R.L. Ives, M. Read, "Design of and Electron Gun Using Computer Optimization", IEEE Trans. on Plasma Sci., 32, 1242- 1250, (2004).

3. J. David, L. Ives, H.T. Tran, T. Bui, M.E. Read, "Computer optimized design of electron guns", IEEE Trans. Plasma Sci., 36, 156-168, (2008).

4. K.B. Thakur, G.K. Sahu and R.V. Tamhankar, Patel Kartik, "High power, high uniformity strip electron gun design, simulation and performance", Rev. Sci. Instrum., 72 , 207–215, (2001).

5. R. Avida, J. Yeheskel,M. Friedman, D. Gazit, and D. Levron, "Magnetically focused line source electron gun", Rev. Sci. Instrum., **53**, 1577-1580, (1982).

6. Munawar Iqbal, Khalid Masood, Mohammad Rafiq and Maqbool A. Chaudhary, Fazal-e-Aleem, "An electromagnetically focused electron beam line source", Rev. Sci. Instrum. , 74, 4616-4619, (2003).

7. M. Iqbal and F. Aleem, "Design and performance of high uniformity linear filament electron gun", Rev. Sci. Instrum. **77**, 106101-1-3, (2006).

8. J. Yeheskel, D. Gazit, R. Avida, and M. Friedman, "An intense electron beam source", J. Phys. D., 16, 499-504, (1983).

9. Munawar Iqbal,Maqbool A. Chaudhary, M. Rafiq and Khalid Masud, “An indirectly heated electron beam emitter assembly”, Rev. Sci. Instrum., 74, 1196-1199, (2003).

10. Khalid Masood, Surfraz A. Bhatti, Mohammad Zakaullah, “Development of directly and indirectly heated thermionic electron beam sources at EBSDL”, Vacuum, 82, 1386–1390, (2008).

11. Namita Maiti, S. Mukherjee, Bhunesh Kumar, U. D. Barve, V. B. Suryawanshi, and A. K. Das, “Design and development of indirectly heated solid cathode for strip type electron gun”, Rev. Sci. Instrm, 81, 013302-1-10, (2010).

12. Herniter M.E. and Getty W.D., “Development of High Current Density LaB6 Thermionic Emitters for a Space Charge Limited Electron Gun”, PAC, 292-294, (1987).

13. W. B. Hermannsfeldt, *EGUN—An Electron Optics and Gun Design Program*,SLAC Report, 331, (1988).

14. A. Banerjee, S.K. Barthwal and K.L. Chopra, “Design of a bent beam electron gun for evaporation”, Rev. Sci. Instrm., 47, 1410-1411, (1976).

15. Pallab Karmakar, Namita Maiti, A.V. Bapat, “Design and Performance of Differential Pumping System of Coating Unit”, Journal of Physics: Conference Series 114, 012069-1-9, (2008)

16. Namita Maiti, U. D. Barve, M. S. Bhatia, and A. K. Das, “Design of transverse electron gun for electron beam based reactive evaporation system”, Rev. Sci. Instrum., 82, 056106-1-3, (2011) .

17. A. Powell, P. Minson, G. Trapaga, and U. Pal, “Mathematical Modeling of Vapor-Plume Focusing in Electron-Beam Evaporation,” Metallurgical and Materials Transactions, 32A, 1959-1966, (2001).

18. S. Baek, V. Prabhu, "Finite element model for unified EB-PVD machine dynamics", Surface Engineering, 23, 453–463, (2007).

19. Seungyup Baek, Vittaldas Prabhu, "Computational Model for Substrate Motion in EB-PVD Process", Materials and Manufacturing Processes, 24, 1331–1336, (2009).

20. Indraneel Fuke, Vittaldas Prabhu, and Seungyup Baek, "Computational model for predicting coating thickness in electron beam physical vapor deposition", Journal of Manufacturing Processes,7, 140-152, (2005).

21. Laurentiu Nastac, William Hanusiak, Hao Dong, and F. Robert Dax, "The CFD Modeling of the EB-PVD of SiC/Ti-6Al-4V Coatings", JOM, 56, 49-53, (2004).

22. L. Nastac, F.R. Dax and W. Hanusiak, "Methodology for modeling the EB-PVD coating process", J. Phys. IV France, 120, 307-314, (2004).

23. Schiller S., Heisig U., Panzer S., *Electron Beam Technology,* John Wiley Publisher, (1982).

24. H.S. Wahab and C.L. Chakrabarti, "Mechanism of yttrium atom formation in electro-thermal atomization from metallic and metal-carbide surfaces of a heated graphite atomizer in atomic absorption spectrometry", Spectrochimica Acta, 36B, 475 - 481, (1981).

25. B. Dixit, M. S. Bhatia, "Hysteresis in Electron-Emission current of an axial electron gun used for evaporation of metals", IEEE Trans. on Plasma Science, 35, 396-401, (2007)

26. Luis A. Zuniga, Michael E. LaFrance, Larry F. Willitzer, Christopher S. Johnson, "Arc free electron gun", U. S. Patent No. 6,064,686, (2000).

27. A.V. Arkhipov, G.G. Sominski, “Gun breakdown prevention in a system with dense non-relativistic electron beam focused on a solid target in pulses with millisecond duration”, IEEE 18th Symp on Discharges and Electrical Insulation in Vacuum, 762-764, (1998).

28. R. J. Hill, “Electron beam gun with grounded shield to prevent arc down and gas bleed to protect the filament”, U.S. Patent No. 6476340, (2000).

29. G. Sayegh, “Control of discharge initiation in high-intensity electron-beam generators for metal processing”, I.E.E.E. Trans. on Electrical Insulation, 24, 959-962, (1989).

30. H. Kita , S Satoh, S. Matsui, S. Yasunaga, H. Irie, *Electron and laser beam welding,* Oxford, Pergamon Press, (1986).

31. O.K. Nazarenko, O.A. Gurin and E.I. Bolgov, “Features of current protection of power sources for EBW”, The Paton Welding J, 1, 2-4, (2013).

32. James M. Constable, “Surge voltage protection system”, U.S. Patent No. 3,678,341, (1972).

33. Slawomir Tumanski, “Induction coil sensors-a review”, Meas. Sci. Technol., 18, R31-R47, (2007).

34. H.A. Wheeler, “Inductance formulas for circular and square coils”, Proc. of the IEEE, 70, 1449-1450, (1982).

35. R.G. Medhurst, “H.F. resistance and self-capacitance of single-layer solenoids”, Wireless Engineer, 24.281, 35-43, (1947) .

36. Robert West, “Common mode inductors for EMI filters require careful attention to core material selection”, MAGNETICS Technical Bulletin, FC-S2, (1994).

37. Magnetics Powder Core Catalog, 2011-1, (2011).

38. Jakschik S, Avellan A, Schroeder U, Bartha, "Influence of Al O Dielectrics on the Trap-Depth Profiles in MOS Devices Investigated by the Charge-Pumping Method", J, IEEE Trans Electron Devices, 51, 2252- 2255, (2004).

39. Pauleau Y, Barna P.B, *Protective Coatings and Thin Films: Synthesis, Characterization and Applications*, Springer, (1997).

40. Song E.P, Ahn J, Lee S, Kim N.J, "Microstructure and wear resistance of nanostructured Al2O3–8 wt% TiO2 coatings plasma-sprayed with nanopowders", Surf Coat Technol, 201, 1309-1315, (2006).

41. Phani A.R, Gammel F.J, Hack T, "Structural, mechanical and corrosion resistance properties of Al2O3-CeO2 nanocomposites in silica matrix on Mg alloys", Surf Coat Technol, 201, 3299-3306, (2006).

42. Khanna A, Bhat D.G, Harris A, Beake B.D, "Structure–property correlations in aluminium oxide thin films grown by reactive AC magnetron sputtering", Surf Coat Technol, 201, 1109-1116, (2006).

43. Ha W.H, Choo M.H, Im S, "Electrical properties of Al2O3 film deposited at low temperature", J Non-Cryst Sol, 303, 78-82, (2002).

44. Wang J, Yu Yuan-Hsin, Lee SC, Chung Yip-Wah, "Tribological and optical properties of crystalline and amorphous alumina thin films grown by low-temperature reactive magnetron sputter-deposition", Surf Coat Technol, 146, 189-194, (2001).

45. Segda B.G, Jacquet M, Besse J.P, "Elaboration, characterization and dielectric properties study of amorphous alumina thin films deposited by r.f. magnetron sputtering", Vacuum, 62, 27-38, (2001).

46. Koski K, Holsa J, Juliet P, "Properties of aluminium oxide thin films deposited by reactive magnetron sputtering", Thin Solid Films, 339, 240-248, (1999).

47. Kelly P.J, Arnell R.D, "Control of the structure and properties of aluminum oxide coatings deposited by pulsed magnetron sputtering", J Vac Sci Technol A, 17, 945-953, (1999).

48. Chiu Re-Long , Chang Peng-Heng, "Thickness dependence of refractive index for anodic aluminium oxide films", J Mat Sci Lett, 16, 174-178, (1997).

49. Sproul W.D, Graham M.E, Wong M.S, Lopez S, Li D, Scholl R.A, "Reactive direct current magnetron sputtering of aluminum oxide coatings", J Vac Sci Technol A, 13, 1188-1191, (1995).

50. Tay B.K, Zhao Z.W, Sun C.Q, "Effects of substrate bias and growth temperature on properties of aluminium oxide thin films by using filtered cathodic vacuum arc", Surf Coat Technol, 198, 94-97, (2005).

51. Zhao Z.W, Tay B.K, Lau S.P, Xiao C.Y, "Microstructural and optical properties of aluminum oxide thin films prepared by off-plane filtered cathodic vacuum arc system", J Vac Sci Technol A, 21, 906-910, (2003).

52. Groner M.D, Elam J.W, Fabreguette F.H, George S.M, "Electrical characterization of thin Al2O3 films grown by atomic layer deposition on silicon and various metal substrates", Thin Solid Films, 413, 186-197, (2002).

53. Jakschik S, Schroeder U, Hecht T, Gutsche M, Seidl H, Bartha J.W, " Crystallization behavior of thin ALD-Al O films", Thin Solid Films, 425, 216-220, (2003).

54. Katiyar P, Jin C, Narayan R.J, "Electrical properties of amorphous aluminum oxide thin films", Acta Materialia, 53, 2617-2622, (2005) .

55. Lin C.H, Wang H.L, Hon M.H, "The effect of residual stress on the adhesion of PECVD-coated aluminum oxide film on glass", Thin Solid Films, 283, 171-174, (1996).

56. Aguilar-Frutis M, Garcia M, Falcony C,"Optical and electrical properties of aluminum oxide films deposited by spray pyrolysis", Appl Phys Lett, 72, 1700-1702, (1998).

57. Shamala K.S, Murthy LCS, Narasimha Rao K ,"Studies on optical and dielectric properties of Al2O3 thin films prepared by electron beam evaporation and spray pyrolysis method", Mat Sci Eng B, 106, 269-274, (2004).

58. Huang Hong-Hsin, Liu Yuan-Shing, Chen Yen-Ming, Huang Ming-Chih, Wang Moo-Chin, "Effect of oxygen pressure on the microstructure and properties of the Al2O3–SiO2 thin films deposited by E-beam evaporation", Surf Coat Technol, 200, 3309-3313, (2006).

59. Thielsch R, Gatto A, Heber J, Kaiser N, "A comparative study of the UV optical and structural properties of SiO2, Al2O3, and HfO2 single layers deposited by reactive evaporation, ion-assisted deposition and plasma ion-assisted deposition", Thin Solid Films, 410, 86-93, (2002).

60. Namita Maiti, A. Biswas, R. B. Tokas, D. Bhattacharyya, S. N. Jha, U. P. Deshpande U. D. Barve, M. S. Bhatia and A. K. Das , "Effects of Oxygen flow rate on microstructure and optical properties of Aluminum oxide films deposited by electron beam evaporation technique", Vacuum, 85, 214-220, (2010).

61. Azzam RMA, Bashara NM, *Ellipsometry and Polarized Light*, North-Hollannd, Amsterdam, (1977).
62. Drevillon B, "Phase modulated ellipsometry from the ultraviolet to the infra-red: in-situ application to the growth of semiconductors", Prog Cryst Growth & Character, 27, 1-87, (1993) .
63. Parrat I.G, "Surface Studies of Solids by Total Reflection of X-Rays", Phys. Rev., 95, 359-369, (1954).
64. M.H. Frasncombe and J.L. Vossen, "Optical Characterisation of Real Surfaces and Films, edited by K. Vedam, in Physics of Thin Films, edited by M.H. Frasncombe and J.L. Vossen (Academic Press, San Diego), 19, (1994).
65. Jellison G.E, Modine F.A, "Parameterization of the optical functions of amorphous materials in the interband region", Appl Phys Lett, 69, 371-373, (1996).
66. Liu Z.J, Jiang N, Shen Y.G, Mai Y.W, "Atomic Force Microscopy Study of Surface Roughening of Sputter-deposited TiN Thin Films", J Appl Phys, 92, 3559-3563, (2002).
67. Zhang C.H, Liu Z.J, Li K.Y, Shen Y.G, Luo J.B, " Microstructure, surface morphology, and mechanical properties of nanocrystalline THiN amorphous Si3N4 composite films synthesized by ion beam assisted deposition", J Appl Phys, 95, 1460-7, (2004).
68. Zhao Y.P, Yang H.N, Wang G.C, Lu T.M, "Extraction of real-space correlation function of a rough surface by light scattering using diode array detectors", Appl Phys Lett, 68, 3063-65, (1996).
69. James R.W, *The Optical Principles of Diffraction of X-rays*, Cornell University Press, NY, (1965).

70. Spliier E, “Characterization of multilayer coatings by X-ray reflection”, Rev Phys Appl, 23, 1687-1700, (1988).

71. Zhang L, Jiang HC, Liu C, Dong J.W, Chow P, “Annealing of Al2O3 thin films prepared by atomic layer deposition”, J Phys D Appl Phys, 40, 3707-3713, (2007).

72. www.phy.cuhk.edu.hk/~surface/XPSPEAK/

73. Atuchin V.V, Kesler V.G, Kokh A.E, Pokrovsky L.D, “X-ray photoelectron spectroscopy study of β-BaB2O4 optical surface”, Appl Surf Sci, 223, 352-360, (2004).

Appendix –I

Properties of materials

1. **Properties of titanium vapors:**

Specific heat, C_p = 900 J/ Kg-K,

Thermal conductivity, K = 0.1 W/m-K,

Dynamic viscosity, μ = 1.72 x 10-5 kg/m-s

Mass diffusivity (Fickian diffusion), D_m = 2.88 x 10-5 m^2/s,

Molecular weight, M_{Ti} = 48 kg/kmol

2.

Property of Material	Y_2O_3	YO	Y	O_2	O
Density (kg/m^3)	4060	4060	4240	1.2999	0.649961
Specific Heat $(J/kg-K)$	700	700	25.9[18]	Piecewise-polynomial	Piecewise-polynomial
Thermal Conductivity $(W/m-K)$	2.93	2.93	1.56	0.0246	0.03674
Viscosity $(kg/m-S)$	0.002	0.002	0.003	1.919e-05	1.886e-05
Molecular Weight $(kg/kgmol)$	226	105	89[18]	31.9988	16
Std. State Enthalpy $(J/kgmol)$	5429.2	5429.2	421300[18]	0	2.491815e+08
Std. State Entropy $(J/kgmol-K)$	99.1	99.1	179.5[18]	205026.9	160932.6

3. Tantalum (Ta)

Typical Property:

Atomic Number:	73

Mass:

Density at 300 K:	16600 Kg/cu meter

Thermal Properties:

Melting point:	3269 K
Boiling point:	5703 K
Linear coefficient of expansion (per C):	6.5 X 10^{-6} $\mu m \cdot m^{-1} \cdot K^{-1}$
Specific heat (at 25 C):	25.36 $J \cdot mol^{-1} \cdot K^{-1}$
Thermal conductivity (300 K):	57.5 $W \cdot m^{-1} \cdot K^{-1}$

Electrical Properties:

Electrical resistivity (at 20 C):	13.5×10^{-8} Ω-m
Temp. coefficient of resistivity per C:	0.0038

Mechanical Properties:

Ultimate tensile strength:	250 M Pa
Yield strength at high temperatures :	150 M Pa
Young’s modulus of elasticity:	186 G Pa
Poisson’s ratio:	0.34
Thermionic work function,	4.12 eV
A [amp$(cm)^{-2}(K)^{-2}$]:	60
Total emissivity:	At 1800 K = 0.21 and at 2500 K = 0.26.

Temperature dependent electrical resistivity of tantalum:

Sr.no.	Temp (K)	Electrical resistivity x 10^{-8} (Ω-m)
1	273	14.6
2	400	18.6
3	500	22.3
4	600	27.4
5	700	31.8
6	800	34.9
7	900	39.1
8	1000	44.1
9	1100	47.3
10	1200	51.0
11	1300	54.8
12	1400	59.0
13	1500	62.4
14	1600	65.8
15	1700	69.3
16	1800	72.5
17	1900	75.8
18	2000	78.9
19	2100	82.0
20	2200	85.2
21	2300	88.3
22	2400	91.3
23	2500	94.4
24	2600	97.4
25	2700	100.2
26	2800	102.9
27	2900	105.6
28	3000	108.7

Temperature dependent thermal conductivity of tanatalum:

1	273	54.4
2	400	59.9
3	800	66.6
4	1200	72.9
5	1600	77.0
6	2000	80.8
7	2400	83.7
8	2800	88.8

Material used for the manufacturing of **Grid Cup** is **Molybdenum.**

Molybdenom:

Atomic number: 42

Mass:

Density at 300 K: 10280 Kg/cu meter

Thermal Properties:

Melting point: 2896 K

Boiling point: 4912 K

Linear coefficient of expansion (per C): 4.8 X 10^{-6} $\mu m \cdot m^{-1} \cdot K^{-1}$

Specific heat (25 C): 24.06 $J \cdot mol^{-1} \cdot K^{-1}$

Thermal conductivity (300 K): 138 $W \cdot m^{-1} \cdot K^{-1}$

Mechanical Properties:

Ultimate tensile strength: 250 M Pa

Yield strength at high temperatures : 150 M Pa

Young's modulus of elasticity: 329 G Pa

Poisson's ratio: 0.31

Total emissivity: At 1800 K it is 0.11 and at 2500 K it is 0.18

Stainless Steel:

Yield strength:	520 GPa
Young's modulus of elasticity:	193 GPa
Thermal conductivity:	16 W/mK
Density:	8.03 g/cm^3
Linear coefficient of expansion:	17.3 x 10^{-6} m/mK
Poisson's ratio:	0.3
Total emissivity:	0.36

Temperature dependent electrical resistivity of stainless steel 304 :

Sr.no.	Temp (K)	Electrical resistivity x 10^{-8} (Ω-m)
1	273	72
2	932	116

Temperature dependent thermal conductivity of stainless steel 304 :

Sr.no.	Temp (˚K)	Thermal conductivity ($W \cdot m^{-1} \cdot K^{-1}$)
1	300	16.2
2	773	21.4

Aluminum Oxide (Al_2O_3):

Molecular weight: 101.96

Melting point: 2293 K

Crystal density: 3.97 gm/cc

Evaporation temperature: 2373 K

Color: Clear to white

Thermal conductivity: 30 $W \cdot m^{-1} \cdot K^{-1}$

Boiling point: 3250 K

Refractive index: 1.768–1.772